
Analysis of the transverse field Ising model
by
continuous unitary transformations

Master Thesis

Lehrstuhl für Theoretische Physik I
Fakultät Physik
Technische Universität Dortmund

Benedikt Fauseweh
2012

Contents

1	Abstract	5
2	Introduction	6
2.1	Low dimensional spin systems	7
2.2	Quantum critical point	8
2.3	Continuous unitary transformations	9
3	The transverse field Ising model	10
3.1	Qualitative understanding using quasi-particle picture	11
3.2	Exact solution of the transverse field Ising model	13
3.3	Zero temperature characteristics	14
3.4	Quantum critical point	16
3.5	Spectral properties	19
4	Continuous unitary transformations	20
4.1	Concept of continuous unitary transformations	20
4.1.1	Wegner's generator	22
4.1.2	Particle conserving generator	23
4.2	Perturbative CUT and self-similar CUT	25
4.3	Enhanced perturbative CUT	26
4.3.1	Algorithm for the contributions	28
4.3.2	Reduction of the DES	29
4.3.3	Directly evaluated epCUT	30
4.3.4	Transformation of observables	30
4.4	Implementation	32
5	String operator algebra	33
5.1	Definition	33
5.2	Proof of closed algebra property	35
5.3	Closed form of flow equation	41
5.4	Evaluation of effective models within the string algebra	46

6	Static results	49
6.1	Convergence of CUT	49
6.2	Ground state energy	52
6.3	Dispersion	55
6.4	Magnetization	60
6.4.1	Transverse magnetization	60
6.4.2	Longitudinal magnetization	62
6.5	Conclusions of the present chapter	63
7	Dynamic results	64
7.1	Dynamical structure factor	65
7.2	Splitting different quasi-particle spaces	66
7.2.1	One-particle case	68
7.2.2	Two-particle case	69
7.2.3	Three-particle case	70
7.3	Lanczos algorithm and continued fraction representation	72
7.3.1	Errors	73
7.3.2	Termination	74
7.3.3	Band edge singularities	76
7.4	S^{zz} dynamical structure factor	78
7.5	S^{xx} dynamical structure factor	87
7.5.1	One-particle contributions	87
7.5.2	Three-particle contributions	91
7.6	Conclusions of the present chapter	97
8	Conclusion	98
8.1	Results	98
8.2	Outlook	99
	List of figures	100
	List of tables	106
	Bibliography	107

1 Abstract

In this thesis we investigate the transverse field Ising model (TFIM) by continuous unitary transformations (CUT). First we will introduce a spin string algebra as operator basis and show that we are able to reach very high orders with directly evaluated enhanced perturbative CUTs (deepCUT). A general expression for the flow equation up to infinite order will be derived. Next static properties will be investigated including the ground state energy per site, the energy dispersion, and the transverse magnetization. Then we consider dynamical properties, namely the spin dynamical structure factor (DSF). We will use the effective models and observables derived by the CUT method in combination with the Lanczos algorithm and a continued fraction representation of the Green function to calculate one-, two- and three-particle contributions to the DSF. To our knowledge the three particle contributions in the TFIM have not been computed in the literature before.

2 Introduction

Since the discovery of high-temperature superconductivity (HTS) in 1986 [1] in doped cuprates, research on low dimensional spin system has become one of the most important fields of many body physics [2, 3]. In contrast to conventional superconductors, high-temperature superconductors have transition temperatures above 30 K up to 138 K or even higher under pressure [4].

Many applications have been developed for superconductors including superconducting coils in magnetic resonance imaging or very sensitive magnetometers called SQUIDs (superconducting quantum interference device) [5]. This shows that the interest in superconductors is not only motivated by scientific curiosity but also by technological relevance.

While conventional superconductors are well explained by the BCS-theory [6], proposed by John Bardeen, Leon Cooper and John Schrieffer in 1957, high-temperature superconductors can not be described by phononic interactions leading to the formation of cooper pairs. The effect leading to superconductivity in these materials is still being investigated and is one of the major open questions in condensed matter physics [2].

Most of these unconventional superconductors display a magnetically ordered phase without doping [7, 8], which means that the magnetic interactions dominate the electronic and thermodynamic properties. Doping these materials with charge carriers leads to the superconducting phase, which suggests that the magnetic interactions play an important role in the dynamics of additional electrons and holes, respectively. A typical phase diagram for a high- T_c superconductor is depicted in Fig. 2.1.

It has been suggested that the magnetic interactions between the electrons could lead to a similar Cooper pairing effect like in conventional superconductors [9]. Hence a fundamental understanding of antiferromagnetic (and ferromagnetic) effects is important in order to describe the underlying physics.

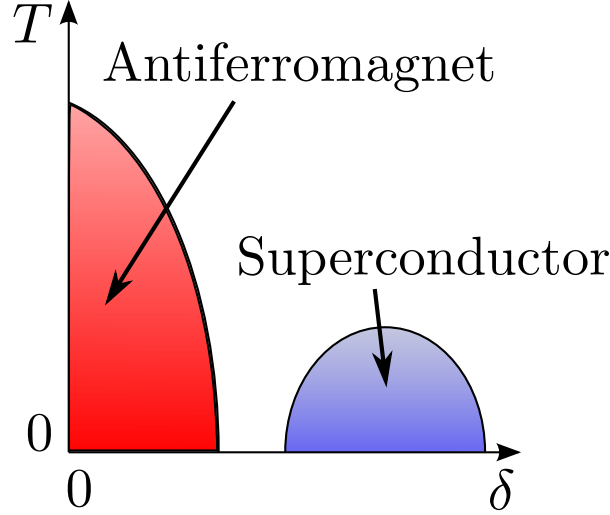


Figure 2.1: Phase diagram for a generic high-temperature superconductor of the cuprate family. T denotes the temperature and δ the degree of doping.

2.1 Low dimensional spin systems

Since cuprate high-temperature superconductors consist of layers of copper oxid separated by layers of other atoms, the physics of the magnetic excitations is mainly two-dimensional. This justifies low dimensional microscopic models which describe the dynamics of these materials. Additional effects such as intra-layer couplings, impurities or anisotropies are often considered of minor importance and are left out in theoretical calculations.

A famous model to describe low dimensional spin systems is the generalized Heisenberg model [10],

$$H = - \sum_{i,j} \sum_{\alpha,\beta} J_{ij}^{\alpha\beta} S_i^\alpha S_j^\beta + \sum_i \vec{B} \cdot \vec{S}_i \quad (2.1.1)$$

where i, j are the lattice sites and $\alpha, \beta \in \{x, y, z\}$ denote the spin vector components. The spin-spin interaction is given by $J_{ij}^{\alpha\beta}$ and can also contain non-diagonal elements, i.e. $\alpha \neq \beta$, while \vec{B} denotes an external magnetic field in suitable units, which couples to all spins on the lattice.

For a low spin, i.e. $S = 1/2$, on a low dimensional lattice, quantum effects play a major role and can result in complex correlations. Hence methods neglecting these features, such as mean-field calculations, can miss a large amount of the physics in the system.

For a general lattice, coupling and external field, the Heisenberg model is usually hard to solve. For certain cases however, analytical results are available and provide a solid test ground with a variety of features to establish new methods and ideas. One of these cases is the transverse field Ising model (TFIM) [11], which can be obtained from the

generalized Heisenberg model by choosing

$$J_{ij}^{\alpha\beta} = J\delta_{i+1,j}\delta_{\alpha\beta}\delta_{\alpha,x}, \quad (2.1.2a)$$

$$\vec{B} = \Gamma\vec{e}_z, \quad (2.1.2b)$$

on a one-dimensional lattice. This leads to the Hamiltonian

$$H_{\text{TFIM}} = \Gamma \sum_i S_i^z - J \sum_i S_i^x S_{i+1}^x. \quad (2.1.3)$$

The TFIM has been studied intensively in many aspects of condensed matter physics [12]. There are also experimental setups and materials which partly realize the physics of the TFIM [13, 14].

2.2 Quantum critical point

The TFIM shows a quantum critical point (QCP). A QCP is a phase transition from an ordered state into a disordered state purely driven by physical parameters at zero temperature $T = 0$. In contrast to conventional phase transitions, where the occurrence of thermal fluctuations lead to a fundamental change in the physics of the system, a quantum phase transition is initiated by quantum fluctuations. This makes them an interesting subject of modern condensed matter research.

In general a QCP can continue into the finite temperature range, connecting to a thermal phase transition. This is, however, not the case for the TFIM, as we will see in the following chapter.

As mentioned before the two phases separated by the QCP usually differ in an order parameter, which is non-zero in the ordered phase, while it is zero in the disordered phase. This is connected to the occurrence of off-diagonal long range order (ODLRO) [15], which implies that correlations are maintained even over a macroscopic number of lattice sites (known as the divergence of the correlation length).

The system lacks an internal length scale at the critical point, because the correlation length diverges. Here the energy gap for the elementary excitations closes and therefore they can be created with infinitesimal energy cost. For this case Sachdev developed a field theoretical approach to describe the dynamics and correlations even at finite temperature [16], similar to the Landau-Ginzburg-Wilson approach to classical phase transitions [17].

The description of dynamical correlation functions in these critical systems is an important task to explain experimental results, such as inelastic neutron scattering rates. In particular the so called dynamical structure factor is specific to the system under investigation and therefore of significant importance in theoretical physics [18].

However, despite the fact that the TFIM is integrable, the calculation of dynamical correlations remains a difficult task. Especially the calculation of longitudinal structure

factors has been impossible for a long time. These are structure factors perpendicular to the transverse field. In 2006, over 40 years after the introduction of the TFIM, Hamer et al. used series expansion techniques to propose an exact expression for the one particle contributions of the longitudinal dynamical structure factor at zero temperature [19]. One aim of this thesis is to verify the results of Hamer et al by using the technique of continuous unitary transformations, which will be described in the following.

2.3 Continuous unitary transformations

Unitary transformations are an important tool to obtain physical information on a system, because they do not change the eigenvalues of the Hamiltonian. Therefore many properties, such as ground state energy or dispersion, can be obtained by applying an appropriate unitary transformation. Examples include the famous Bogoliubov transformation in the BCS-theory or the Fröhlich transformation [20] in electron phonon systems. Often unitary transformations are applied one after another to diagonalize the Hamiltonian or to map the system onto an effective Hamiltonian with a smaller number of degrees of freedom. This is also the basic idea of continuous unitary transformations (CUT). Instead of applying a series of discrete transformations (or a single transformation) the transformation is performed in a continuous way. This transformation maps the Hamiltonian onto an effective Hamiltonian, which still describes all the physics but in an basis that is more suitable for evaluation.

The idea of CUT was first introduced by Wegner [21] and independently by Głazek and Wilson [22, 23]. Since then many different CUT variations have been developed and applied to manifold physical systems. Examples include the dimerized and frustrated $S = 1/2$ chain [24], spin ladder systems [25, 26], the systematic mapping of the Hubbard model to the t - J model [27], the Kitaev honeycomb model [28] and the toric code model in a parallel magnetic field [29]. Recently another CUT approach [30] has been developed based on contributions from finite graphs (gCUT) and was also tested on the TFIM.

In this thesis we will use the CUT method to derive effective models and observables from the TFIM to calculate ground state properties as well as dynamical properties at zero temperature.

3 The transverse field Ising model

The transverse field Ising model (TFIM) was first introduced by de Gennes in 1963 [11] as a pseudo spin model to describe the tunneling of protons in ferroelectric crystals. Since then the model has become a famous example for studying low dimensional strongly interacting systems. It was applied to multiple condensed matter systems. An overview is given in Ref. [12].

The TFIM describes a chain of spins with $S = 1/2$, interacting through a ferromagnetic exchange J along the x axis. A magnetic field is applied perpendicularly to the ferromagnetic interaction along the z axis.

Note that the ferromagnetic exchange can be replaced by an antiferromagnetic exchange $J \rightarrow -J$ without significant influence. This coincides with a π rotation around S_i^z for every second site i . The main difference is the location of the energy gap, which is $q_{\text{crit}} = 0$ for the ferromagnetic case and $q_{\text{crit}} = \pi$ for the antiferromagnetic case. In the following chapter we will consider the ferromagnetic case, while our results are computed for the antiferromagnetic case.

In the following we will consider a chain of infinite size, therefore we do not consider boundary effects nor boundary conditions. This implies the Hamiltonian

$$H_{\text{TFIM}} = \Gamma \sum_i S_i^z - J \sum_i S_i^x S_{i+1}^x, \quad (3.0.1a)$$

$$\Gamma > 0, \quad (3.0.1b)$$

where the sum i runs over all lattice sites. Note that we normalized the distance between two sites to one. In the following we will also use the Pauli matrices which are just multiples of the S operators,

$$\sigma^\alpha = 2S^\alpha \quad \alpha \in \{x, y, z\}. \quad (3.0.2)$$

Note that we have chosen $\hbar = 1$ in all following chapters.

The model was solved exactly by Pfeuty in 1970 [31] based on the works of Lieb et al. [32] and Niemeijer [33]. We will examine this exact solution in section 3.2. First we want to establish a fundamental understanding of the TFIM by introducing a quasi-particle picture and we will study two simple limits of the physical parameters. Later in this chapter we will investigate the zero temperature characteristics. A detailed discussion of the quantum critical point will follow.

Note that the TFIM shows a discrete \mathcal{Z}_2 symmetry

$$S^x \rightarrow -S^x \quad (3.0.3a)$$

$$H \rightarrow H \quad (3.0.3b)$$

on the level of the Hamiltonian. We will see later that this symmetry will spontaneously be broken in the ordered phase.

3.1 Qualitative understanding using quasi-particle picture

To obtain a fundamental understanding of the physics of the TFIM, we will consider two simple limits, namely the strong field limit and the zero field limit. The first one will also be our starting point for a perturbative description by means of CUT.

In the strong field limit, the external field is of much greater magnitude than the internal ferromagnetic interaction

$$\Gamma \gg J. \quad (3.1.4)$$

We can therefore set $J = 0$. Then the Hamiltonian is blockdiagonal in every spin subspace and the local Hilbert spaces for every site i decouple. The system describes free spins with a magnetic field along the z axis, therefore the ground state becomes the fully polarized state

$$|g\rangle = |\cdots \downarrow_{j-1} \downarrow_j \downarrow_{j+1} \cdots\rangle. \quad (3.1.5)$$

This is depicted in Fig. 3.1.

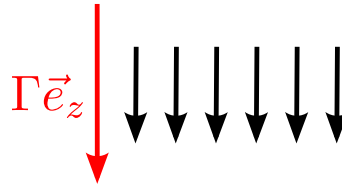


Figure 3.1: In the limit $J = 0$ the fully polarized state becomes the ground state of the TFIM.

Note that in this limit the \mathcal{Z}_2 symmetry is also provided by the ground state, because

$$M_x = \langle g | \sigma^x | g \rangle = 0 \xrightarrow{\mathcal{Z}_2} -M_x = 0 = M_x \quad (3.1.6)$$

holds.

In this limit an elementary excitation is given by a single spin flip in the system, as depicted in Fig. 3.2.

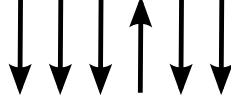


Figure 3.2: Elementary excitation of the TFIM in the strong field limit.

Under the influence of a finite but small J the excitations hop from site to site and show an energy dispersion, which depends on the total momentum q .

Note that on a single site only one excitation can exist, which is similar to the Pauli principle in fermionic systems. On the other hand the wave function of a multi-particle state is symmetric under particle exchange, which is a bosonic property. Therefore the elementary excitations are called hard-core bosons.

The complementary limit is the zero field or strong interaction limit, which means that the internal ferromagnetic exchange is of much larger magnitude than the external field,

$$\Gamma \ll J. \quad (3.1.7)$$

We can therefore set $\Gamma = 0$, i.e. the external field is deactivated. In this limit the model is reduced to the classical one-dimensional Ising model [34]. At zero temperature the ground state is twofold degenerate. A graphical representation of the two ground states is depicted in Fig. 3.3.



Figure 3.3: The two ground states of the TFIM in the strong interaction limit.

Note that these states break the \mathbb{Z}_2 symmetry due to

$$M_x = \langle g | \sigma^x | g \rangle \xrightarrow{\mathbb{Z}_2} -M_x \neq 0. \quad (3.1.8)$$

In contrast to the strong field limit, the elementary excitations are domain walls between the two ground states. These excitations are extremely non-local in the spin picture, i.e. a single domain wall is represented by an infinite number of spin flips. A graphical illustration is shown in Fig. 3.4.



Figure 3.4: Domain walls are the elementary excitations of the TFIM in the strong interaction limit.

We will refer to the phase, where $M_x \neq 0$, as the ferromagnetically ordered phase.

3.2 Exact solution of the transverse field Ising model

In this section we will discuss the exact solution of the TFIM calculated by Pfeuty in 1970 [31]. Starting point is the Hamiltonian in Eq. (3.0.1a). Expressing the spin operators by S^+ and S^- yields

$$H = \Gamma \sum_j \left(S_j^+ S_j^- - \frac{1}{2} \right) - \frac{J}{4} \sum_j (S_j^+ S_{j+1}^- + \text{h. c.}) + (S_j^+ S_{j+1}^+ + \text{h. c.}). \quad (3.2.9)$$

Next a Jordan Wigner transformation [35]

$$S_j = \exp \left(-\pi i \sum_{k < j} c_k^\dagger c_k \right) c_j S_j^+ = \exp \left(\pi i \sum_{k < j} c_k^\dagger c_k \right) c_j^\dagger \quad (3.2.10a)$$

is applied, which maps the Hamiltonian onto a system of free fermions,

$$H = \Gamma \sum_j \left(c_j^\dagger c_j - \frac{1}{2} \right) - \frac{J}{4} \sum_j (c_j^\dagger c_{j+1} + \text{h. c.}) + (c_j^\dagger c_{j+1}^\dagger + \text{h. c.}). \quad (3.2.11)$$

Note that the Jordan Wigner transformation is highly non-local. Therefore the evaluation of correlation functions is rather complicated, especially in the longitudinal case. Next a Fourier transformation followed by a Bogoliubov transformation [36] is applied to diagonalize the remaining Hamiltonian, resulting in the expression

$$H = \Gamma \sum_q \Lambda_q \eta_q^\dagger \eta_q - \frac{\Gamma}{2} \sum_q \Lambda_q, \quad (3.2.12)$$

with the energy dispersion Λ_q given by

$$\Lambda_q = \sqrt{1 + \frac{J^2}{4\Gamma^2} - \frac{J}{\Gamma} \cos(q)}. \quad (3.2.13)$$

Note that q denotes the wave vector in the Brillouin zone. With the help of the dispersion we can also obtain the energy gap Δ as a function of J ,

$$\Delta = \Gamma \left| 1 - \frac{J}{2\Gamma} \right|. \quad (3.2.14)$$

The gap is located at $q_{\text{crit}} = 0$ in the Brillouin zone for a ferromagnetic exchange J . The ground state energy per site is given by the expression

$$\frac{E_0}{N} = -\frac{\Gamma}{2} \sum_q \Lambda_q \stackrel{N \rightarrow \infty}{=} -\frac{\Gamma}{2} \frac{1}{\pi} \int_0^\pi \Lambda_q dq. \quad (3.2.15)$$

This function is non-analytic for $J = 2\Gamma$.

3.3 Zero temperature characteristics

The ground state energy per site in Eq. (3.2.15) is shown in Fig. 3.5.

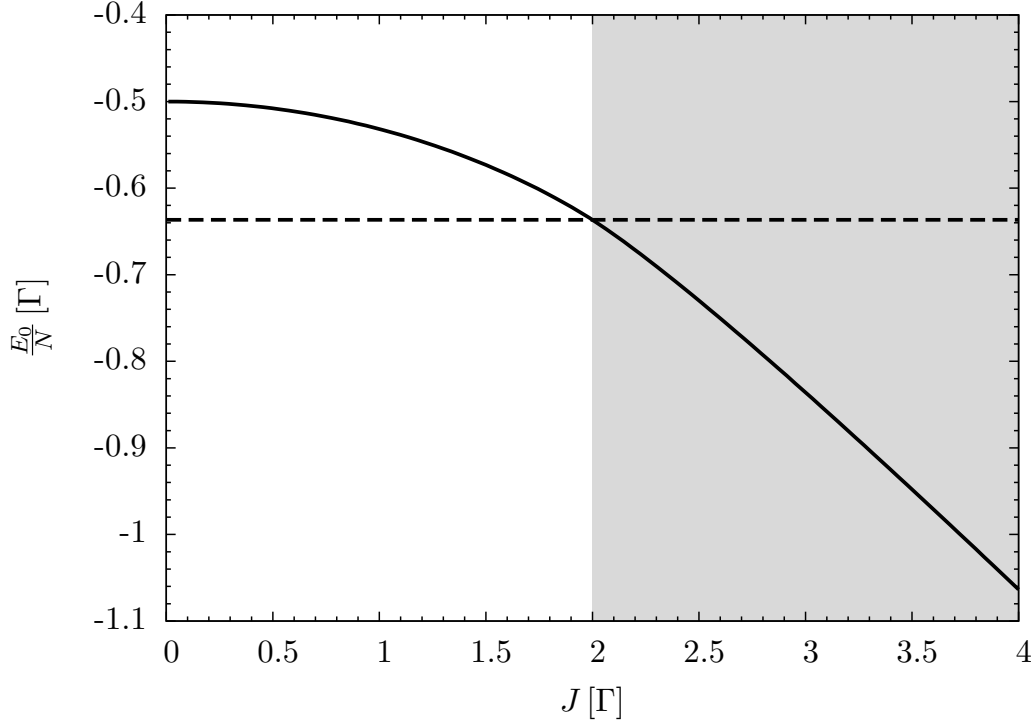


Figure 3.5: Ground state energy per site of the TFIM as function of J . The gray shaded region shows the ferromagnetically ordered phase while the black dashed line indicates the value of the groundstate energy at the phase transition, see section 3.4.

The energy dispersion of the elementary excitations for various values of J is depicted in Fig. 3.6. The dispersion is flat in the case $J = 0$ and begins to disperse with rising parameter.

Note that the energy gap closes for the parameter $J = 2\Gamma$. For higher parameters the gap opens again and is only zero at a single point as a function of J . Note that the ground state energy is also non-analytic for $J = 2\Gamma$. This is hard to grasp by looking only at Fig. 3.5.

Another interesting property is the magnetization along the transverse field,

$$M_z = \langle g | \sigma_z | g \rangle. \quad (3.3.16)$$

This property has also been worked out by Pfeuty

$$M_z = \frac{1}{\pi} \int_0^\pi \frac{1 + \frac{J}{2\Gamma} \cos(q)}{\Lambda_q} dq, \quad (3.3.17)$$

and is shown in Fig. 3.7.

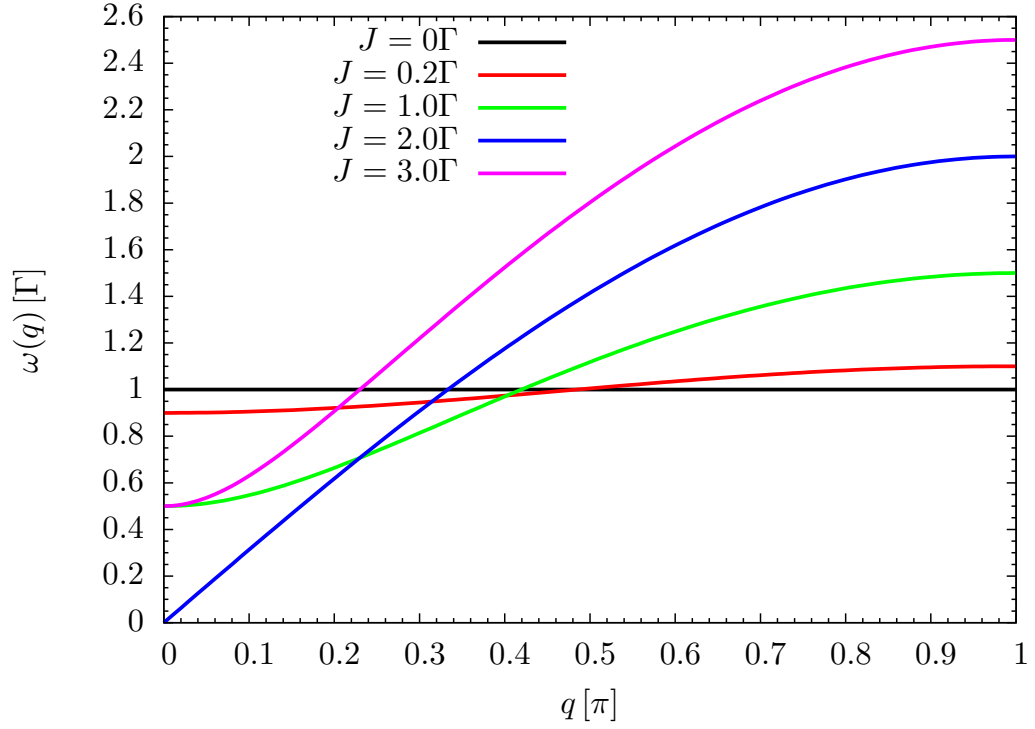


Figure 3.6: Energy dispersion of the elementary excitations of the TFIM for various values of J as function of wave vector q . Note that the dispersion is symmetric in the region $q < 0$, which is not shown here.

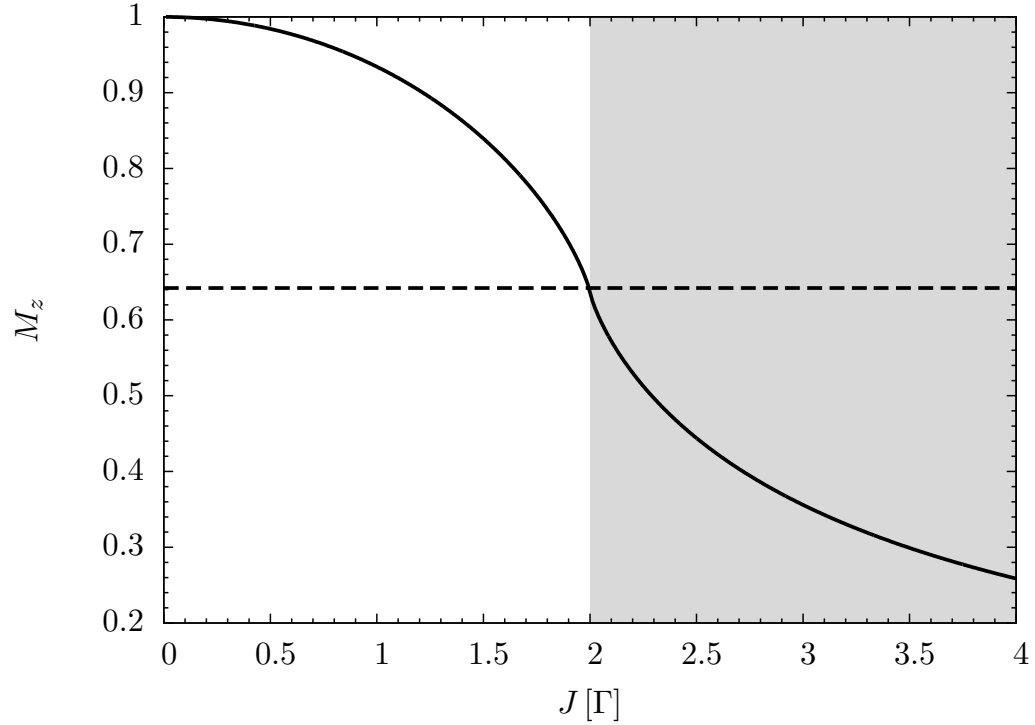


Figure 3.7: Transverse magnetization M_z as a function of J in the TFIM. The gray shaded region shows the ferromagnetically ordered phase while the black dashed line indicates the value of the transverse magnetization at the phase transition, see section 3.4.

For $J = 0$, all spins are aligned along the external field and the transverse magnetization is at its maximum. With rising parameter J , the interaction disturbs the effect of the external field and the magnetization begins to decrease. Note that the point $J = 2\Gamma$ is clearly non-analytical, which can be extracted from the exact formula in Eq. (3.3.17) and also from the graph of the function.

3.4 Quantum critical point

As mentioned earlier, the energy gap of the system closes for $J = 2\Gamma$. This is one of the key indications for a fundamental change in the underlying physics of the system. The two limiting cases we have seen before differ strongly in their ground state symmetries and a phase transition must occur between these two phases.

Another important feature is the existence of an order parameter M_x , that describes the degree of long range order in the system. This parameter differs from zero in the ordered phase, as opposed to the disordered phase.

The appearance of long range order is associated with a broken symmetry, as we have seen in the zero field limit.

One way to deal with long range order is the calculation of correlation functions, such as

$$G^x(n) = \langle g | \sigma_j^x \sigma_{j+n}^x | g \rangle. \quad (3.4.18)$$

In general we expect that the correlation decreases with rising distance n . Therefore

$$\lim_{n \rightarrow \infty} \langle g | \sigma_j^x \sigma_{j+n}^x | g \rangle = C \langle g | \sigma_j^x | g \rangle \langle g | \sigma_{j+n}^x | g \rangle \quad (3.4.19)$$

should hold. In the ordered phase $\langle g | \sigma_j^x | g \rangle$ differs from zero (if there is an infinitesimal field along x), so that the correlation functions never drops to zero, which explains the concept of long range order. Due to this fact the observable $M_x = \langle g | \sigma_j^x | g \rangle$ is the order parameter of the TFIM.

Fortunately, Pfeuty calculated the longitudinal magnetization M_x as a function of the ferromagnetic interaction strength J ,

$$M_x = \begin{cases} \left(1 - \frac{4\Gamma^2}{J^2}\right)^{\frac{1}{8}} & , \quad J \geq 2\Gamma \\ 0 & , \quad J < 2\Gamma \end{cases} \quad (3.4.20)$$

which is depicted in Fig. 3.8. As we can see the order parameter is zero for $J < 2\Gamma$ and rises rapidly for $J \geq 2\Gamma$, which indicates the phase transition for the TFIM. This point is generally denoted as a quantum critical point (QCP), which marks a phase transition at zero temperature purely driven by the physical parameter J .

Another important quantity in this context is the correlation length ξ . The correlation

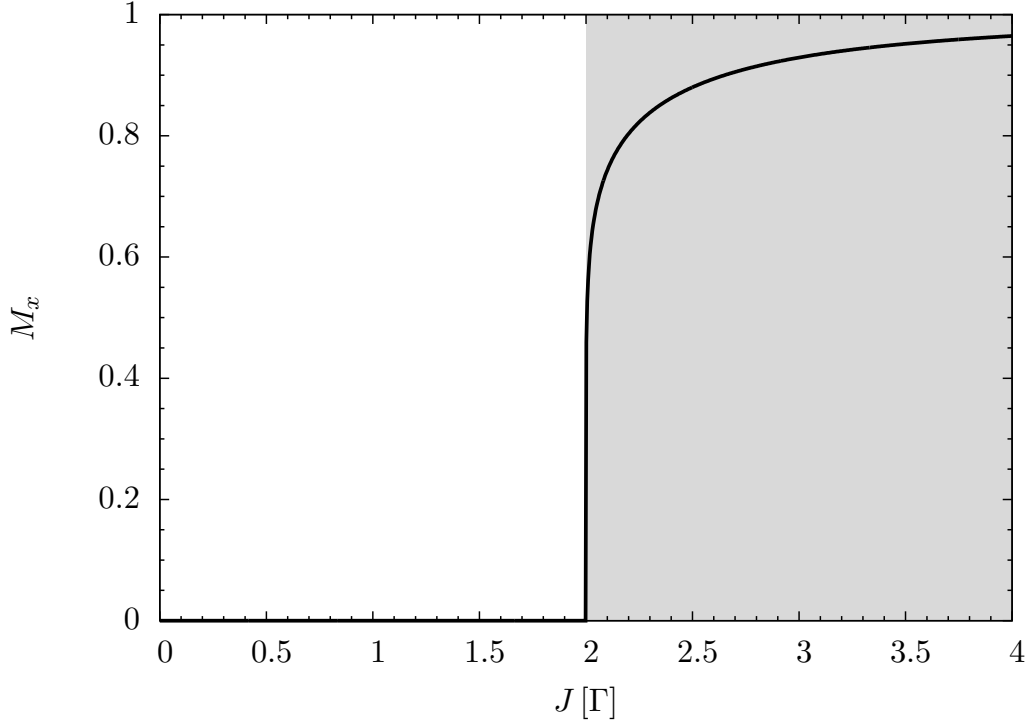


Figure 3.8: Longitudinal magnetization M_x as a function of J . The gray shaded region shows the ferromagnetically ordered phase.

length is defined as the length in which correlation functions typically begin to vanish,

$$G^x(n) \propto \exp\left(-\frac{n}{\xi}\right). \quad (3.4.21)$$

The concept of long range order is connected to the divergence of ξ . For $J < 2\Gamma$ the correlation length remains finite, but when approaching the critical point $J \rightarrow 2\Gamma$

$$\xi \rightarrow \infty, \quad (3.4.22)$$

holds.

Similar to the finite temperature case, we can also define critical exponents which describe the behaviour of observables $O(J)$ close to the quantum critical point,

$$O(J) \propto (J - 2\Gamma)^\theta, \quad (3.4.23)$$

where θ denotes the critical exponent. For the order parameter the corresponding critical exponent is denoted β by convention and can be derived from Eq. (3.4.20). It takes the value

$$\beta = \frac{1}{8}. \quad (3.4.24)$$

Note that the quantum critical point does not continue to $T \neq 0$ but induces a quantum

critical region where the physics of the model is influenced by thermal as well as by quantum fluctuations. We stress that for $T \neq 0$ no ferromagnetic ordered phase exists because the elementary domain walls are non-local excitations that create a macroscopic change of the magnetization. This is similar to the classical one-dimensional Ising model, where there is no phase transition at $T > 0$ either, see Ref. [34].

With this information we can construct a phase diagram of the TFIM, see Fig. 3.9.

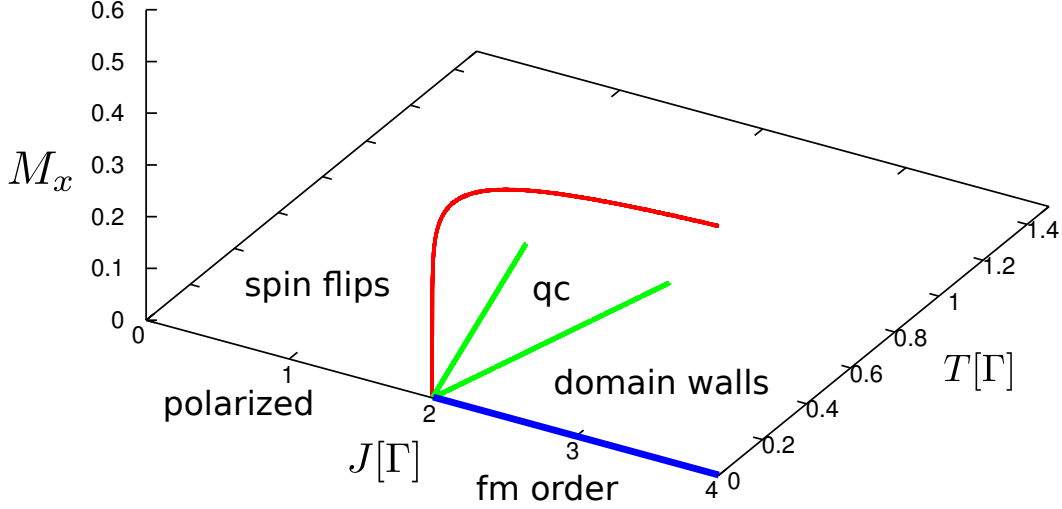


Figure 3.9: Phase diagram of the TFIM. The red curve indicates the order parameter and is only non-zero for $T = 0$, i.e. in the M_x - J -plane. The green curves indicate the quantum critical region (qc), here the physics is mainly dominated by quantum and thermal fluctuations. The blue line shows the ferromagnetic ordered phase (fm order) which does not extend to finite temperatures $T > 0$. The elementary excitations of the ferromagnetic ordered phase are domain walls. For small parameters $J < 2\Gamma$ the system is in the polarized state (polarized) with single spin flips as elementary excitations.

3.5 Spectral properties

Although the TFIM is analytically integrable, the evaluation of dynamical correlations remains a difficult task. The main reason for this is the non-local Jordan Wigner Transformation in Eq. (3.2.10a), which makes evaluation of Green functions of the kind

$$G^x(n, t) = \langle g | \sigma_j^x \sigma_{j+n}^x(t) | g \rangle, \quad (3.5.25)$$

challenging. This is due to the fact that for $n \rightarrow \infty$ the Green function includes infinitely many factors that need to be computed.

One important quantity in the study of spin systems is the dynamical structure factor (DSF),

$$S^{\alpha\beta}(\omega, Q) = \frac{1}{N} \int_{-\infty}^{\infty} \frac{dt}{2\pi} \sum_{l, l'} e^{i\omega t} e^{-iQ(l-l')} \langle S_l^\alpha(t) S_{l'}^\beta \rangle, \quad (3.5.26a)$$

$$\alpha, \beta \in \{x, y, z\},$$

which is the Fourier transformation of the real-space- and time-dependent correlation function. For $\alpha = \beta = z$ exact results are known [37, 38], but for $\alpha = \beta = x$ only the one particle contributions have been calculated by Hamer et al. in 2006 [19].

The DSF is an important quantity because it is directly linked to the differential cross section in inelastic scattering experiments, see Ref. [39].

A more detailed discussion will be given in chapter 7.

4 Continuous unitary transformations

In this thesis we will use the method of continuous unitary transformations (CUT) to derive effective models, which allow for an easier evaluation of ground state properties and dynamical correlation functions. The concept is also known under the name flow equation method. The idea of CUT was first introduced by Wegner [21] and independently by Głazek and Wilson [22, 23].

In this chapter we will introduce the general concepts of CUT and focus on the enhanced perturbative realization of the method (epCUT) [40, 41]. Concepts such as the residual off-diagonality (ROD) and the directly evaluated epCUT (deepCUT) will be presented. Finally we will give an overview on the numerical implementation of the CUT used in this thesis.

4.1 Concept of continuous unitary transformations

The goal of many studies in strongly correlated systems is the diagonalization of the Hamiltonian. One major problem that appears even for low dimensional quantum systems is the exponential growth of the Hilbert space when including additional degrees of freedom, such as additional sites on a finite chain of spins. In one-dimensional systems full exact diagonalization (FED) is limited to much less than 100 sites, even if the local Hilbert space is only two-dimensional. This size is far away from real solid state physics where 10^{23} particles interact with one another.

In general a Hamiltonian can be diagonalized by the use of an appropriate unitary transformation

$$H_{\text{diag}} = U H U^\dagger, \quad (4.1.1)$$

where U is a unitary matrix and H is the systems Hamiltonian. Many studies apply unitary transformations to map the Hamiltonian into a more convenient form. This corresponds to a change of basis in the Hilbert space of the Hamiltonian. In praxis it is rather difficult to find a unitary transformation that directly yields a diagonal Hamiltonian. Furthermore there is no systematic method to obtain such a transformation for different models, i.e., for every Hamiltonian we have to rethink on how to obtain a

diagonalizing unitary transformation.

The idea of CUT is to use a more systematic way to find a unitary transformation that maps the Hamiltonian into a diagonal representation. We therefore introduce a family of unitary transformations depending differentiable on a parameter $l \in \mathbb{R}^+$, which makes the Hamiltonian dependent on l via,

$$H(l) = U(l)HU^\dagger(l). \quad (4.1.2)$$

To create an Hamiltonian that is differentiablely dependent on l we specify the initial condition by

$$H(l)|_{l=0} = H \Rightarrow U(l)|_{l=0} = \mathbb{1}. \quad (4.1.3)$$

Therefore the unitary transformation is performed in a continuous fashion. By taking the derivative of Eq. (4.1.2) we obtain the expression

$$\partial_l H(l) = (\partial_l U(l))HU^\dagger(l) + U(l)H(\partial_l U^\dagger(l)), \quad (4.1.4a)$$

$$= (\partial_l U(l)) \underbrace{U^\dagger(l)U(l)}_{=\mathbb{1}} HU^\dagger(l) + U(l)H \underbrace{U^\dagger(l)U(l)}_{=\mathbb{1}} (\partial_l U^\dagger(l)), \quad (4.1.4b)$$

$$= (\partial_l U(l))U^\dagger(l)H(l) + H(l)U(l)(\partial_l U^\dagger(l)), \quad (4.1.4c)$$

in which we introduce the generator of the CUT by

$$\eta(l) = (\partial_l U(l))U^\dagger(l), \quad (4.1.5a)$$

$$\Rightarrow \partial_l U(l) = \eta(l)U(l). \quad (4.1.5b)$$

A formal solution for the unitary transformation is given by

$$U(l) = Le^{\int_0^l \eta(l') dl'}, \quad (4.1.6)$$

where L is the l -ordering operator, similar to the standard time-ordering operator. This also explains why $\eta(l)$ is denoted as the generator of the CUT.

It is easy to show that the generator is antihermitian,

$$0 = \partial_l \mathbb{1} = \partial_l (U(l)U^\dagger(l)) \quad (4.1.7a)$$

$$= (\partial_l U(l))U^\dagger(l) + U(l)(\partial_l U^\dagger(l)) = \eta(l) + \eta^\dagger(l). \quad (4.1.7b)$$

Using Eq. (4.1.4c) we can compute the derivative of the flowing Hamiltonian $H(l)$ with respect to l . A short calculation yields

$$\partial_l H(l) = [\eta(l), H(l)] \quad (4.1.8)$$

which is the flow equation for the Hamiltonian $H(l)$. It is a first order differential equation with the initial condition given in Eq. (4.1.3).

For $l \rightarrow \infty$ the Hamiltonian acquires its final form and it is denoted as the effective Hamiltonian

$$H_{\text{eff}} = H(l)|_{l=\infty} = U(\infty) H U^\dagger(\infty). \quad (4.1.9)$$

In this context the question of convergence of the expression above can not be answered and depends on the specific form of the generator as well as on truncation criteria.

Note that observables O also need to be transformed into effective observables with the same unitary transformation. This results in the flow equation for observables via

$$\partial_l O(l) = [\eta(l), O(l)]. \quad (4.1.10)$$

Finally, the effective observable is given by

$$O_{\text{eff}} = O(l)|_{l=\infty} = U(\infty) O U^\dagger(\infty), \quad (4.1.11)$$

where the effective observable is expressed in the same basis as the effective Hamiltonian. Note that the generator characterizes the CUT and the flow of the Hamiltonian. The choice of the generator is an important question and it still represents an active field of research.

4.1.1 Wegner's generator

The first choice was Wegner's generator [21]. He decomposed the Hamiltonian into two parts, one that is already diagonal H_d and the non-diagonal part H_{nd} ,

$$H = H_d + H_{\text{nd}}. \quad (4.1.12)$$

Wegner's generator is then given by the commutator between the diagonal part and the non-diagonal part,

$$\eta_{\text{Weg}}(l) = [H_d(l), H_{\text{nd}}(l)] = [H_d(l), H(l)]. \quad (4.1.13)$$

Notice that the second equality holds simply because the diagonal part commutes with itself. The matrix elements of Wegner's generator are given by

$$\eta_{\text{Weg},ij}(l) = (h_{ii}(l) - h_{jj}(l)) h_{ij}(l). \quad (4.1.14)$$

To show that Wegner's generator creates a diagonal Hamiltonian we calculate the derivative of the sum of the squared non-diagonal elements,

$$\partial_l \sum_{i \neq j} |h_{ij}(l)|^2 = -2 \sum_{i,j} (h_{ii}(l) - h_{jj}(l))^2 |h_{ij}(l)|^2. \quad (4.1.15)$$

As we can see, the derivative is always negative or zero and the sum of the squared non-diagonal elements is bounded from below, which proves the convergence of the generator.

There are two disadvantages associated with Wegner's generator. First, the right hand side of Eq. (4.1.14) vanishes for degeneracies. Thus it is not possible to decouple degenerate subspaces with Wegner's generator. Second, Wegner's generator does not conserve band diagonal structures. In second quantization this implies that if the initial Hamiltonian creates n quasi-particles at maximum, $H(l)$ can create more than n during the flow. The flow of Wegner's generator is depicted in Fig. 4.1.

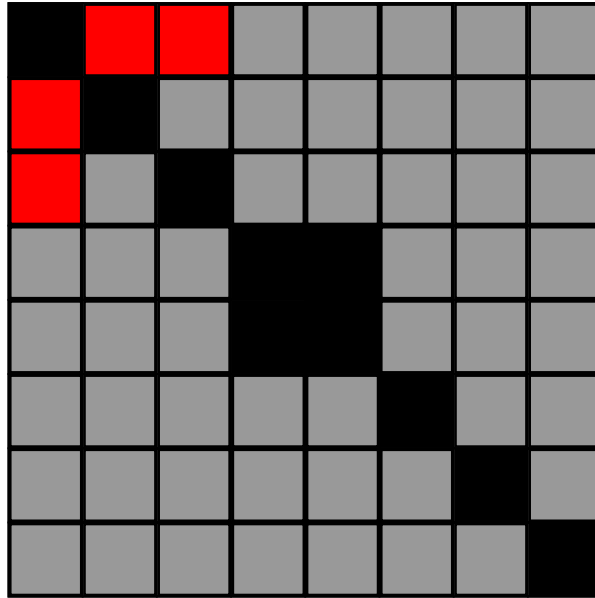


Figure 4.1: Illustration of Wegner's generator. The boxes represent the matrix elements. The red boxes indicate the initial non diagonal parts of the Hamiltonian. The grey boxes indicate the Hamiltonian during the flow. The black boxes indicate the effective Hamiltonian after the flow. Note that degenerate subspaces are not diagonalized, represented by bigger black boxes.

4.1.2 Particle conserving generator

To overcome the disadvantages of Wegner's generator and to apply the idea of CUT to a more general context, Mielke [42], in the context of band-matrices, and independently Knetter and Uhrig [43], in the context of many-body physics, developed the particle conserving (pc) or MKU generator. The pc generator directly aims at the quasi-particle picture. The goal is to eliminate terms that are not quasi-particle conserving, leading

to the requirement

$$[H_{\text{eff}}, Q] = 0 \quad (4.1.16)$$

in which Q counts the number of quasi-particles in the system.

The pc generator in matrix representation, in the eigenbasis of Q , is given by

$$\eta_{\text{pc},ij}(l) = \text{sgn}(q_i - q_j) h_{ij}(l), \quad (4.1.17)$$

where q_i denotes the eigenvalues of the Operator Q . An equivalent description of the pc generator can be given by decomposing the Hamiltonian into parts that create, $H^+(l)$, conserve, $H^0(l)$, and annihilate, $H^-(l)$, quasi-particles,

$$H(l) = H^+(l) + H^0(l) + H^-(l). \quad (4.1.18)$$

Then, the quasi-particle conserving generator is simply given by

$$\eta_{\text{pc}} = H^+(l) - H^-(l). \quad (4.1.19)$$

The convergence of the generator is proven for finite-dimensional systems, where a state of minimal energy exists. Note that the pc generator preserves the band diagonal structure, i.e., the maximum number of particles created during the flow remains constant. This is shown in Fig. 4.2.

Problems, however, can occur if the energies of multi particle states fall below the energy of single or no particle energies. This is due to the fact that the pc generator attempts to sort all quasi-particle spaces according to energy, even if higher quasi-particle spaces have less energy than lower quasi-particle spaces. For systems with a finite energy gap this can be a minor problem, but for systems with a quantum phase transition, such as the TFIM, the quasi-particle picture can break down and the validity of the CUT must be questioned.

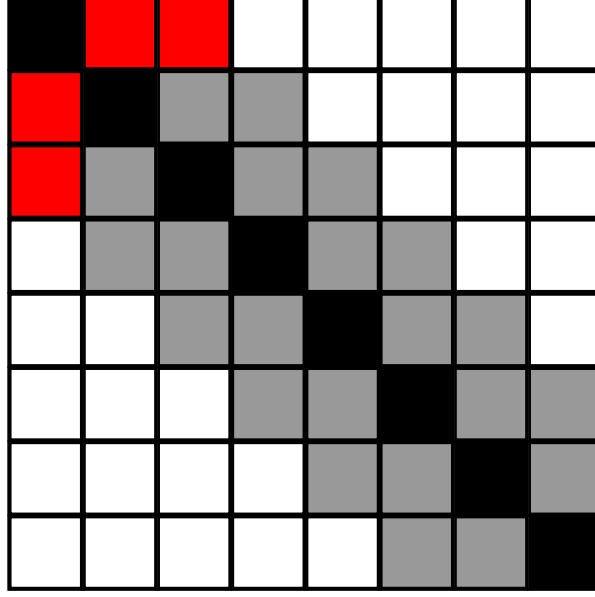


Figure 4.2: Illustration of the pc generator. The boxes represent the matrix elements. The red boxes indicate the initial non diagonal parts of the Hamiltonian. The grey boxes indicate the Hamiltonian during the flow. The black boxes indicate the effective Hamiltonian after the flow. Note that the band diagonal structure is preserved during the flow.

4.2 Perturbative CUT and self-similar CUT

The CUT method consists of two fundamental steps. The commutator in Eq. (4.1.8) needs to be calculated, followed by the integration of the resulting flow equation. The latter can easily be done with standard numerical integration algorithms or even analytically.

In general, commuting H with η will create new types of terms that were originally not part of the Hamiltonian. For systems with a finite dimension the operator space acting on that Hilbert space is also finite, therefore only a finite number of new terms might appear. Then, if the size of the Hilbert space is not too large for numerical calculations, the CUT can be achieved in full accuracy.

This differs from situations in which the Hilbert space of the system has infinite dimensions. Examples include systems in the thermodynamic limit. Here, all sorts of new terms might arise, connecting several sites over large distances. In a numerical calculation we cannot treat an infinite number of operators, hence we have to restrict ourselves to operators which are physically relevant.

One particularly successful approach towards this goal was perturbative CUT (pCUT) [43]. In this method the Hamiltonian is divided, according to standard perturbation theory, into a simple part H_0 and a perturbation xV . For pCUT, H_0 needs to have an equidistant spectrum, while there are no restrictions concerning the perturbation. The perturbation V is divided according to the number m of quasi-particles it creates or

annihilates,

$$V = \sum_{m=-N}^{m=N} T_m, \quad (4.2.20)$$

where T_m creates m quasi-particles and N is the maximum number of quasi-particles that is created by V . Note that pCUT is solely defined for the pc generator. Furthermore the restriction to an equidistant H_0 is a drawback. On the other hand, pCUT is described in a very general context, therefore the flow equation can be solved independently for a variety of models. Only the action of the effective operators for the considered model must be calculated to obtain an effective quasi-particle conserving model.

Another approach is self-similar CUT (sCUT) [44]. Here the structure of operators in second quantization is arbitrary and no equidistant spectrum is required. Furthermore, we are not restricted to the pc generator. The crucial point of sCUT is to choose a certain operator basis and calculate the commutator for the flow equation in this operator basis in a self-similar fashion. This also implies that certain terms, which are not part of the operator basis, will be truncated in order to obtain a finite size flow equation. The truncation scheme depends on the model under consideration and typically involves the range of operators as well as the number of quasi-particles the operator acts on [45]. For example, in a system of low quasi-particle density, terms describing the correlated hopping of multiple excitations over a long range will be dropped in favour of terms describing the hopping of a single excitation over a short range.

The advantages of sCUT are the free choice of the generator as well as the operator basis. On the other hand the flow equation must be solved anew for each model and the truncation scheme can include rather sophisticated considerations.

To avoid this variability in the truncation scheme the sCUT approach can be expanded perturbatively, yielding the method of enhanced pCUT (epCUT). On the one hand it contains the free choice of the generator and H_0 but also the perturbatively controlled expansion of the flow equation. In the following we will explain the epCUT method according to Ref. [41].

4.3 Enhanced perturbative CUT

The idea of epCUT is to calculate all contributions to the *differential equation system* (DES) correctly up to a given order. We stress that the algorithm is independent of the chosen operator basis, but can result in different flow equations depending on the form of the operators. We will denote our operators by the basis-set $\{A_i\}$. Then the flow Hamiltonian can be written as

$$H(l) = \sum_i h_i(l) A_i \quad (4.3.21)$$

where the coefficients depend on the flow parameter l . For the generator we choose the same operator basis with different coefficients,

$$\eta(l) = \sum_i \eta_i(l) A_i = \sum_i h_i(l) \eta[A_i] \quad (4.3.22)$$

where $\eta[\cdot]$ is a superoperator applying the generator scheme to the operator. For example, if considering the pc generator, the fermionic creator c^\dagger would simply yield $\eta[c^\dagger] = c^\dagger$ while its hermitian conjugate c would yield $\eta[c] = -c$, see also Eq. (4.1.19).

With this definitions we can obtain the flow equation for a given generator basis by

$$\sum_i \partial_l h_i(l) A_i = \sum_{j,k} h_j(l) h_k(l) [\eta[A_j], A_k]. \quad (4.3.23)$$

Note that the commutator on the right hand side is in general a linear combination of the operator basis $\{A_i\}$. We can therefore compare the coefficients for all operators to obtain a scalar flow equation

$$\partial_l h_i(l) = \sum_{j,k} D_{ijk} h_j(l) h_k(l). \quad (4.3.24)$$

We call the $D_{ijk} \in \mathbb{C}$ the *contributions* to the DES. They are obtained by calculating the commutator in Eq. (4.3.23) and expanding the results in the given operator basis. The contributions are the prefactors in this operator basis,

$$\sum_i D_{ijk} A_i = [\eta[A_j], A_k]. \quad (4.3.25)$$

Note that this notation is still general and also applies to sCUT. The operator basis $\{A_i\}$ is not necessarily a multi-particle-representation. This fact will be used in the following chapters.

Now we want to expand the flow equation in a small parameter x . We thus write our initial Hamiltonian in the form,

$$H = H_0 + xV \quad (4.3.26)$$

where H_0 describes the unperturbed Hamiltonian and V represents a perturbation. Note that there are no restrictions concerning H_0 , but we will see later that the method works best for a local and block-diagonal H_0 .

Next, we expand the Hamiltonian during the flow according to the order of the parameter x ,

$$H(l) = \sum_{m=0}^{m=n} H^{(m)}, \quad H^{(m)} \propto x^m, \quad (4.3.27)$$

where n denotes the maximum order that our calculation aims at. By using the representation in Eq. (4.3.21) we also divide the coefficients $h(l)$ according to orders in x ,

$$h_i(l) = \sum_{m=0}^{m=n} x^m f_i^{(m)}(l). \quad (4.3.28)$$

Note that the initial values of $f_i^{(m)}(0)$ are fixed by the starting conditions $h_i(0)$. Next we insert this representation into Eq. (4.3.24), which yields

$$\partial_l \sum_{m=0}^{m=n} x^m f_i^{(m)}(l) = \sum_{j,k} D_{ijk} \sum_{p,q}^n x^{p+q} f_j^{(p)}(l) f_k^{(q)}(l). \quad (4.3.29)$$

Comparing coefficients yields the perturbative expansion of the flow equation,

$$\partial_l f_i^{(m)}(l) = \sum_{j,k} D_{ijk} \sum_{p,q}^{p+q=m} f_j^{(p)}(l) f_k^{(q)}(l). \quad (4.3.30)$$

Note that the contributions D_{ijk} do not depend on the order of calculation but only on the algebraic relations between the operators $\{A_i\}$. Furthermore Eq. (4.3.30) defines a hierarchy for the coefficients of the flow equation, which means that a certain order is only influenced by the same or by lower orders and not by higher ones.

4.3.1 Algorithm for the contributions

Once all contributions D_{ijk} and operators relevant for a certain order are known, the remaining task is to integrate the flow equation (4.3.30). Note that certain prefactors are influenced only in high order calculations, e.g., long range hopping terms in a nearest neighbor Hamiltonian will only be created in high orders. This means that the corresponding coefficient $f_i^{(m)}$ is nonzero only for high enough m . Hence one of the remaining tasks is to calculate all contributions that are relevant up to a given target order n .

An effective algorithm is sketched in Fig. 4.3. Because of the hierarchy for the coefficients, the calculation to obtain all contributions for a given order is based on the previous orders. First note that horizontal and vertical lines in boxes indicate self-consistent runs, i.e., the commutation of $[\eta^{(1)}, H^{(0)}]$ might produce new first order terms that need to be included into the generator $\eta^{(1)}$. Then the commutator must be recalculated to include the new operators in the generator. This procedure must be repeated until self-consistency is reached. If the local Hilbert space is finite and H_0 is local, the self-consistent runs are guaranteed to finish, because the number of operators on a finite cluster is finite. If H_0 contains non block-diagonal terms the commutators $[\eta^{(0)}, H^{(m)}]$ also have to be carried out self-consistently.

If one of these self-consistent runs does not terminate, i.e., H_0 is not block-diagonal and not local, additional truncation criteria have to be introduced, which means that parts

of the epCUT will be sCUT calculations.

When calculating the commutator $[\eta[A_j], A_k]$ new operators might appear that are not yet part of the operator basis. In this case they will be included in the operator basis and we define the minimal order of these operators $O_{\min}(A_i)$ as the order in which they occur first.

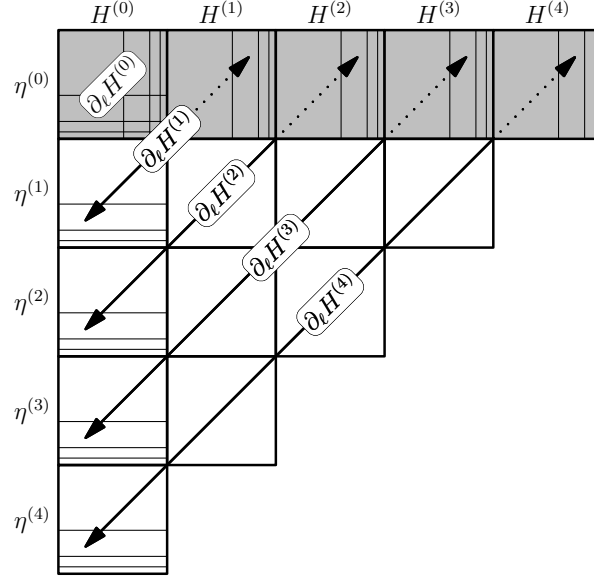


Figure 4.3: Illustration of the algorithm used to determine all contributions for a given maximum order, here 4, from Ref. [41]. The boxes represent the calculation of the commutator between the different orders of the generator $\eta^{(m)}$ and the Hamiltonian $H^{(n)}$ to obtain the contributions to the DES. The calculation for every order o is based on the previous orders and is achieved by calculating every commutator with $n + m = o$.

4.3.2 Reduction of the DES

To save memory and computation time several optimizations have been introduced in Ref. [41]. One possibility is the reduction of the size of the resulting DES by aiming only at certain quantities of interest. For example, single hopping terms will not be influenced by multi-particle interactions that only appear in very high orders. This means that if we are only interested in single particle properties, such as the dispersion we can neglect all contributions that do not influence our quantity of interest. The justification of this approach lies in the hierarchy of the DES. We therefore introduce the maximum order of an operator A_i $O_{\max}(A_i)$. It is defined as the maximum order in which an operator still influences the quantity of interest.

For a more detailed discussion we refer the reader to Ref. [41], from which we take over the expression

$$O_{\max}(A_j) = \max_{\{i,k|D_{ijk} \neq 0\}} (O_{\max}(A_i) - O_{\min}(A_k)). \quad (4.3.31)$$

Note that this is an implicit definition, which must be calculated self-consistently. The starting point is given by

$$O_{\max}(A_i) = \begin{cases} n, & \text{if } A_i \text{ is targeted} \\ 0, & \text{otherwise} \end{cases} \quad (4.3.32)$$

4.3.3 Directly evaluated epCUT

So far, the epCUT algorithm produces an effective Hamiltonian as a power series in x . In recent studies, see Ref. [41], a non-perturbative evaluation of the DES showed a very robust integration even beyond the point at which the bare series begins to diverge.

The idea is to apply the epCUT algorithm in Fig. 4.3 to obtain all contributions D_{ijk} as well as the operator basis. Then, the reduction of the DES is applied. In contrast to the epCUT the flow equation is now solved for the $h_i(l)$ in Eq. (4.3.24) for all x anew, rather than for a power series in the $f_j^{(p)}(l)$. Therefore, the method is called directly evaluated epCUT (deepCUT).

The method can be viewed as a sCUT calculation with a perturbative truncation scheme. One main difference between sCUT and deepCUT is that contributions will be also truncated in the deepCUT method, whereas sCUT only truncates the operator basis. This allows deepCUT to achieve a very robust integration similar to sCUT.

Due to the recent positive results with deepCUT, we will use this method in all following chapters.

4.3.4 Transformation of observables

As mentioned before, the transformation of observables is similar to the transformation of the Hamiltonian, with the simplification that the generator is already known from the Hamiltonian transformation. The starting point is the flow equation for observables in Eq. (4.1.10). Equivalently to the expansion of the flowing Hamiltonian according to the order in x , the same can be done for the observable via

$$O(l) = \sum_i o_i(l) B_i = \sum_i \sum_{m=0}^n f_i^{(m),\text{Obs}}(l) x^m B_i. \quad (4.3.33)$$

Employing this expansion in the flow equation yields

$$\partial_l o_i(l) = \sum_{j,k} D_{ijk}^{\text{Obs}} h_j(l) o_k(l) \quad (4.3.34)$$

and accordingly

$$\partial_l f_i^{(m),\text{Obs}}(l) = \sum_{j,k} \sum_{p,q}^{p+q=m} D_{ijk}^{\text{Obs}} f_j^{(p)}(l) f_k^{(q),\text{Obs}}(l) \quad (4.3.35)$$

where the contributions D_{ijk}^{Obs} can again be calculated by the algebraic relation

$$\sum_i D_{ijk}^{\text{Obs}} B_i = [\eta[A_j], B_k]. \quad (4.3.36)$$

Note that the operator basis $\{B_i\}$ must not be the same as the Hamiltonian operator basis $\{A_i\}$, if the commutation relations between them are known.

The algorithm to calculate the contributions D_{ijk}^{Obs} is depicted in Fig. 4.4. The calculation is alike to the Hamiltonian case, with the simplification that no new generator terms can appear, which reduces the number of self-consistent runs. For $\eta^{(0)} = 0$ the algorithm is guaranteed to finish without introducing any additional truncation schemes. As in the case of the Hamiltonian, the observable DES can also be reduced. For a detailed discussion see Ref. [41].

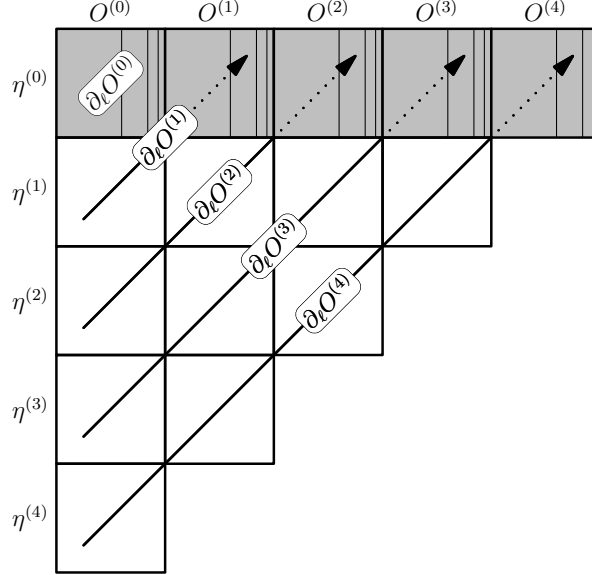


Figure 4.4: Illustration of the algorithm used to determine all contributions for the observable transformation for a given maximum order, here 4, from Ref. [41]. The boxes represent the calculation of the commutator between the different orders of the generator $\eta^{(m)}$ and the observable $O^{(n)}$ to obtain the contributions to the DES. The calculation for every order o is based on the previous orders and is achieved by calculating every commutator with $n + m = o$.

4.4 Implementation

To analyze the convergence of the CUT we introduce the residual off-diagonality (ROD). The ROD is the square root of the sum of all off-diagonal prefactors squared,

$$\text{ROD} = \sqrt{\sum_i |\eta h_i(l)|^2} \quad (4.4.37)$$

where $\eta h_i(l)$ only denotes complete coefficients that appear in the generator as well. The ROD measures the distance to diagonality and describes the speed of convergence. If l is large enough, the ROD should decrease exponentially and numerical integration can be stopped, once a critical threshold has been undercut. Several studies, however, show that the ROD does not necessarily converge if we consider a truncated system. Therefore, we will carefully study it in the case of the TFIM.

The numerical integration of the deepCUT flow equation is done by using an adaptive Runge Kutta algorithm. The flow is considered finished once the ROD falls below a critical threshold, here 10^{-10} . The typical integration range for this value is $l < 200$, however this strongly depends on the parameter J and the order of calculation.

To reduce the necessary memory several symmetries are used, see also Ref. [46, 47]. On the one hand, the number of operators to be tracked is reduced by using the same coefficient for an operator and its hermitian conjugate, due to the fact that all transformed operators show this feature. For local observables a mirror symmetry is implemented. It maps operators on the site $i + k$ to the site $i - k$, if i is the position of the local observable.

The algorithm to determine all contributions for a given order [41] as well as the calculation of dynamical correlations is implemented parallelly, using the openMP library [48].

5 String operator algebra

In the previous chapter, we explained how continuous unitary transformations are applied in a general context, for example for a hard-core bosonic algebra.

However, for the transverse field Ising model, the normal multi-particle-representation is highly disadvantageous for describing the elementary excitations. Specifically, if one aims at higher orders, the number of operators to be tracked grows exponentially, increasing the numerical effort of storing all contributions to the DES. Therefore, we will introduce a modified operator basis, which we will call string algebra. Note that this algebra is similar to the Jordan-Wigner [35] representation of the Hamiltonian.

In the following chapter we will first give a definition for the string algebra. Next we will prove that the algebra closes under the commutator. We can therefore obtain a closed form of the flow equation for the Hamiltonian. Finally, we evaluate the action of string operators on different states. This is especially interesting when transforming observables, which are not part of the string algebra.

5.1 Definition

A string operator is given by the following product of Pauli operators

$$T_n^{\phi\epsilon} := \sum_j \sigma_j^\phi \left(\prod_{k=j+1}^{j+n-1} \sigma_k^z \right) \sigma_{j+n}^\epsilon = \sum_j \sigma_j^\phi \sigma_{j+1}^z \sigma_{j+2}^z \cdots \sigma_{j+n-1}^z \sigma_{j+n}^\epsilon, \quad (5.1.1a)$$

$$\{\phi, \epsilon\} \in \{+, -\}, \quad (5.1.1b)$$

$$n \in \mathbb{N}^+. \quad (5.1.1c)$$

We can see that each string operator is a string of σ_z matrices, framed by spin flip creation- and/or annihilation-operators. We will refer to n as the range of an operator. Here, we have already chosen the translationally invariant form of string operators. When dealing with local observables it is also useful to introduce local string operators,

$$O_{j,n}^{\phi\epsilon} := \sigma_j^\phi \left(\prod_{k=j+1}^{j+n-1} \sigma_k^z \right) \sigma_{j+n}^\epsilon = \sigma_j^\phi \sigma_{j+1}^z \sigma_{j+2}^z \cdots \sigma_{j+n}^\epsilon, \quad (5.1.2a)$$

$$\{\phi, \epsilon\} \in \{+, -\}, \quad (5.1.2b)$$

$$n \in \mathbb{N}^+. \quad (5.1.2c)$$

Note that a translationally invariant string operator is given by a sum of local string operators,

$$T_n^{\phi\epsilon} = \sum_j O_{j,n}^{\phi\epsilon}. \quad (5.1.3)$$

For $n = 1$, these definitions correspond to a normal hopping term or pair creation-/annihilation-operator. For $n > 1$, the situation is slightly different. For example the case $n = 2$, $\phi = +$ and $\epsilon = -$ can be rewritten in multi-particle-representation,

$$T_1^{+-} = \sum_j \sigma_j^+ \sigma_{j+1}^z \sigma_{j+2}^- \quad (5.1.4a)$$

$$= \sum_j \sigma_j^+ (2\sigma_{j+1}^+ \sigma_{j+1}^- - 1) \sigma_{j+2}^- \quad (5.1.4b)$$

$$= \sum_j 2\sigma_j^+ \sigma_{j+1}^+ \sigma_{j+1}^- \sigma_{j+2}^- - \sigma_j^+ \sigma_{j+2}^-, \quad (5.1.4c)$$

which is the sum of a quartic interaction term and a hopping term.

This simple example already illustrates the computational advantage of the string algebra. If we tracked all operators in multi-particle-representation, a single string operator of range n would be equal to 2^{n-1} multi-particle-operators. Therefore, if the model preserves the algebra, it is convenient to describe all operators by using string operators. It is also useful to define a string operator of range 0 consisting of a single σ^z matrix.

$$T_0 := \sum_j \sigma_j^z, \quad (5.1.5a)$$

$$O_{j,0} := \sigma_j^z. \quad (5.1.5b)$$

Note that with these definitions, the Hamiltonian of the transverse field Ising model can be rewritten in terms of string operators

$$H_{\text{TFIM}} = \frac{\Gamma}{2} \sum_j \sigma_j^z + \frac{J}{4} \sum_j \sigma_j^+ \sigma_{j+1}^- + \sigma_j^+ \sigma_{j+1}^+ + \text{h.c.} \quad (5.1.6a)$$

$$= \frac{\Gamma}{2} T_0 + \frac{J}{4} (T_1^{+-} + T_1^{-+} + T_1^{++} + T_1^{--}). \quad (5.1.6b)$$

Note that we have taken the antiferromagnetic model for $J > 0$. As mentioned before this changes the properties of the model only slightly.

The computational difference between the multi-particle-representation and the string operator basis is that all local operators are represented by the basis

$$\{\sigma_j^+, \sigma_j^-, \sigma_j^z, \mathbb{1}\}, \quad (5.1.7)$$

while in the multi-particle-representation the local operator basis is given by

$$\{\sigma_j^+, \sigma_j^-, \sigma_j^+ \sigma_j^-, \mathbb{1}\}. \quad (5.1.8)$$

To further investigate the differences between the multi-particle-representation and string operators, we define a quasi-particle vacuum by

$$|0\rangle = |\cdots \downarrow_{j-1} \downarrow_j \downarrow_{j+1} \cdots\rangle, \quad (5.1.9)$$

which means that all spins in the chain point downwards. Note that this corresponds to the strong field limit in the TFIM. A single spin excitation can be created by the operator σ_l^+ . We denote this state by

$$|l\rangle = \sigma_l^+ |0\rangle. \quad (5.1.10)$$

So far, this corresponds to a normal hard-core boson multi-particle-representation picture. The difference, however, comes into play, when string operators are applied to excited states. Let us first look at the action of hopping terms on single excited states,

$$T_n^{-+} |l\rangle = \sum_j \sigma_j^- \sigma_{j+1}^z \sigma_{j+2}^z \cdots \sigma_{j+n}^+ |l\rangle \quad (5.1.11a)$$

$$= \sum_j \delta_{l,j} \sigma_{j+1}^z \sigma_{j+2}^z \cdots \sigma_{j+n}^+ |0\rangle \quad (5.1.11b)$$

$$= (-1)^{n-1} |l+n\rangle. \quad (5.1.11c)$$

In the second line we used the property $\sigma_j^- |l\rangle = \delta_{l,j} |0\rangle$. Next we know that $\sigma_j^z |0\rangle = -|0\rangle$, which gives us the final result. If there is only one quasi-particle in the system, the main difference to normal hopping operators is the factor $(-1)^{n-1}$.

For higher quasi-particle spaces we have to take into account that there might be particles on the sites $l+1, l+2 \dots l+n-1$. They will modify the exponent of (-1) and can therefore change the sign of the resulting state.

5.2 Proof of closed algebra property

In chapter 6 and 7 we will apply the method of continuous unitary transformations to the transverse field Ising model. The flow of operators is determined by commuting the Hamiltonian with the generator of the unitary transformation. Therefore it is reasonable to examine the string algebra characteristics under this operation.

In the following, we will show that the string algebra closes under the commutation. This means that the result of the commutation of two string operators can again be written as a linear combination of string operators.

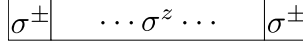


Figure 5.1: Graphical representation of a single string operator.

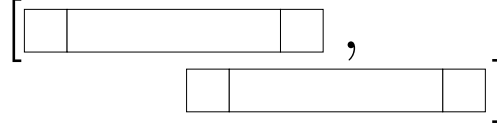


Figure 5.2: Graphical representation of the commutator of two string operators. The position of the blocks represent the different sites upon which a local string operator acts.

As we have already seen, the Hamiltonian of the transverse field Ising model can be written in terms of string operators. Later we will see that also the generator will be a sum of string operators. Therefore, our method preserves the string algebra and high order evaluations are easily accessible.

In order to simplify the proof of the closed algebra property we will introduce a graphical representation for the string algebra. A single string operator is depicted by the block in Fig. 5.1. The ends of the block represent the spin flip operators while the middle part shows the string of σ^z matrices. For commuting two string operators we write one block above the other. The positions of the blocks then represent the different sites that a local string operator acts upon.

For example Fig. 5.2 shows the commutation of two local string operators, where the lower one begins in the middle of the upper one. First, we will show that on a chain, two string operators commute if neither of their start-/end-blocks are on the same site. Without loss of generality that means that all commutators in Fig. 5.3 vanish. The last one is simply zero because operators acting on completely different sites always commute in a bosonic algebra.

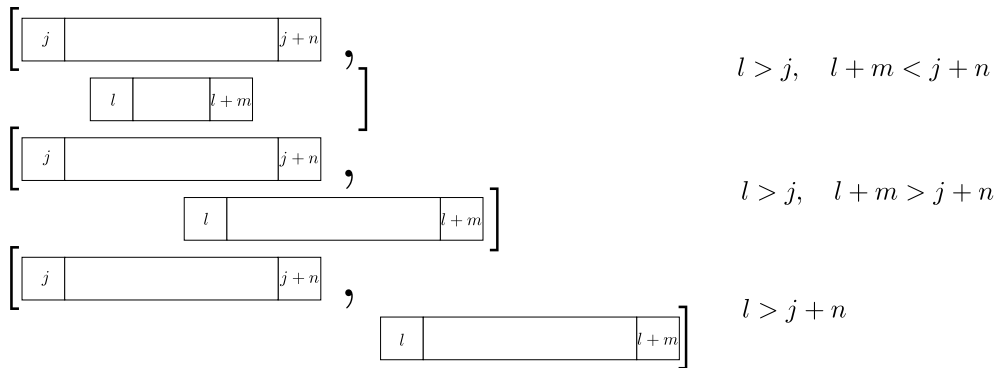


Figure 5.3: Vanishing commutators of string operators on a chain.

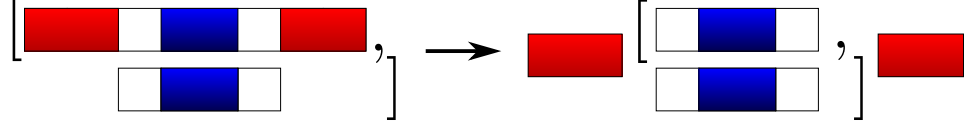


Figure 5.4: Simplifying the first commutator by factoring out (red) and multiplying the inner string operators to identity (blue).

The expression for the first commutator is given by

$$\left[O_{j,n}^{\phi\epsilon}, O_{l,m}^{\chi\xi} \right] = \left[\sigma_j^\phi \cdots \sigma_l^z \cdots \sigma_{l+m}^z \cdots \sigma_{j+n}^\epsilon, \sigma_l^\chi \cdots \sigma_{l+m}^\xi \right], \quad (5.2.12)$$

with

$$l > j, \quad l + m < j + n, \quad \phi, \epsilon, \chi, \xi \in \{+, -\} \quad (5.2.13)$$

First, all operators on sites smaller than l and greater than $l + m$ commute with all other operators and can therefore be factored out. Second, all inner parts of the string operators are σ^z matrices and therefore commute with one another. On each inner site, we have a product of two σ^z matrices, yielding $\sigma^z \sigma^z = \mathbb{1}$, see also Fig. 5.4. Therefore, only the edge operators remain. Now we use the identity $[A, BC] = [A, B]C + B[A, C]$ to simplify the result,

$$\left[O_{j,n}^{\phi\epsilon}, O_{l,m}^{\chi\xi} \right] \propto \left[\sigma_l^z \sigma_{l+m}^z, \sigma_l^\chi \sigma_{l+m}^\xi \right] \quad (5.2.14a)$$

$$= \left[\sigma_l^z \sigma_{l+m}^z, \sigma_l^\chi \right] \sigma_{l+m}^\xi + \sigma_l^\chi \left[\sigma_l^z \sigma_{l+m}^z, \sigma_{l+m}^\xi \right] \quad (5.2.14b)$$

$$= \sigma_{l+m}^z \left[\sigma_l^z, \sigma_l^\chi \right] \sigma_{l+m}^\xi + \sigma_l^\chi \sigma_l^z \left[\sigma_{l+m}^z, \sigma_{l+m}^\xi \right] \quad (5.2.14c)$$

$$= (\chi) 2 \sigma_{l+m}^z \sigma_l^\chi \sigma_{l+m}^\xi + (\xi) \sigma_l^\chi 2 \sigma_l^z \sigma_{l+m}^\xi \quad (5.2.14d)$$

$$= 2 \left\{ (\chi)(\xi) \sigma_l^\chi \sigma_{l+m}^\xi - (\chi)(\xi) \sigma_l^\chi \sigma_{l+m}^\xi \right\} \quad (5.2.14e)$$

$$= 0, \quad (5.2.14f)$$

using $[\sigma^z, \sigma^\chi] = \chi 2 \sigma^\chi$, $\sigma^z \sigma^\chi = \chi \sigma^\chi$ and $\sigma^\chi \sigma^z = -\chi \sigma^\chi$, if all operators act on the same site.

For the second commutator the starting point is the expression

$$\left[O_{j,n}^{\phi\epsilon}, O_{l,m}^{\chi\xi} \right] = \left[\sigma_j^\phi \cdots \sigma_l^z \cdots \sigma_{j+n}^\epsilon, \sigma_l^\chi \cdots \sigma_{j+n}^z \cdots \sigma_{l+m}^\xi \right] \quad (5.2.15)$$

with

$$l > j, \quad l + m > j + n. \quad (5.2.16)$$

First note that all operators on sites smaller than l and greater than $j + n$ commute with all other operators and can therefore be factored out. Secondly all operators on sites $l + 1 \dots j + n - 1$ are σ^z matrices yielding again $\sigma^z \sigma^z = \mathbb{1}$, see also Fig. 5.5.

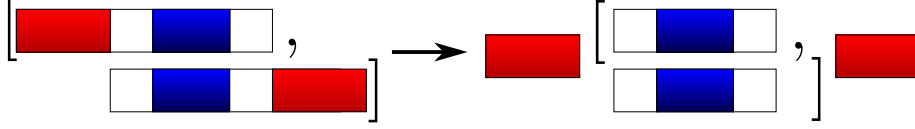


Figure 5.5: Simplifying the second commutator by factoring out (red) and multiplying the inner string operators to identity (blue).

Now we can simplify the result again,

$$[O_{j,n}^{\phi\epsilon}, O_{l,m}^{\chi\xi}] \propto [\sigma_l^z \sigma_{j+n}^\phi, \sigma_l^\chi \sigma_{j+n}^z] \quad (5.2.17a)$$

$$= [\sigma_l^z \sigma_{j+n}^\phi, \sigma_l^\chi] \sigma_{j+n}^z + \sigma_l^\chi [\sigma_l^z \sigma_{j+n}^\phi, \sigma_{j+n}^z] \quad (5.2.17b)$$

$$= \sigma_{j+n}^\phi [\sigma_l^z, \sigma_l^\chi] \sigma_{j+n}^z + \sigma_l^\chi \sigma_l^z [\sigma_{j+n}^\phi, \sigma_{j+n}^z] \quad (5.2.17c)$$

$$= 2 \left\{ -(\chi)(\phi) \sigma_l^\chi \sigma_{j+n}^\phi + (\chi)(\phi) \sigma_l^\chi \sigma_{j+n}^\phi \right\} \quad (5.2.17d)$$

$$= 0. \quad (5.2.17e)$$

Finally the case $n = 0$ is trivial, because σ^z commutes with all inner string operators. So far we have proven that only commutators for which string operators touch each other at the edge can contribute. In the following, we want to calculate these contributions exactly.

The relevant commutators are represented in Fig. 5.6. Note that all contributions coming from mirroring symmetries are also included by exchange of the arguments of the commutator. Furthermore, the edge operators of two string operators need to be different, because otherwise the identity $\sigma^+ \sigma^+ = \sigma^- \sigma^- = 0$ would yield a zero contribution. The relevant expression for the first commutator is,

$$[O_{j,n}^{\phi\epsilon}, O_{j,m}^{-\phi\xi}] = [\sigma_j^\phi \cdots \sigma_{j+m}^z \cdots \sigma_{j+n}^\epsilon, \sigma_j^{-\phi} \cdots \sigma_{j+m}^\xi], \quad (5.2.18)$$

with

$$m < n. \quad (5.2.19)$$

Again, we factor out commuting parts and combine inner σ^z matrices, see also Fig. 5.7. That implies

$$[O_{j,n}^{\phi\epsilon}, O_{j,m}^{-\phi\xi}] = [\sigma_j^\phi \sigma_{j+m}^z, \sigma_j^{-\phi} \sigma_{j+m}^\xi] \sigma_{j+m+1}^z \cdots \sigma_{j+n}^\epsilon \quad (5.2.20a)$$

$$= \left\{ [\sigma_j^\phi, \sigma_j^{-\phi}] \sigma_{j+m}^z \sigma_{j+m}^\xi + \sigma_j^{-\phi} \sigma_j^\phi [\sigma_{j+m}^z, \sigma_{j+m}^\xi] \right\} \sigma_{j+m+1}^z \cdots \sigma_{j+n}^\epsilon \quad (5.2.20b)$$

$$= \xi \sigma_{j+m}^\xi \sigma_{j+m+1}^z \cdots \sigma_{j+n}^\epsilon \quad (5.2.20c)$$

$$= \xi O_{j+m,n-m}^{\xi\epsilon}, \quad (5.2.20d)$$

which is again a string operator of range $n - m$.

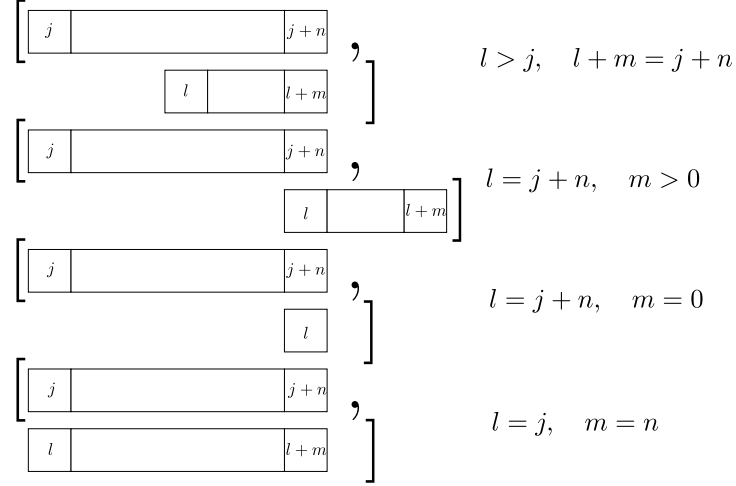


Figure 5.6: Contributing commutators of string operators on a chain. The single box in the third commutator represents a single σ^z matrix.

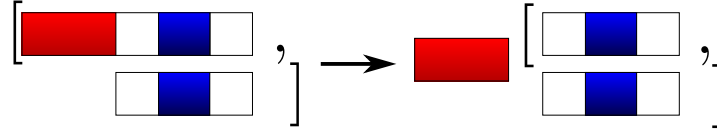


Figure 5.7: Simplifying the first contributing commutator by factoring out (red) and multiplying the inner string operators to identity (blue).

The second commutator is given by

$$[O_{j,n}^{\phi\epsilon}, O_{j+n,m}^{-\epsilon\xi}] = \sigma_j^\phi \cdots [\sigma_{j+n}^\epsilon, \sigma_{j+n}^{-\epsilon}] \cdots \sigma_{j+n+m}^\xi \quad (5.2.21a)$$

$$= \epsilon \sigma_j^\phi \cdots \sigma_{j+n}^z \cdots \sigma_{j+n+m}^\xi \quad (5.2.21b)$$

$$= \epsilon O_{j,n+m}^{\phi\xi}, \quad (5.2.21c)$$

and it is therefore a string operator of range $n + m$.

The third commutator is given by

$$[O_{j,n}^{\phi\epsilon}, O_{j+n,0}] = \sigma_j^\phi \cdots [\sigma_{j+n}^\epsilon, \sigma_{j+n}^z] \quad (5.2.22a)$$

$$= -\epsilon 2 \sigma_j^\phi \cdots \sigma_{j+n}^\epsilon \quad (5.2.22b)$$

$$= -\epsilon 2 O_{j,n}^{\phi\epsilon}, \quad (5.2.22c)$$

which remains a string operator of range n .

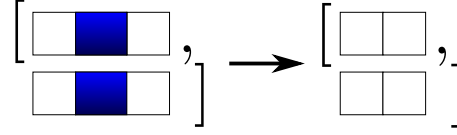


Figure 5.8: Simplifying the last contributing commutator by multiplying the inner string operators to identity (blue).

In the last case we again use the identity $\sigma^z \sigma^z = \mathbb{1}$ for all inner σ^z matrices, see also Fig. 5.8. Then we obtain the result

$$[O_{j,n}^{\phi\epsilon}, O_{j,n}^{-\phi-\epsilon}] = [\sigma_j^\phi \sigma_{j+n}^\epsilon, \sigma_j^{-\phi} \sigma_{j+n}^{-\epsilon}] \quad (5.2.23a)$$

$$= [\sigma_j^\phi \sigma_{j+n}^\epsilon, \sigma_j^{-\phi}] \sigma_{j+n}^{-\epsilon} + \sigma_j^{-\phi} [\sigma_j^\phi \sigma_{j+n}^\epsilon, \sigma_{j+n}^{-\epsilon}] \quad (5.2.23b)$$

$$= \phi \sigma_j^z \left\{ \frac{\epsilon}{2} \sigma_{j+n}^z + \frac{1}{2} \right\} + \epsilon \sigma_{j+n}^z \left\{ \frac{-\phi}{2} \sigma_j^z + \frac{1}{2} \right\} \quad (5.2.23c)$$

$$= \frac{\phi}{2} \sigma_j^z + \frac{\epsilon}{2} \sigma_{j+n}^z \quad (5.2.23d)$$

$$= \frac{\phi}{2} O_{j,0} + \frac{\epsilon}{2} O_{j+n,0} \quad (5.2.23e)$$

which is by definition (5.1.5b) the sum of two string operators of range 0.

This concludes our proof of the closing of the string algebra. We use the results for the local string operators in order to derive commutator relations for the translational invariant string operators. We begin with the case $n, m \in \mathbb{N}^+, n < m$

$$[T_n^{++}, T_m^{--}] = T_{n+m}^{+-} + T_{n+m}^{-+} - T_{m-n}^{+-} - T_{m-n}^{-+}, \quad (5.2.24a)$$

$$[T_n^{++}, T_m^{+-}] = T_{n+m}^{++} - T_{m-n}^{++} \quad (5.2.24b)$$

$$[T_n^{++}, T_m^{-+}] = T_{n+m}^{++} - T_{m-n}^{++} \quad (5.2.24c)$$

$$[T_m^{++}, T_n^{+-}] = T_{n+m}^{++} + T_{m-n}^{++} \quad (5.2.24d)$$

$$[T_m^{++}, T_n^{-+}] = T_{n+m}^{++} + T_{m-n}^{++} \quad (5.2.24e)$$

$$[T_n^{++}, T_0] = -4T_n^{++} \quad (5.2.24f)$$

$$[T_n^{++}, T_m^{++}] = 0.$$

Next we consider the case $n = m$

$$[T_m^{++}, T_m^{--}] = T_{2m}^{+-} + T_{2m}^{-+} + T_0 \quad (5.2.25a)$$

$$[T_m^{++}, T_m^{+-}] = T_{2m}^{++} \quad (5.2.25b)$$

$$[T_m^{++}, T_m^{-+}] = T_{2m}^{++} \quad (5.2.25c)$$

$$[T_m^{++}, T_m^{++}] = 0. \quad (5.2.25d)$$

All remaining cases can easily be derived by conjugating these commutator relations. With these results, we can examine the flow of the transverse field Ising model under the continuous unitary transformation.

5.3 Closed form of flow equation

Consider the representation of the transverse field Ising model in the string algebra in Eq. (5.1.6b). Without the non-particle-conserving terms $T_1^{++} + T_1^{--}$ the Hamiltonian could simply be diagonalized by Fourier transformation. Therefore, we choose the particle conserving generator η_{pc} to deduce an effective particle conserving Hamiltonian which we can diagonalize more easily.

To reach a better understanding of the continuous unitary transformation, we will first derive the three leading orders for the flow equation. Here we will already see how the flow for the transverse field Ising model is built up.

Next, we will derive a closed form of the flow equation up to infinite order. This is a remarkable step, because in general it is not possible to obtain such a closed form of the flow equation due to the large number of operators that appear in a high order calculation.

First we define the Hamiltonian during the flow by

$$H_{\text{TFIM}}(l) = t_0(l)T_0 + \sum_{n=1}^{\infty} t_n^{+-}(l) (T_n^{+-} + \text{h.c.}) + \sum_{n=1}^{\infty} t_n^{++}(l) (T_n^{++} + \text{h.c.}). \quad (5.3.26)$$

Note that the flow of the real coefficients of T_n^{++} and T_n^{--} must be the same to obtain a hermitian Hamiltonian. The same applies to T_n^{+-} and T_n^{-+} . For the sake of clarity we omit the dependence of the coefficients on the flow parameter l in the following examinations.

Comparison of the coefficients with Eq. (5.1.6b) yields the initial conditions

$$t_0 \big|_{l=0} = \frac{\Gamma}{2}, \quad (5.3.27a)$$

$$t_1^{+-} \big|_{l=0} = \frac{J}{4}, \quad (5.3.27b)$$

$$t_1^{++} \big|_{l=0} = \frac{J}{4}, \quad (5.3.27c)$$

$$t_n^{+-} \big|_{l=0} = t_n^{++} \big|_{l=0} = 0, n > 1. \quad (5.3.27d)$$

We start our study in the strong field limit $J \rightarrow 0$. Therefore, the energy scale is given by Γ and the dimensionless perturbation parameter is $x = \frac{J}{\Gamma}$. Observe that all non particle conserving terms are at least of order one, hence we have no generator term $\eta^{(0)}$.

Furthermore we can identify the starting blocks

$$H^{(0)} = T_0, \quad (5.3.28a)$$

$$H^{(1)} = (T_1^{+-} + \text{h.c.}) + (T_1^{++} + \text{h.c.}), \quad (5.3.28b)$$

$$\eta^{(1)} = T_1^{++} - \text{h.c.} \quad (5.3.28c)$$

Following the epCUT algorithm in Fig. 4.3, we first calculate the block $[\eta^{(1)}, H^{(0)}]$ until self-consistency is reached,

$$[\eta^{(1)}, H^{(0)}] = [T_1^{++} - \text{h.c.}, T_0] \quad (5.3.29a)$$

$$= -4 (T_1^{++} + \text{h.c.}). \quad (5.3.29b)$$

Obviously no new terms appear and the result is self-consistent. Because we have no term $\eta^{(0)}$, our first order calculation is already finished, resulting in the first order flow equation

$$\partial_l t_0 = 0, \quad (5.3.30a)$$

$$\partial_l t_1^{+-} = 0, \quad (5.3.30b)$$

$$\partial_l t_1^{++} = -4t_1^{++}t_0. \quad (5.3.30c)$$

Note that all other coefficients $t_n^{\pm\pm}, n > 1$ remain constant in first order. This differential equation has the exact solution $t_0 = \text{const}, t_1^{+-} = \text{const}, t_1^{++} = -J/4 \exp(-4t_0 l)$, resulting in the final values

$$t_0 \big|_{l=\infty} = \frac{\Gamma}{2}, \quad (5.3.31a)$$

$$t_1^{+-} \big|_{l=\infty} = \frac{J}{4}, \quad (5.3.31b)$$

$$t_1^{++} \big|_{l=\infty} = 0. \quad (5.3.31c)$$

This simple calculation shows us that on the one hand the CUT indeed decouples the vacuum state from multi-particle states. On the other hand it, shows us that there are no corrections to the ground state energy in first order, because the term t_0 remains constant.

For the second order we begin with the block $[\eta^{(1)}, H^{(1)}]$ to obtain second order terms,

$$[\eta^{(1)}, H^{(1)}] = [T_1^{++} - \text{h.c.}, T_1^{++} + T_1^{+-} + \text{h.c.}] \quad (5.3.32a)$$

$$= 2 (T_2^{+-} + \text{h.c.}) + 2T_0 + 2 (T_2^{++} + \text{h.c.}) \quad (5.3.32b)$$

Here we see that the new terms $T_2^{+-} + \text{h.c.}$ and $T_2^{++} + \text{h.c.}$ appear. They are of minimal order $O_{\min} = 2$. The latter one is not particle conserving and must be added to the

generator $\eta^{(2)}$. Furthermore we have a first correction to the ground state by the term T_0 . Now we calculate the block $[\eta^{(2)}, H^{(0)}]$ self consistently,

$$[\eta^{(2)}, H^{(0)}] = [T_2^{++} + \text{h.c.}, T_0] \quad (5.3.33a)$$

$$= -4 (T_2^{++} + \text{h.c.}) . \quad (5.3.33b)$$

Again, no new terms appear after the commutation, therefore we have obtained all contributions for the second order. This implies the following set of flow equations

$$\partial_t t_0 = 2t_1^{++}t_1^{++}, \quad (5.3.34a)$$

$$\partial_t t_1^{+-} = 0, \quad (5.3.34b)$$

$$\partial_t t_2^{+-} = 2t_1^{++}t_1^{++}, \quad (5.3.34c)$$

$$\partial_t t_1^{++} = -4t_1^{++}t_0, \quad (5.3.34d)$$

$$\partial_t t_2^{++} = 2t_1^{++}t_1^{+-} - 4t_2^{++}t_0. \quad (5.3.34e)$$

For the third order, the relevant commutators yield

$$[\eta^{(1)}, H^{(2)}] = [T_1^{++} - \text{h.c.}, T_2^{++} + T_2^{+-} + \text{h.c.}] , \quad (5.3.35a)$$

$$= -2T_1^{++} + 2T_3^{++} + 2T_3^{+-} - 2T_1^{+-} + \text{h.c.}, \quad (5.3.35b)$$

$$[\eta^{(2)}, H^{(1)}] = [T_2^{++} - \text{h.c.}, T_1^{++} + T_1^{+-} + \text{h.c.}] , \quad (5.3.35c)$$

$$= 2T_1^{++} + 2T_3^{++} + 2T_3^{+-} - 2T_1^{+-} + \text{h.c.}, \quad (5.3.35d)$$

$$[\eta^{(3)}, H^{(0)}] = [T_3^{++} - \text{h.c.}, T_0] , \quad (5.3.35e)$$

$$= -4 (T_3^{++} + \text{h.c.}) . \quad (5.3.35f)$$

Thus, we obtain the flow equation up to the third order

$$\partial_t t_0 = 2t_1^{++}t_1^{++}, \quad (5.3.36a)$$

$$\partial_t t_1^{+-} = -4t_1^{++}t_2^{++}, \quad (5.3.36b)$$

$$\partial_t t_2^{+-} = 2t_1^{++}t_1^{++}, \quad (5.3.36c)$$

$$\partial_t t_3^{+-} = 4t_1^{++}t_2^{++}, \quad (5.3.36d)$$

$$\partial_t t_1^{++} = -4t_1^{++}t_0 - 2t_1^{++}t_2^{+-} + 2t_2^{++}t_1^{+-}, \quad (5.3.36e)$$

$$\partial_t t_2^{++} = 2t_1^{++}t_1^{+-} - 4t_2^{++}t_0, \quad (5.3.36f)$$

$$\partial_t t_3^{++} = 2t_1^{++}t_2^{+-} + 2t_2^{++}t_1^{+-} - 4t_3^{++}t_0. \quad (5.3.36g)$$

Evaluating these first three expansions, it is possible to find the pattern for the contributions to the flow equation. We extend the flow equation up to infinite order

$$\partial_l t_0 = 2 \sum_{n=1}^{\infty} (t_n^{++})^2, \quad (5.3.37a)$$

$$\partial_l t_m^{+-} = 2 \sum_{k,l}^{k+l=m} t_k^{++} t_l^{++} - 2 \sum_{k,l}^{|k-l|=m} t_k^{++} t_l^{++}, \quad (5.3.37b)$$

$$\partial_l t_m^{++} = -4t_m^{++} t_0 + 2 \sum_{k,l}^{|k-l|=m} \text{sgn}(k-l) t_k^{++} t_l^{+-} + 2 \sum_{k,l}^{k+l=m} t_k^{++} t_l^{+-}, \quad (5.3.37c)$$

$$m, k, l \in \mathbb{N}^+. \quad (5.3.37d)$$

To prove this expression we will proceed in two steps. First, we show that all kinds of string operators of arbitrary range will be created during the flow. Next we show which contributions to the DES are created.

Our starting point for step one is the Hamiltonian of the TFIM in string operators in Eq. (5.1.6b). By induction we show that once we have a complete set of operators of maximum range n , $T_0, T_1^{\pm\pm}, T_2^{\pm\pm}, \dots, T_n^{\pm\pm}$ we can create a new complete set of operators of range $n+1$ by commutation with a string pair-creation-operator,

$$[T_n^{++}, T_1^{--}] = T_{n+1}^{+-} + T_{n+1}^{-+} - T_{n-1}^{+-} - T_{n-1}^{-+}, \quad (5.3.38a)$$

$$[T_n^{++}, T_1^{+-}] = T_{n+1}^{++} - T_{n-1}^{++}, \quad (5.3.38b)$$

$$[T_n^{--}, T_1^{-+}] = -T_{n+1}^{--} + T_{n-1}^{--}. \quad (5.3.38c)$$

As we can see, we have created all new string operators of range $n+1$. Because the Hamiltonian in Eq. (5.1.6b) already comprises a complete set of range unity we can deduce that all ranges $n \in \mathbb{N}^+$ will be created during the flow. Hence, we can conclude for the generator of the TFIM

$$\eta = \sum_{n=1}^{\infty} t_n^{++} (T_n^{++} - T_n^{--}). \quad (5.3.39)$$

For step two we consider the relations in Eq. (5.2.24) and Eq. (5.2.25). We start with the contributions to the operator T_0 . As we can see T_0 will be created only in the case $m=n$. For a given range n there are two contributions from the commutators

$$[T_n^{++}, T_n^{--}] = T_0 + \dots, \quad (5.3.40a)$$

$$[T_n^{--}, T_n^{++}] = -T_0 + \dots \quad (5.3.40b)$$

both with prefactor one. Note that T_n^{++} and T_n^{--} share the same prefactor up to a sign due to hermiticity/anti-hermiticity. Finally these considerations yield for the flow

equation for the prefactor of T_0

$$\partial_l t_0 = 2 \sum_{n=1}^{\infty} (t_n^{++})^2. \quad (5.3.41)$$

Next we consider the operator T_m^{+-} and T_m^{-+} , respectively. They are created by two different kinds of commutators, first

$$[T_k^{++}, T_l^{--}] = T_m^{+-} + \dots \quad \text{with } k+l=m, \quad (5.3.42a)$$

$$[T_k^{--}, T_l^{++}] = -T_m^{+-} + \dots \quad \text{with } k+l=m, \quad (5.3.42b)$$

and second

$$[T_k^{++}, T_l^{--}] = -T_m^{+-} + \dots \quad \text{with } |k-l|=m, \quad (5.3.43a)$$

$$[T_k^{--}, T_l^{++}] = T_m^{+-} + \dots \quad \text{with } |k-l|=m, \quad (5.3.43b)$$

all with prefactor one. Note that the operator T_m^{-+} shares the same prefactor as T_m^{+-} . These calculations yield

$$\partial_l t_m^{+-} = 2 \sum_{k,l}^{k+l=m} t_k^{++} t_l^{++} - 2 \sum_{k,l}^{|k-l|=m} t_k^{++} t_l^{++}. \quad (5.3.44)$$

Last we consider the operator T_m^{++} and T_m^{--} , respectively. They are created by three different kinds of commutators, first

$$[T_k^{++}, T_l^{+-}] = T_m^{++} + \dots \quad \text{with } k+l=m, \quad (5.3.45a)$$

$$[T_k^{++}, T_l^{-+}] = T_m^{++} + \dots \quad \text{with } k+l=m, \quad (5.3.45b)$$

second

$$[T_k^{++}, T_l^{+-}] = \text{sgn}(k-l) T_m^{++} + \dots \quad \text{with } |k-l|=m, \quad (5.3.46a)$$

$$[T_k^{++}, T_l^{-+}] = \text{sgn}(k-l) T_m^{++} + \dots \quad \text{with } |k-l|=m, \quad (5.3.46b)$$

note that the sign function comes from the different signs in the cases $[T_n^{++}, T_m^{+-}]$ and $[T_m^{++}, T_n^{+-}]$ in Eq. (5.2.24). Finally the third case is given by

$$[T_m^{++}, T_0] = -4T_m^{++}. \quad (5.3.47)$$

Now we can write down the flow equation for the prefactor t_m^{++} ,

$$\partial_l t_m^{++} = -4t_m^{++} t_0 + 2 \sum_{k,l}^{|k-l|=m} \text{sgn}(k-l) t_k^{++} t_l^{+-} + 2 \sum_{k,l}^{k+l=m} t_k^{++} t_l^{+-}, \quad (5.3.48)$$

which concludes our derivation for the flow equation for infinite order.

This result is remarkable considering that it would include tremendously more flow parameters if we formulated the problem in multi-particle-representation. It also allows us to evaluate the Hamiltonian transformation for very high orders, which is especially interesting in the vicinity of the quantum critical point $J = 2\Gamma$.

5.4 Evaluation of effective models within the string algebra

In this section we explain how to evaluate the resulting effective Hamiltonian, for example how to obtain the ground state energy per site or the dispersion relation. Additionally, we want to elaborate on how the CUT transforms observables. This is interesting regarding measurable quantities such as the magnetization or spectral properties.

After the CUT, the effective Hamiltonian takes the form

$$H(l)|_{l=\infty} = t_0(\infty)T_0 + \sum_n t_n^{+-}(\infty) (T_n^{+-} + \text{h.c.}) \quad (5.4.49)$$

Note that terms of the form $T_n^{++} + \text{h.c.}$ are rotated away by the CUT and do not contribute to the final Hamiltonian. Therefore, the particle vacuum $|0\rangle$ now represents the ground state of the effective Hamiltonian. This leads to the ground state energy per site with the expression

$$\frac{1}{N}H(\infty)|0\rangle = \frac{1}{N}t_0(\infty)T_0|0\rangle \quad (5.4.50a)$$

$$= \frac{1}{N}(-N)t_0(\infty)|0\rangle \quad (5.4.50b)$$

$$= -t_0(\infty)|0\rangle. \quad (5.4.50c)$$

We have used the property $T_n^{+-}|0\rangle = T_n^{-+}|0\rangle = 0$. As a result the ground state energy is simply given by the coefficient $\frac{E_0}{N} = -t_0(\infty)$ and can easily be read out after the CUT. Next, we consider the dispersion relation for a single excitation in the system. Thereby we define a Fourier transformed spin flip with momentum Q

$$|Q\rangle = \frac{1}{\sqrt{N}} \sum_n e^{iQn} |n\rangle, \quad (5.4.51)$$

and examine the action of the Hamiltonian on this state

$$H(\infty) |Q\rangle = \sum_n e^{iQn} \left\{ t_0(\infty) T_0 + \sum_{n'} t_{n'}^{+-}(\infty) (T_{n'}^{+-} + \text{h.c.}) \right\} |n\rangle \quad (5.4.52a)$$

$$= \sum_n e^{iQn} \left\{ t_0(\infty) (-N + 2) |n\rangle + \sum_{n'} t_{n'}^{+-}(\infty) (-1)^{n'-1} (|n - n'\rangle + |n + n'\rangle) \right\} \quad (5.4.52b)$$

$$= (E_0 + 2t_0(\infty)) |Q\rangle + \sum_{n'} \sum_n t_{n'}^{+-}(\infty) (-1)^{n'-1} \left\{ e^{iQ(n+n')} + e^{iQ(n-n')} \right\} |n\rangle \quad (5.4.52c)$$

$$= \left(E_0 + 2t_0(\infty) + \sum_{n'} 2t_{n'}^{+-}(\infty) (-1)^{n'-1} \cos(Q) \right) |Q\rangle, \quad (5.4.52d)$$

which is again an eigenstate of the Hamiltonian. The dispersion is therefore given by the Fourier sum of hopping coefficients except for a sign

$$\omega(Q) = 2t_0(\infty) + \sum_{n'} 2t_{n'}^{+-}(\infty) (-1)^{n'-1} \cos(Q). \quad (5.4.53)$$

To obtain quantities such as the magnetization we also have to transform observables via the CUT to effective observables. If the observable is part of the string algebra, the problem is again simplified due to the closed algebra property. For example, this is the case for the transverse magnetization

$$M_z = \langle 0 | \sigma_{\text{eff}}^z | 0 \rangle, \quad (5.4.54a)$$

$$\sigma_{\text{eff}}^z = U^\dagger(l) \sigma^z U(l) \big|_{l=\infty}. \quad (5.4.54b)$$

Another possibility to obtain the transverse magnetization is via the groundstate energy,

$$\sum_j \sigma_j^z = \frac{H}{\Gamma} - \frac{J}{\Gamma} \frac{dH}{dJ}, \quad (5.4.55a)$$

$$\Rightarrow M_z = \frac{E_0}{\Gamma N} - \frac{J}{\Gamma N} \frac{dE_0}{dJ}. \quad (5.4.55b)$$

In contrast to this, the magnetization along x is more complicated, because the corresponding observable $\sigma^x = \sigma^+ + \sigma^-$ is not part of the string algebra. But due to the fact that the flow of the Hamiltonian is very compact in the string algebra, we stay within the local basis (5.1.7) in order to transform such observables.

This observation is in agreement with the fermionic representation of the transverse field Ising model employed by the Jordan-Wigner transformation. There the observable σ^x is represented by an extremely non-local string of operators acting upon an extensive number of lattice sites. By staying in the spin picture, we avoid this problem at the cost

of a more complex, but local operator structure. Specifically, such an observable can have terms of the form

$$\sigma_{\text{eff}}^x \propto \sum_j \left(\sigma_j^+ \prod_{lmn\dots} \sigma_k^z \sigma_l^z \sigma_m^z \cdots + \text{h.c.} \right) \quad (5.4.56a)$$

$$+ \sum_{jko} \left(\sigma_j^+ \sigma_k^+ \sigma_o^+ \prod_{lmn\dots} \sigma_k^z \sigma_l^z \sigma_m^z \cdots + \text{h.c.} \right) \quad (5.4.56b)$$

$$+ \sum_{jko} \left(\sigma_j^+ \sigma_k^+ \sigma_o^- \prod_{lmn\dots} \sigma_k^z \sigma_l^z \sigma_m^z \cdots + \text{h.c.} \right) \quad (5.4.56c)$$

$$+ \dots, \quad (5.4.56d)$$

after the CUT. Here the indices j, k, l, m, n, o denote lattice sites that are not necessary adjacent. In a finite order calculation the number and range of operators remain finite, hence they are not extensive.

Note that the generator includes only even numbers of creation-/annihilation-operators. Therefore, the generator preserves the parity of an observable, i.e., the number of particles is only changed in multiples of two. If such an operator acts upon the vacuum $|0\rangle$ we can easily calculate the resulting state

$$\sigma_{\text{eff}}^x |0\rangle \propto \underbrace{\sum_j (-1)^{\#\sigma^z} |j\rangle}_{1 \text{ particle excitations}} + \underbrace{\sum_{jko} (-1)^{\#\sigma^z} |jko\rangle}_{3 \text{ particle excitations}} + \dots \quad (5.4.57)$$

where $\#\sigma^z$ denotes the number of σ^z matrices in an operator.

6 Static results

In this chapter we present and evaluate the static results for the transverse field Ising model. The expression 'static' refers to properties which are time-independent, such as the ground state energy per site, the energy dispersion or the magnetization. At first, we look at the residual off diagonality (ROD). This gives us an overview for the numerical errors we can expect due to the fact that we can not integrate up to $l = \infty$. We investigate how the CUT behaves directly at the critical point $J = 2\Gamma$, where the energy gap closes.

Next we discuss the ground state energy and compare the results for different orders with the exact results given by Pfeuty [31]. The energy dispersion is evaluated for different orders and values of J and it is again compared to the exact results. With the help of the dispersion we can also obtain the energy gap as a function of J .

Finally, we look at the transverse magnetization M_z obtained by an observable transformation.

6.1 Convergence of CUT

To monitor the convergence of the CUT, we previously introduced the residual off diagonality (ROD) in (4.4.37). Since all off diagonal terms also appear in the generator, the ROD also serves as a norm for the generator.

For a system of finite size and a finite energy gap we generally expect that the ROD decreases exponentially. We will see that this also holds for the TFIM if we stay below the critical value $J = 2\Gamma$.

Once the ROD reaches a critical threshold (here 10^{-10}), we consider the CUT completed and stop the integration. The point in l where the threshold is reached strongly depends on our expansion parameter J and the order of calculation.

A generic behaviour of the CUT is depicted in Fig. 6.1. Notice that the ROD is decreasing exponentially. The effect of different orders becomes conspicuous above $l \approx 2$. Increasing the parameter J has an even more significant effect, as we can see in Fig. 6.2. On the one hand, the initial value of the ROD at $l = 0$ rises, because the initial Hamiltonian has a larger off-diagonal part. On the other hand, the speed of the exponential decay decreases with higher values of J . This is expected, because the energy gap begins to decrease.

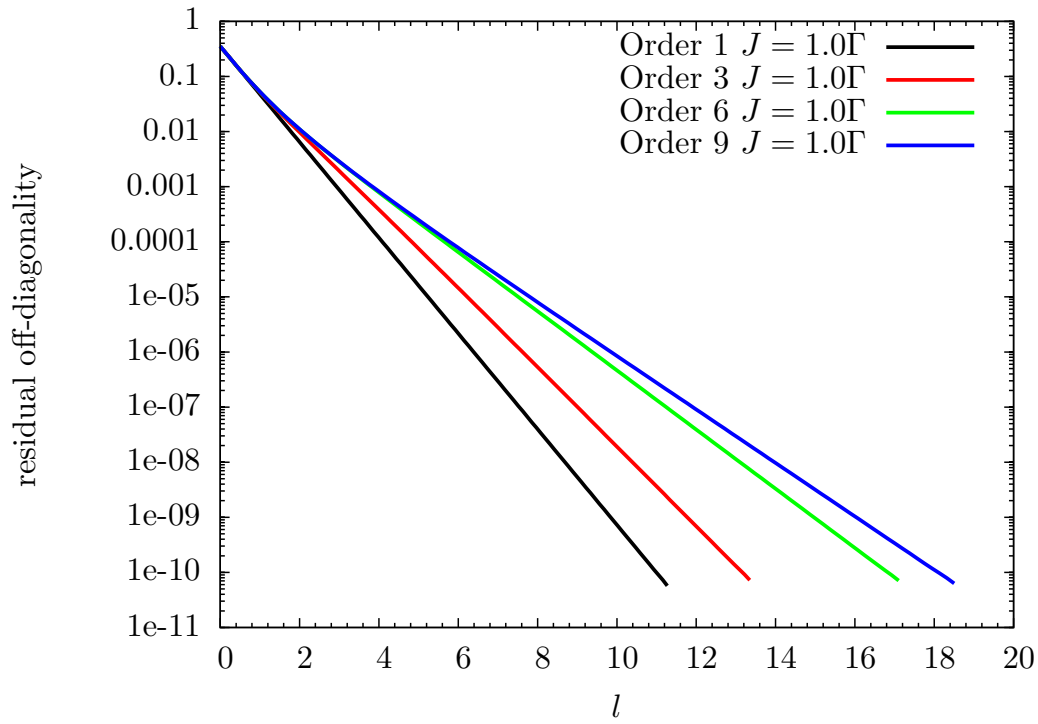


Figure 6.1: ROD for different orders and a fixed value of $J = 1.0\Gamma$.

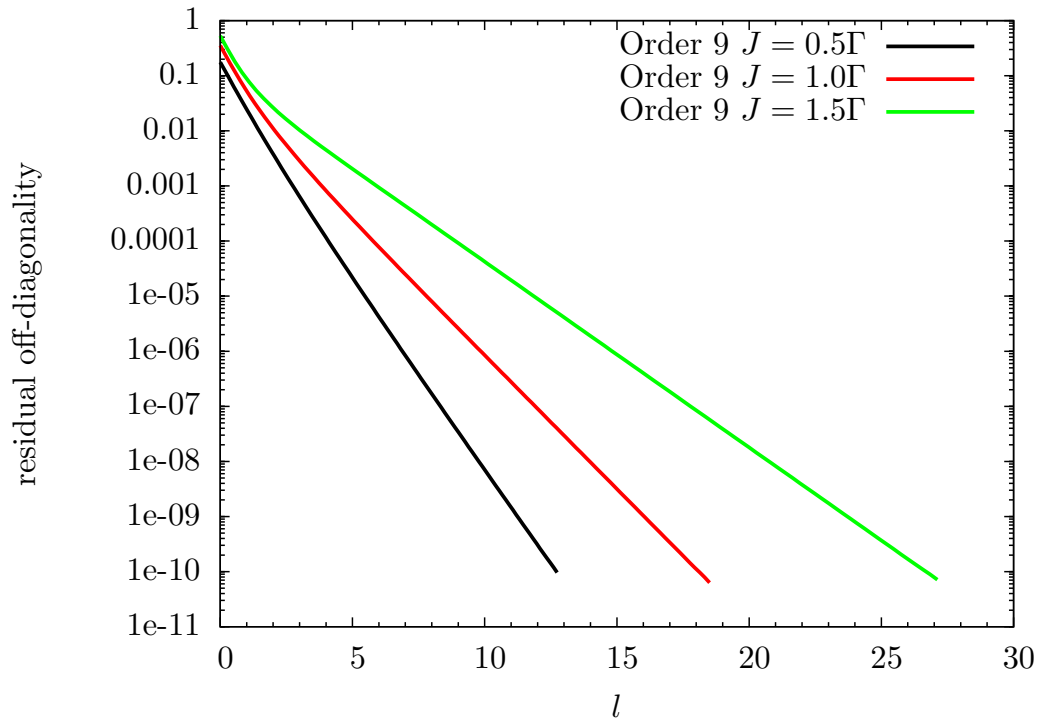


Figure 6.2: ROD for different values of J and a fixed order.

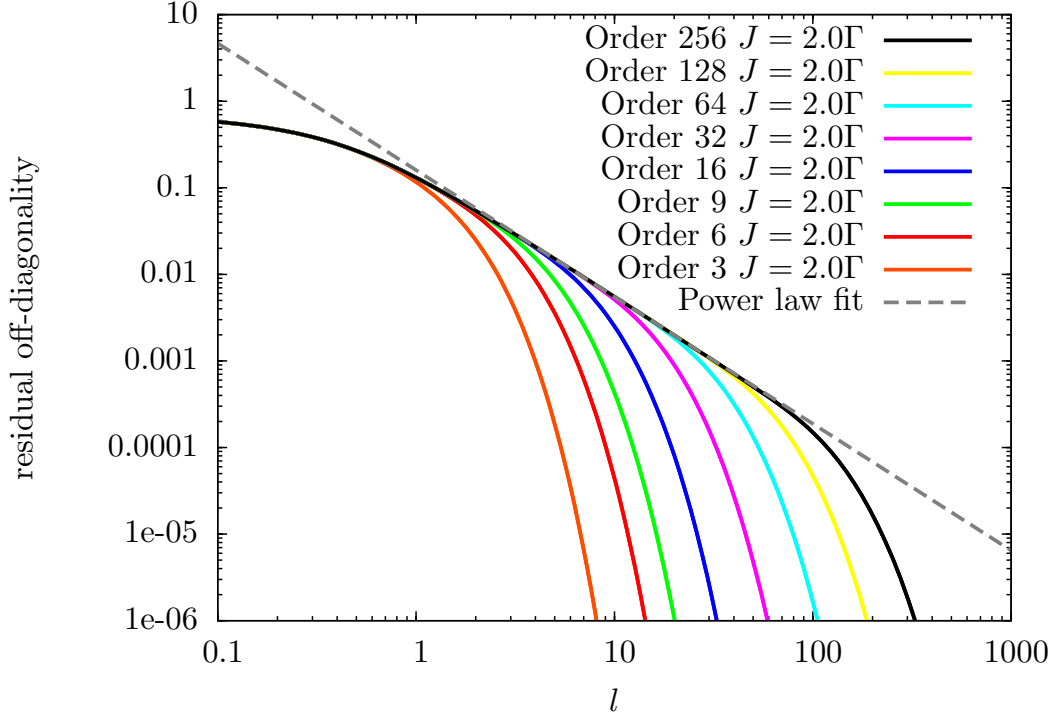


Figure 6.3: ROD at the critical point $J = 2\Gamma$ for different orders.

In general, for $J \neq 2\Gamma$, the CUT always converges exponentially. Therefore, we do not need to introduce special generators such as the $n : m$ generators in Ref. [26]. On the other hand, upon approaching the critical point $J = 2\Gamma$, the threshold value of l begins to rise, resulting in more time consuming numerical integration.

At the critical point the energy gap of the TFIM closes. In an exact CUT calculation we would now only expect an algebraic decrease of the ROD. Due to the fact that we exclusively consider finite order calculations, this behaviour is only true for small values of l .

This effect is depicted in Fig. 6.3. It shows the ROD at the critical point $J = 2\Gamma$ for different orders. First, note that both scales are logarithmic, which implies that straight lines represent power laws. Therefore, the envelope of all orders is an algebraic declining function, as expected for an exact CUT. The power law fit reveals an exponent of 1.5 ± 0.4 . For higher values of l all RODs show an exponential decay, which implies that for all finite orders the CUT still “sees” an effective gap. Due to the truncation of the differential equation system, this error is suppressed with increasing order. Finally, note that the threshold value of l for an order 256 at the critical point is about a factor 50 greater than the threshold value for an order 9 at $J = 0.5\Gamma$. This reinforces our previous statement concerning the rise of the threshold value of l .

When going beyond the phase transition, the ROD again declines exponentially, but much more slower than in the disordered phase. Furthermore, much of the weight is concentrated in matrix elements connecting high ranges in real space. Therefore our perturbative truncation scheme ignores many of the important physical processes. This can be explained by the fact, that in the limit $J \rightarrow \infty$, the elementary excitations are

non-local domain walls. Within our localized description based on spin-flips, the CUT is not able to catch this feature of the TFIM.

This should, however, not be seen as a general disadvantage of our method, because with an adapted quasi-particle picture, such as a Kramers-Wannier duality transformation [49], it should also be possible to describe the ordered phase with CUT.

6.2 Ground state energy

To evaluate the ground state energy of our effective, quasi-particle conserving model, we refer the reader to Eq. (5.4.50). An exact expression for the ground state energy per site was calculated by Pfeuty [31], see Eq. (3.2.15). As mentioned before, it is possible to reach very high orders within the string operator framework. We were therefore able to obtain the ground state energy per site up to order 256.

In the context of perturbative expansions for more complex models, this is a very high order. Due to the fact that the number of representatives only rises linearly even higher orders are accessible. Higher orders, however, do not improve the results significantly, therefore we restrict ourselves up to order 256. It is worth emphasizing that the phase transition at $J = 2\Gamma$ can not be described with any finite order calculation.

Figure 6.4 shows the exact result for the ground state energy per site in comparison to various orders for the CUT. As expected, the precision of the CUT increases with higher orders. Even close to the QCP the CUT of order 128 and the exact results can barely be separated from each other.

To make a more quantitative statement we investigate the absolute difference of the CUT calculation to the exact curve,

$$\Delta \frac{E_0}{\Gamma N} = \frac{|E_0 - E_{0,(\text{CUT})}|}{\Gamma N}. \quad (6.2.1)$$

This quantity is depicted in Fig. 6.5. First, note that we have taken the logarithm of both, $\Delta \frac{E_0}{\Gamma N}$ and J . Consequently straight lines represent power laws,

$$\Delta \frac{E_0}{\Gamma N} = Ax^P, \quad (6.2.2a)$$

$$\Rightarrow \log \left(\Delta \frac{E_0}{\Gamma N} \right) = \log(A) + P \log(x). \quad (6.2.2b)$$

In this logarithmic scale, the QCP is located at $\log_{10} \left(\frac{J}{2\Gamma} \right) = 0$. A closer analysis reveals that with increasing order, the ground state energy is obtained more and more accurately. Furthermore all orders follow a power law whose exponent increases with the order. This is reasonable because in a perturbative expansion we expect the errors to be in $\mathcal{O}(x^{\text{order}+1})$.

By fitting the curves to linear functions, using the Levenberg-Marquardt algorithm [50, 51], we obtain the exponents of the power laws. They are reported in Tab. 6.1.

Ground state energy exponents		
Order	Exponent	Fitting Error
9	10	± 3
16	21	± 4
32	33	± 3
64	72	± 6
128	132	± 5

Table 6.1: Exponents of the power laws for the ground state energy obtained by fitting linear functions.

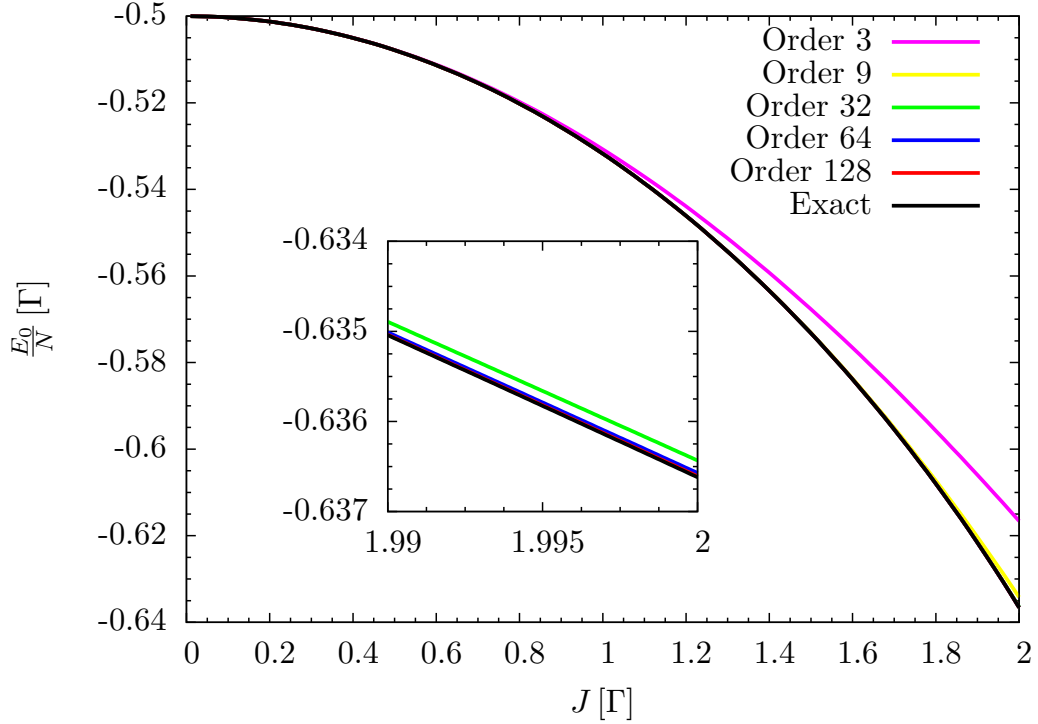


Figure 6.4: Ground state energy per site as function of J . Comparison of the exact result with various CUT orders.

As expected, the exponents are at least above and close the order of the calculation. Additionally we want to investigate how the ground state energy of the effective model evolves above the QCP. As explained before, beyond this point our quasi-particle picture breaks down and we can not expect to obtain a quantitatively correct answer. For low orders < 64 this holds true but surprisingly the ground state energy for higher orders is described qualitatively correct, see also Fig. 6.6. Naturally, we are not able to achieve a precision of $< 10^{-10}$ as we did in the disorder phase. Nevertheless, the value is correct up to 10^{-2} for an order 256 even at the point $J = 4\Gamma$.

A possible explanation is the fact that the ground state energy is a fairly robust quantity even beyond the QCP.

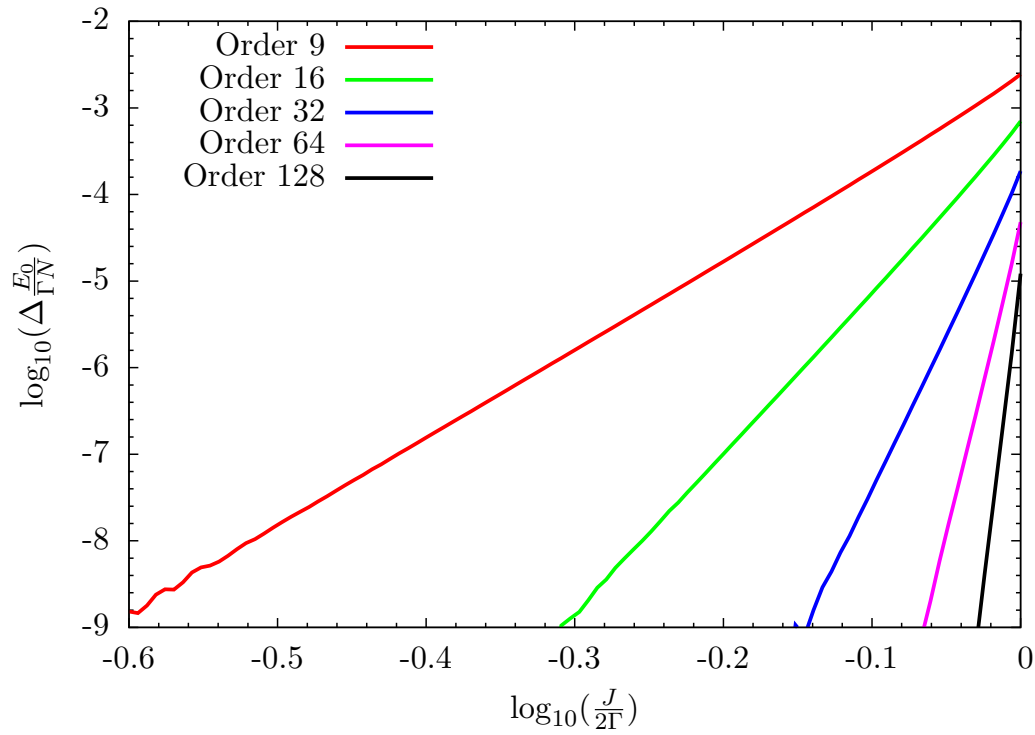


Figure 6.5: Absolute difference between the exact ground state energy per site and the CUT calculation as function of J . The QCP is located at $\log_{10} \left(\frac{J}{2\Gamma} \right) = 0$.

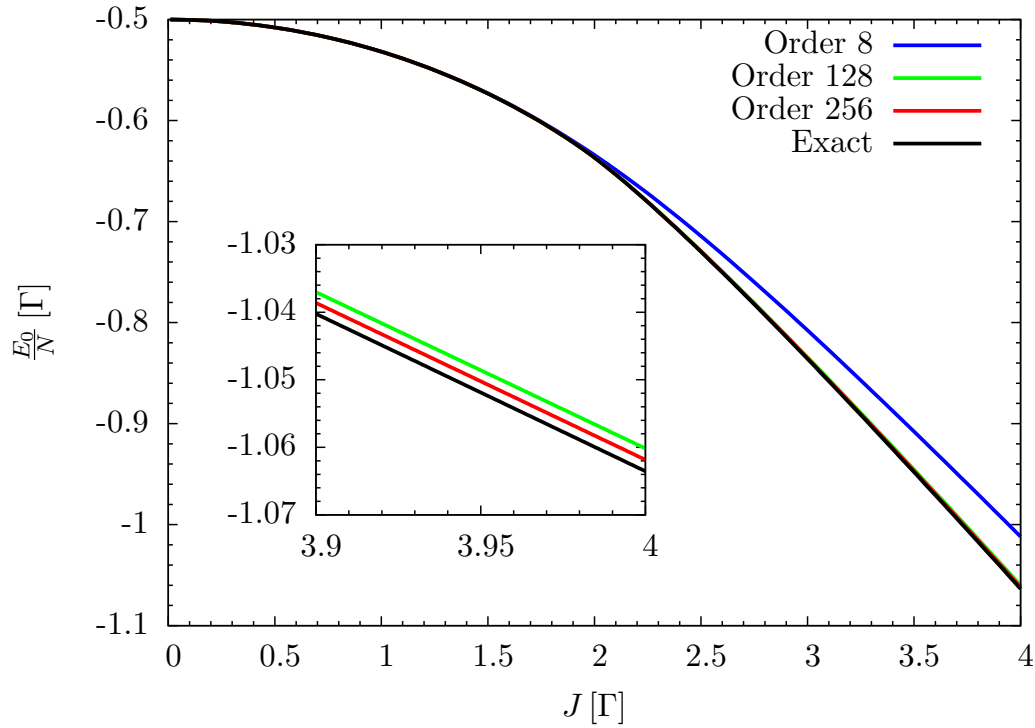


Figure 6.6: Ground state energy per site as function of J above the QCP. Comparison of the exact result with various CUT orders.

6.3 Dispersion

In this section we consider the results for the energy dispersion of the TFIM. We refer the reader to eq. (5.4.53) on how to obtain the energy dispersion from the effective Hamiltonian.

The exact dispersion is given by the simple expression

$$\omega(q) = \Gamma \sqrt{1 + \frac{J^2}{4\Gamma^2} + \frac{J}{\Gamma} \cos(q)}, \quad (6.3.3)$$

see also Ref. [31]. Expanding this expression in the Parameter $x = J/\Gamma$ yields

$$\frac{\omega(q)}{\Gamma} = 1 + \frac{1}{2} \cos(q)x + \frac{1}{16} (1 - \cos(2q))x^2 + \frac{1}{64} (-\cos(k) + \cos(3q))x^3 + \mathcal{O}(x^4). \quad (6.3.4)$$

This shows us that hopping processes of even/odd parity appear only in even/odd orders. The dispersion is an important quantity that can also be measured in experiments. We will later see that the dispersion determines the position of the one-particle dynamical structure factor in frequency space.

As before we were able to reach order 256 for the CUT calculation. Therefore we obtain hopping matrix elements up to a maximum range of 256. For small parameters J , a low order calculation is sufficient to achieve a good agreement with the exact result. This is depicted in Fig. 6.7 and Fig. 6.8. Closer to the QCP this changes distinctly, see Fig. 6.9 and Fig. 6.10, which makes higher order calculations necessary. Directly at the QCP we are able to obtain the correct result within 10^{-5} over a large part of the Brillouin zone.

This behaviour is expected, because the excitations become more and more dispersive with increasing parameter J . Consequently, the correlation length increases rapidly close to the QCP and hopping processes over more and more sites become important. To include these physical processes we need higher orders, because the maximum range that we can describe directly corresponds to the order of calculation.

A closer look exactly at the QCP also reveals that our calculation of the dispersion is worst in the region of the critical wave vector $q = \pi$. Here, the energy gap closes and our quasi-particle picture breaks down, see insets of Fig. 6.9 and Fig. 6.10.

Similar to the ground state energy we investigate how CUT predicts the dispersion above the QCP. In the limit of $J \rightarrow \infty$ the elementary excitations become domain walls. Domain walls are non-local in terms of spin flip excitations and they are not expected to be described correctly by the CUT. Figure 6.11 shows the exact dispersion at $J = 2.5\Gamma$ and the CUT calculation of order 256. Interestingly, the CUT describes the upper half of the dispersion with a precision of 0.001, but when approaching the critical wave vector $q = \pi$ the result strongly differs from the exact one.

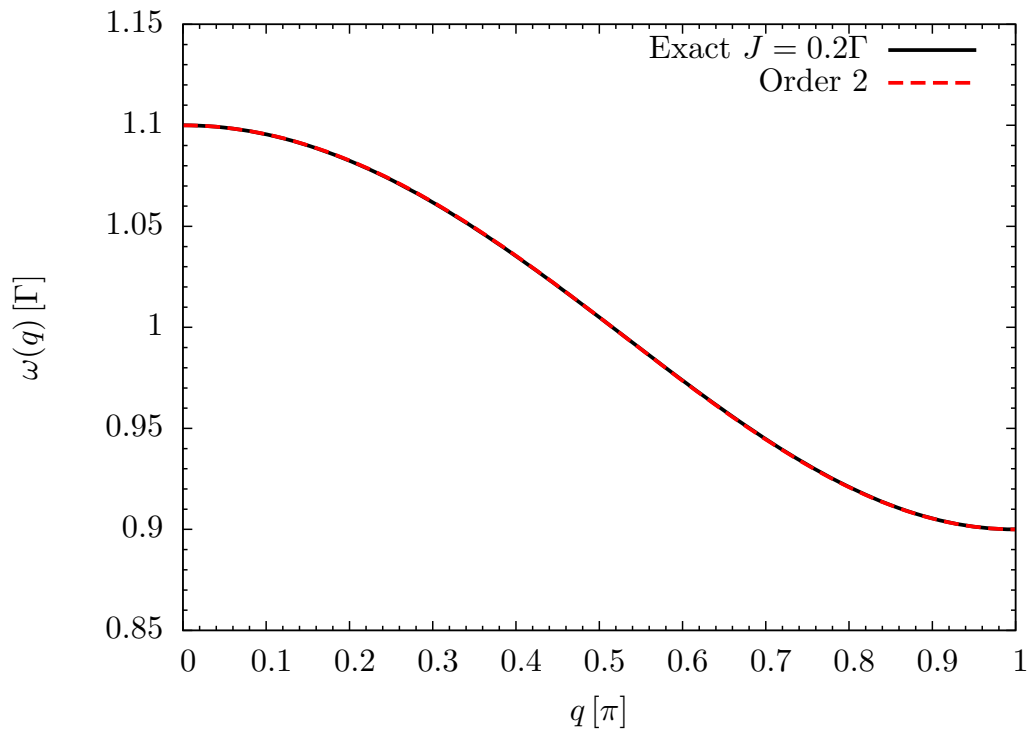


Figure 6.7: Energy dispersion for $J = 0.2\Gamma$. Comparison of the exact result with the CUT calculation.

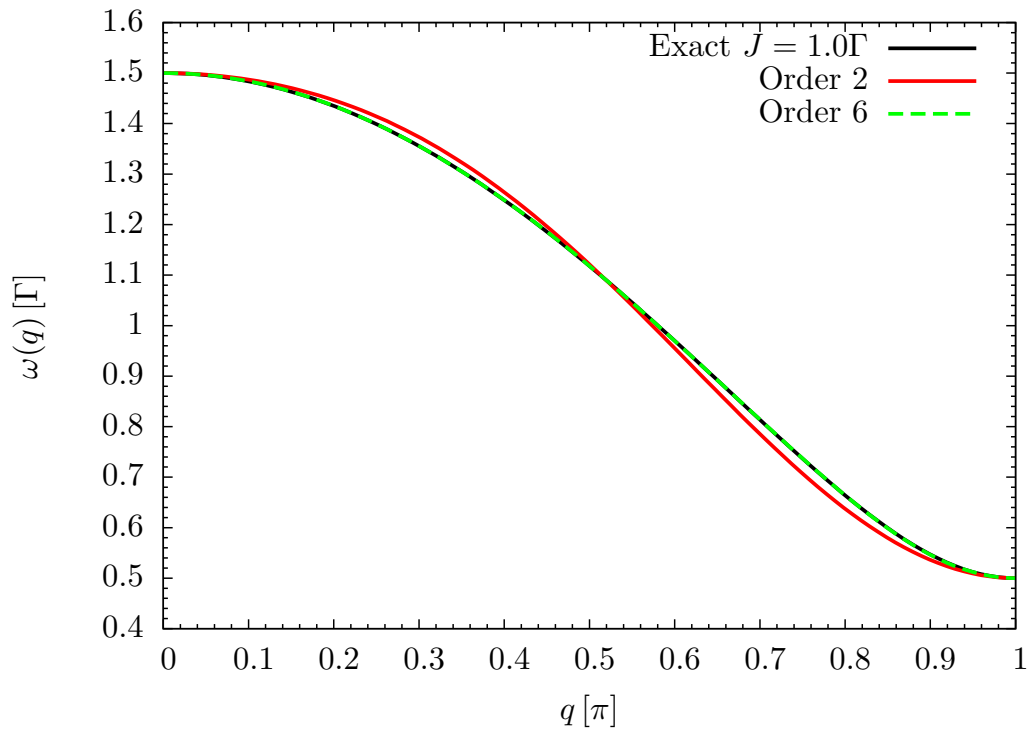


Figure 6.8: Energy dispersion for $J = 1.0\Gamma$. Comparison of the exact result with the CUT calculation.

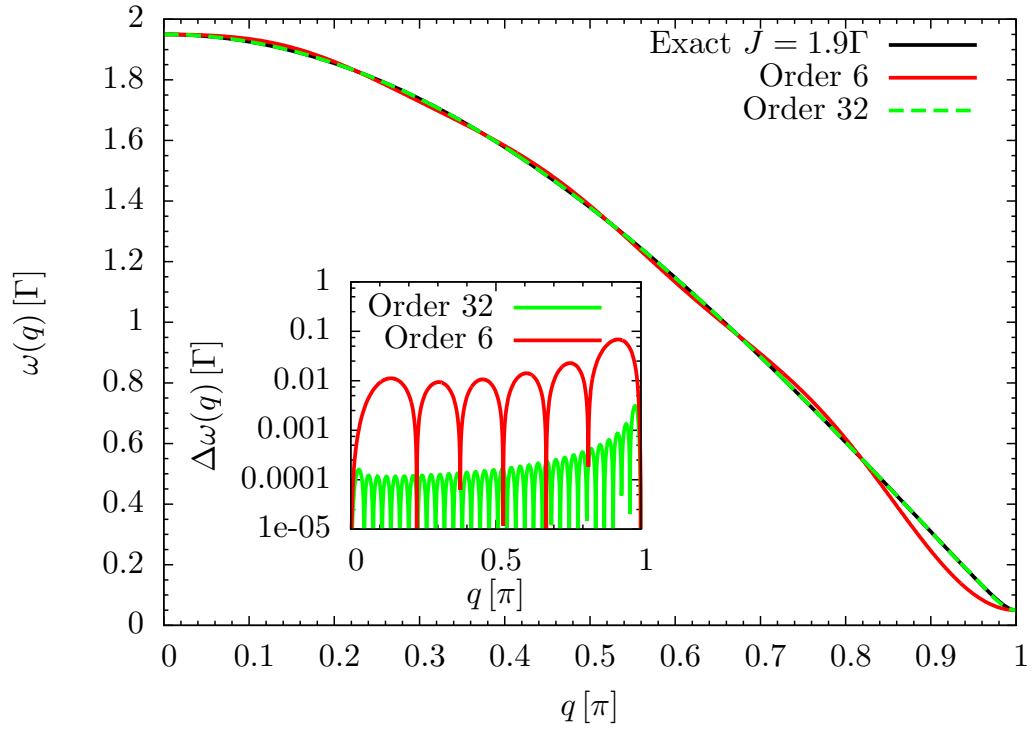


Figure 6.9: Energy dispersion for $J = 1.9\Gamma$. Comparison of the exact result with the CUT calculation. The inset shows the difference between the exact result and the CUT calculation.

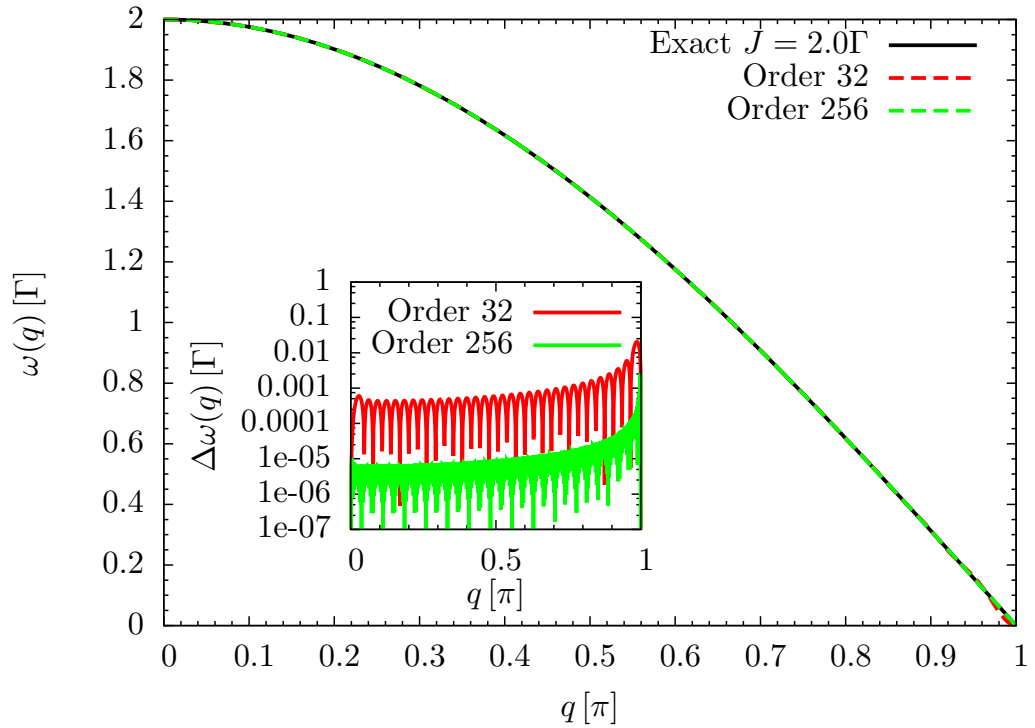


Figure 6.10: Energy dispersion at the QCP $J = 2\Gamma$. Comparison of the exact result with the CUT calculation. The inset shows the difference between the exact result and the CUT calculation.

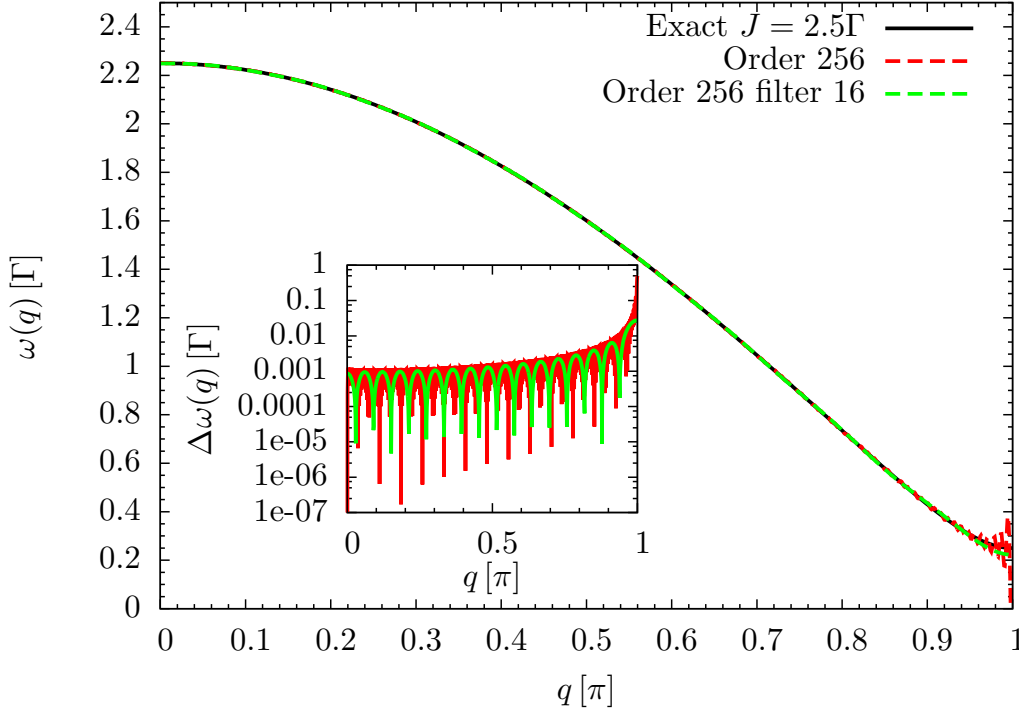


Figure 6.11: Energy dispersion at the QCP $J = 2.5\Gamma$. Comparison of the exact result with the CUT calculation. The second CUT curve was filtered by a low pass so that only the first 16 Fourier-coefficients contribute.

We therefore filtered the first 16 fourier-coefficients of the CUT calculation and compared the resulting curve with the exact one. This improves the result significantly, especially at the critical wave vector. However, this is a purely numerical observation and can not be justified analytically. In particular the Fourier coefficients t_n^{+-} above 16 are not converged, which is shown in Fig. 6.12.

Another interesting quantity that we can obtain using the dispersion is the energy gap Δ of the lowest lying excitations. For all parameters J the gap is located at $q = \pi$ in the Brillouin zone. Using the exact dispersion (6.3.3) yields the following expression for the gap as a function of the parameter J

$$\Delta(J) = \Gamma \left| 1 - \frac{J}{2\Gamma} \right|. \quad (6.3.5)$$

Due to the linearity of this expression, all orders above zero of the CUT yield this graph exactly up to numerical errors $< 10^{-10}$ and up to the QCP. Figure 6.13 shows the exact energy gap in comparison to the CUT calculations. Above the QCP the CUT continues with the linear curve, which is expected in a perturbative truncation scheme in the small Parameter J . The CUT is not able to catch the non differentiable point at $J = 2\Gamma$.

This fact also explains the above deviations of the dispersion for $J > 2\Gamma$. Because the gap is forced to be a linear function, there is a constraint that forces the dispersion at $q = \pi$ to become negative above the QCP.

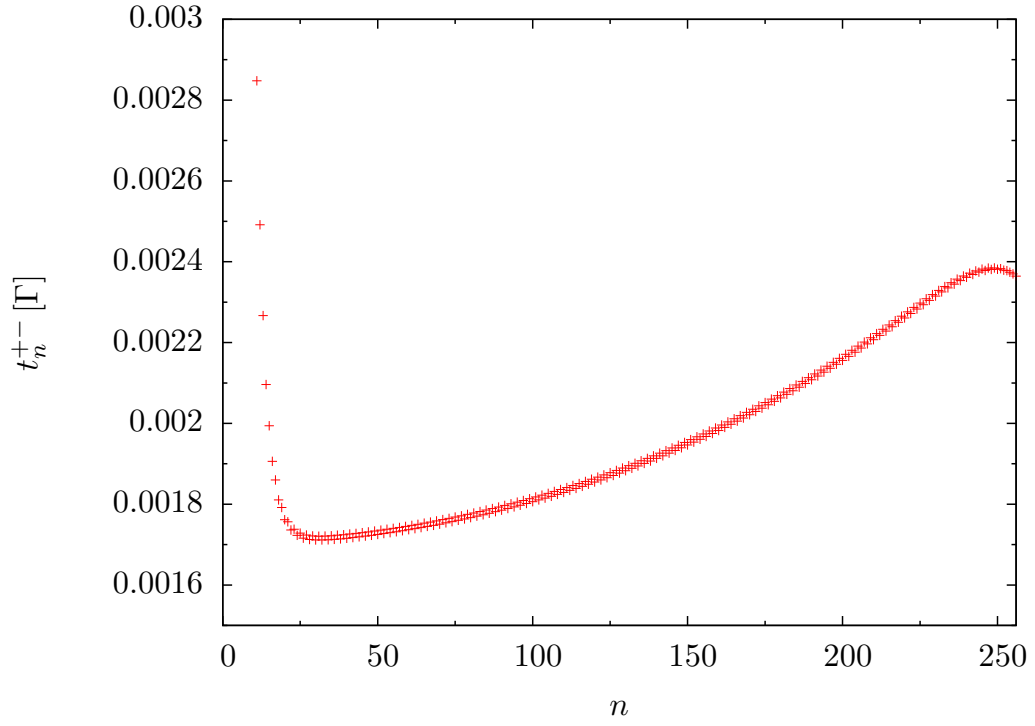


Figure 6.12: Fourier coefficients t_n^{+-} for $J = 2.5\Gamma$ and order 256. At $n \approx 25$ it becomes conspicuous that the Fourier coefficients not yet converged.

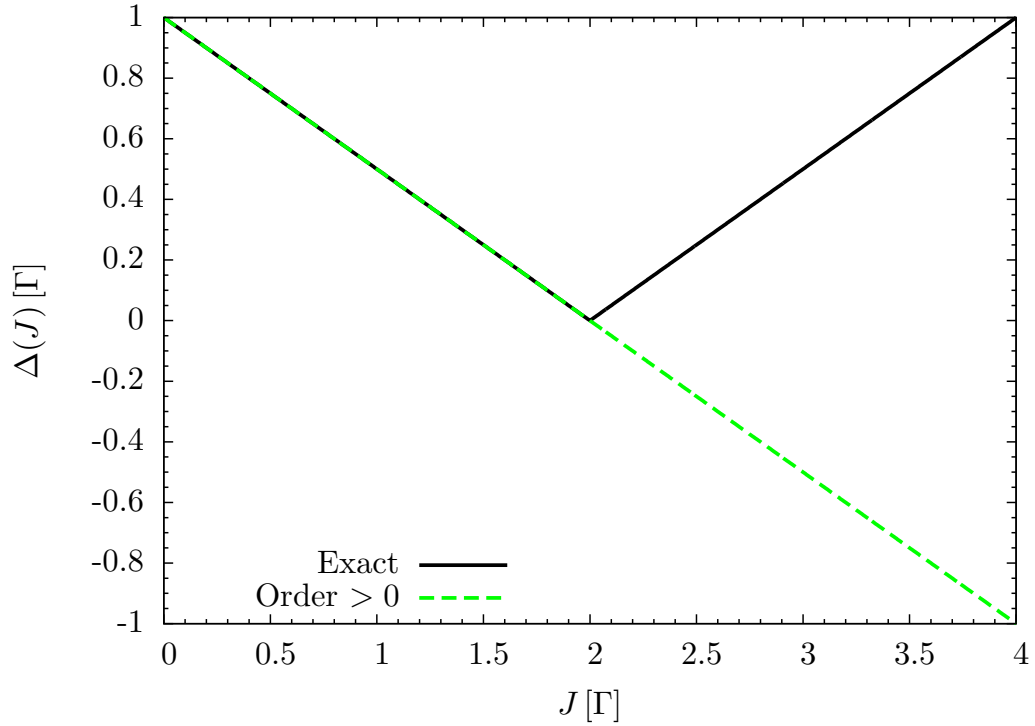


Figure 6.13: Energy gap for different parameters J . Comparison of the exact result with the CUT calculation. All orders > 0 yield the same results within numerical errors.

6.4 Magnetization

6.4.1 Transverse magnetization

Last we examine the transverse magnetization given by the expression,

$$M_z = -\frac{1}{N} \sum_j \langle g | \sigma_j^z | g \rangle = -\frac{1}{N} \langle g | \sum_j \sigma_j^z | g \rangle \quad (6.4.6)$$

Note that 'transverse' refers to the direction of the external field, which is in our model the z-axis.

Here $|g\rangle$ denotes the ground state of the Hamiltonian, which is the zero particle state after the CUT. In the limit $J \rightarrow 0$ all spins are aligned along the external field. As a result,

$$\lim_{J \rightarrow 0} M_z = 1, \quad (6.4.7)$$

holds.

In the case $J > 0$ the spins are disturbed by the antiferromagnetic interaction, reducing the transverse magnetization. An exact expression for this quantity was calculated by Pfeuty in Ref. [31] and is given in Eq. (3.3.17).

To acquire the transverse magnetization in context of the CUT calculation, we transform the observable σ_j^z with the same unitary transformation onto an effective observable. Note, that the corresponding operator can be expressed by a string operator by means of

$$\sum_j \sigma_j^z(l=0) = T_0. \quad (6.4.8)$$

Due to this identity and the fact that the string algebra closes under the commutator, we know that the final effective observable can be written as a linear combination of string operators,

$$\sigma_{\text{eff}}^z = \sum_j \sigma_j^z(l) \Big|_{l=\infty} \quad (6.4.9a)$$

$$= o_0(\infty) T_0 + \sum_n o_n^{+-}(\infty) (T_n^{+-} + \text{h.c.}) + o_n^{++}(\infty) (T_n^{++} + \text{h.c.}). \quad (6.4.9b)$$

Note that all coefficients o_n^{+-} and o_n^{++} do not contribute to the zero particle expectation values. However, they can not be ignored during the flow of the observable.

Finally, the transverse magnetization after the CUT is given by

$$M_z = -\frac{1}{N} \langle 0 | \sigma_{\text{eff}}^z | 0 \rangle = o_0(\infty). \quad (6.4.10)$$

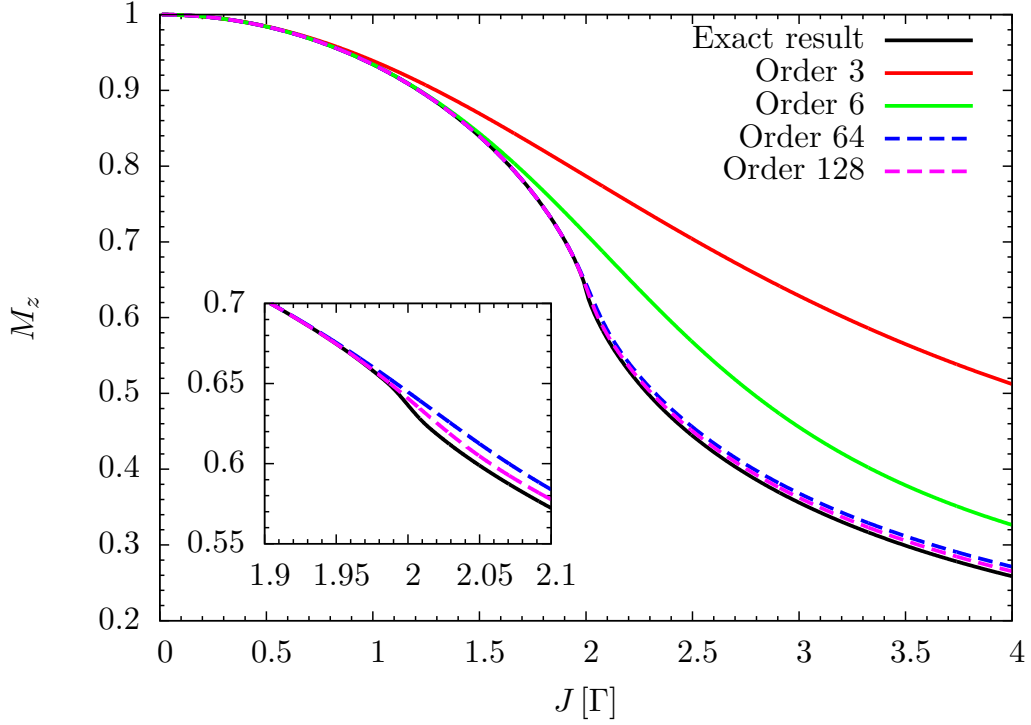


Figure 6.14: Transverse Magnetization as a function of J . Comparison of the exact result with the CUT calculation. The inset shows a close view on the QCP.

Transverse magnetization exponents		
Order	Exponent	Fitting Error
16	15	± 1
32	31	± 1
64	65	± 2
128	129	± 2

Table 6.2: Exponents of the power laws for the transverse magnetization obtained by fitting linear functions.

Due to this simple form of the observable we could again reach very high orders even for the observable transformation. For an order of 128 and $J < 1.8\Gamma$ the results agree up to the numerical precision of 10^{-10} . The transverse magnetization calculated by the CUT is shown in Fig. 6.14 in comparison to the exact result.

As expected the result improves with increasing order. For $J > 2\Gamma$ we again see an agreement for higher orders but with a systematic offset. This can be accounted to the non-analytical point in the magnetization at $J = 2\Gamma$, which can not be described properly by the CUT calculation in its present form.

To analyze the errors more quantitatively, Fig. 6.15 shows the difference between the exact curve and the CUT calculation, similar to Eq. (6.2.1). First, notice that we have taken the logarithm of both, ΔM_z as well as J . Consequently straight lines represent power laws, see also (6.2.2b). By fitting the curves to linear functions we obtain the exponents of the power laws. They are reported in Tab. 6.2. As expected, the exponents are at least above and close to the order of the calculation.

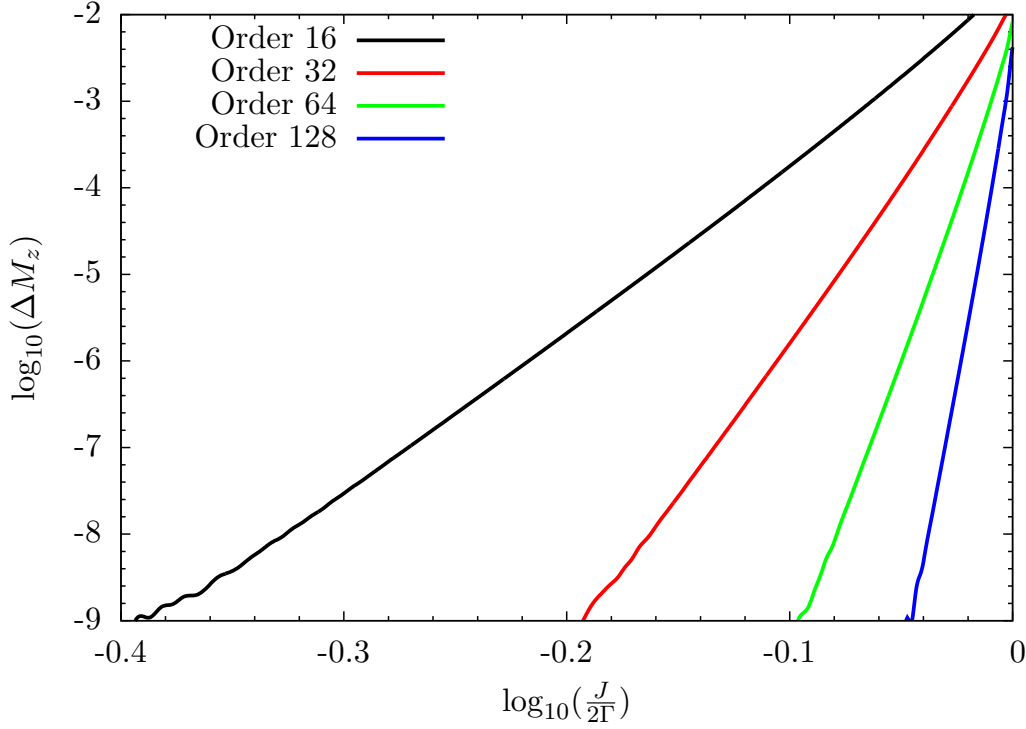


Figure 6.15: Absolute difference between the exact transverse magnetization and the CUT calculation as function of J . The QCP is located at $\log_{10} \left(\frac{J}{2\Gamma} \right) = 0$.

6.4.2 Longitudinal magnetization

Note that the order parameter in the TFIM is given by the longitudinal magnetization,

$$M_x = -\frac{1}{N} \sum_j \langle g | \sigma_j^x | g \rangle. \quad (6.4.11)$$

For $J < 2\Gamma$ the longitudinal magnetization is zero, but it acquires a finite value for $J > 2\Gamma$. Due to the fact that the observable σ_j^x creates or annihilates an odd number of excitations and the generator of the CUT preserves the parity of observables, the longitudinal magnetization will always be zero within the CUT calculation, even above the QCP.

One possibility to avoid this problem is to introduce symmetry breaking terms in the Hamiltonian of the TFIM, such as a longitudinal field $h_x \sigma_x$. However, such terms would not be part of the string algebra and would therefore prevent access to higher order calculations. Therefore, we concentrate on the transverse magnetization. Results, however, for dynamical longitudinal correlations are accessible and will be given in the next chapter.

6.5 Conclusions of the present chapter

In this chapter we investigated the static properties of the TFIM. First we analyzed the convergence of the CUT by evaluating the ROD for various orders and parameter values. In general all RODs decayed exponentially, while the envelope at the QCP showed a power law, as expected for an exact CUT. As a result we could already see the influence of the QCP in the speed of convergence for the CUT.

It was shown that we can obtain the ground state energy per site in a high numerical precision up to the QCP. Even above the QCP the results are still in a qualitative agreement with the exact results, which was accredited to the robustness of the ground state energy.

For the dispersion the results are in good agreement below the QCP. Above the QCP the dispersion was only valid for small values of the wave vector q . Presumably, the reason for this is a constraint to the energy gap that forces the dispersion to become negative at the critical wave vector $q = \pi$. A low pass filter was applied, which could improve the results significantly even at the critical wave vector.

Last, we investigated the transverse magnetization, which was obtained by an observable transformation. For high orders we achieved a good agreement with the exact results up to the QCP. Above the QCP the transverse magnetization obtained a constant error, which was attributed to the non-analytical point at $J = 2\Gamma$.

It is worth emphasizing that all results above the QCP have to be considered carefully, because our local quasi-particle picture breaks down at this point. It is therefore remarkable that many quantities, like the ground state energy, the transverse magnetization and parts of the dispersion, are at least in qualitative agreement with the exact results.

7 Dynamic results

In this chapter we will present and evaluate the dynamic results for the transverse field Ising model. Here, 'dynamic' refers to spectral properties such as the dynamical structure factor (DSF). The DSF is an important quantity because it is directly measurable in scattering experiments. Furthermore, dynamical correlations strongly depend on the model under study and often exhibit features which rely on the microscopic interactions in the Hamiltonian. Examples can include bound states in antiferromagnetic spin ladders [52] or the finite-temperature low-energy 'Villain' modes [53, 54].

In this chapter, we will concentrate on zero temperature dynamics, which is a valid approximation for the experiment as long as $k_b T \ll \Delta$, where Δ is the energy gap of the system under study.

Despite the fact that the TFIM is integrable, the calculation of dynamical correlations remains a difficult and complex problem. For the transverse DSF, exact expressions can be found for example in Ref. [38]. 2006 Hamer et al. proposed an analytic expression for the one-particle longitudinal DSF [19], but to our knowledge there are no results concerning higher quasi-particle spaces.

In the following, we will show our results for the transverse as well as for the longitudinal DSF. For the transverse DSF our results agree very well with the exact expressions, within numerical errors of the order of 10^{-5} . The one-particle longitudinal results coincide with those proposed by Hamer et al. and therefore support their expression. Furthermore, we will show three-particle longitudinal results for the TFIM. Hence we will also investigate the higher particle spaces.

Other methods, such as the tDMRG [55] and exact diagonalization of finite chains, can also yield expressions for the DSF. They are, however, often limited by finite size effects or problems when transforming time dependent data into frequency space. This problem is avoided in the CUT calculation, because the calculation is done directly in the thermodynamic limit and in frequency space.

Additionally, many other methods depend on the Jordan-Wigner-Transformation to map the spin Hamiltonian onto fermions. Therefore, it is not possible to obtain longitudinal correlations within this framework, because they are represented by an extensive string of Fermi operators on the chain.

This problem is also avoided by the CUT, because we stay within the spin picture and do not need extensive operators to describe these correlations.

Nevertheless, one disadvantage of our description is that our effective Hamiltonian is

obtained by numerical integration, so we can not calculate analytical expressions for the DSF.

7.1 Dynamical structure factor

The dynamical structure factor is defined as the Fourier transformation of the correlation function $\langle S_l^\alpha(t) S_{l'}^\beta \rangle$ in time and space,

$$S^{\alpha\beta}(\omega, Q) = \frac{1}{N} \int_{-\infty}^{\infty} \frac{dt}{2\pi} \sum_{l,l'} e^{i\omega t} e^{-iQ(l-l')} \langle S_l^\alpha(t) S_{l'}^\beta \rangle, \quad (7.1.1a)$$

$$\alpha, \beta \in \{x, y, z\}, \quad (7.1.1b)$$

where Q denotes the total momentum. In the following we restrict ourselves to the diagonal part of the DSF, namely $\alpha = \beta$.

The DSF is linked to the imaginary part of the retarded, zero temperature Green function by the fluctuation-dissipation theorem at zero temperature, see for example Ref. [56],

$$S^{\alpha\alpha}(\omega, Q) = -\frac{1}{\pi} \text{Im} G^{\alpha\alpha}(\omega, Q). \quad (7.1.2)$$

In our context, at $T = 0$, it is useful to write this Green function as a resolvent

$$G^{\alpha\alpha}(\omega, Q) = \lim_{\delta \rightarrow 0^+} \langle g | S^\alpha(-Q) \frac{1}{\omega - (H(Q) - E_0) + i\delta} S^\alpha(Q) | g \rangle, \quad (7.1.3a)$$

$$\omega \in \mathbb{R}^+,$$

in which E_0 is the ground state energy and

$$S^\alpha(Q) = \frac{1}{\sqrt{N}} \sum_l e^{iQl} S_l^\alpha \quad (7.1.4)$$

is the Fourier transformed spin operator S_l^α .

When integrating (7.1.1a) over energy we obtain the static or equal time structure factor,

$$S^{\alpha\alpha}(Q) = \frac{1}{N} \sum_{l,l'} e^{-iQ(l-l')} \langle S_l^\alpha S_{l'}^\alpha \rangle. \quad (7.1.5)$$

Integrating again over the wave vector Q yields the total spectral weight, i.e., the sum rule

$$S^{\alpha\alpha} = \frac{1}{N} \sum_l \langle S_l^\alpha S_l^\alpha \rangle = (S^\alpha)^2 = \frac{1}{4}. \quad (7.1.6)$$

The sum rule allows us to evaluate how much weight is concentrated in certain quasi-particle spaces [57].

Now we introduce the CUT framework, see also Ref. [52, 58], by inserting several identities $UU^\dagger = 1$ into Eq. (7.1.3a),

$$G^{\alpha\alpha}(\omega, Q) = \lim_{\delta \rightarrow 0+} \langle g | UU^\dagger S^\alpha(-Q) UU^\dagger \frac{1}{\omega - (H(Q) - E_0) + i\delta} UU^\dagger S^\alpha(Q) UU^\dagger | g \rangle, \quad (7.1.7)$$

where U denotes the continuous unitary transformation at $l = \infty$

$$U = U_{\text{CUT}}|_{l=\infty}. \quad (7.1.8)$$

Applying these unitary transformation to the states and operators yields

$$U^\dagger |g\rangle = |0\rangle, \quad (7.1.9a)$$

$$U^\dagger S^\alpha(Q) U = S_{\text{eff}}^\alpha(Q), \quad (7.1.9b)$$

$$U^\dagger \frac{1}{\omega - (H(Q) - E_0) + i\delta} U = \frac{1}{\omega - (H_{\text{eff}}(Q) - E_0) + i\delta}. \quad (7.1.9c)$$

Note that the new ground state is given by the quasi-particle vacuum $|0\rangle$, because our effective Hamiltonian is quasi-particle conserving and the pc generator sorts the quasi-particle spaces according to energy. Furthermore we expect that the ground state does not break particle conservation. Combining these expression with Eq. (7.1.7) and (7.1.2) yields

$$S^{\alpha\alpha}(\omega, Q) = -\frac{1}{\pi} \text{Im} \lim_{\delta \rightarrow 0+} \langle 0 | S_{\text{eff}}^\alpha(-Q) \frac{1}{\omega - (H_{\text{eff}}(Q) - E_0) + i\delta} S_{\text{eff}}^\alpha(Q) | 0 \rangle, \quad (7.1.10)$$

which depends only on our effective Hamiltonian and effective observable obtained by the CUT.

7.2 Splitting different quasi-particle spaces

In this section we specialize our consideration above to the string operator basis, see Eq. (5.1.7). To calculate $S^{\alpha\alpha}(\omega, Q)$ in our effective model, we need to Fourier transform the effective observables S_{eff}^α . We therefore split the effective observable into terms according to the number of particle creators σ^+ and particle annihilators σ^- they contain.

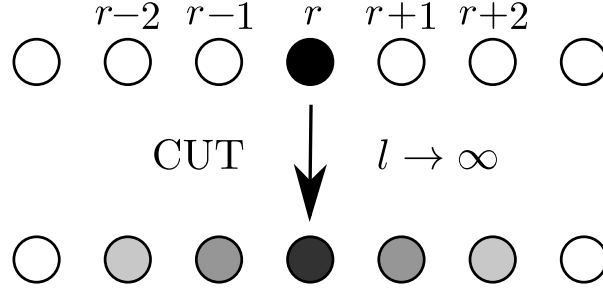


Figure 7.1: Graphical illustration of the local observable transformation by the CUT. The initial observable is located at site r . Due to the CUT new terms appear in the effective observable, which also act on neighboring sites. In this model the maximum range of the effective observable is given by the order of the calculation, but most of the weight will be located near the site r if we are not to close the QCP.

The notation

$$S_{\text{eff}}^{\alpha} = \sum_{c=0, a=0}^{\infty} S_{\text{eff}}|_a^c \quad (7.2.11)$$

introduces the operators $S_{\text{eff}}|_a^c$, which create c particles and annihilate a particles. First note that every operator with $a \neq 0$ simply yields

$$S_{\text{eff}}|_{a \neq 0}^c |0\rangle = 0 \quad (7.2.12)$$

if it acts on the quasi-particle vacuum. Therefore, we can ignore these operators in the case $T = 0$, because they do not contribute to the DSF.

Next we examine how the Fourier transformed effective observable acts on the quasi-particle vacuum. First, note that according to Eq. (7.1.1a) we need a local effective observable in order to define the Fourier transformed observables. Due to the CUT this local observables acquires a finite extension, depending on the observable, the parameter J and the order of calculation. This is depicted in Fig. 7.1. Investigating the action of the effective observable on the zero-particle state $|0\rangle$ yields

$$\begin{aligned} S_{\text{eff}}^{\alpha}(Q) |0\rangle &= \frac{1}{\sqrt{N}} \sum_r e^{iQr} \sum_{c=0} S_{\text{eff}}|_0^c |0\rangle \\ &= \frac{1}{\sqrt{N}} \sum_{r,j} e^{iQr} s_{\text{eff},j} |0\rangle \\ &\quad + \frac{1}{\sqrt{N}} \sum_{r,d_0,j} e^{iQr} s_{\text{eff},j}^{d_0} |r + d_0\rangle \\ &\quad + \frac{1}{\sqrt{N}} \sum_{r,d_0,d_1,j} e^{iQr} s_{\text{eff},j}^{d_0,d_1} |r + d_0, r + d_0 + d_1\rangle \\ &\quad + \frac{1}{\sqrt{N}} \sum_{r,d_0,d_1,d_2,j} e^{iQr} s_{\text{eff},j}^{d_0,d_1,d_2} |r + d_0, r + d_0 + d_1, r + d_0 + d_1 + d_2\rangle \\ &\quad + \dots \end{aligned} \quad (7.2.13)$$

where we have introduced several new notations. First $|r + d_0\rangle$, $d_0 \in \mathbb{Z}$ denotes a single excited state at site $r + d_0$, see also Eq. (5.1.10). Analogously, $|r + d_0, r + d_0 + d_1\rangle$ is a state with two excitations at sites $r + d_0$ and $r + d_0 + d_1$ and so on. Note that $d_1, d_2, \dots > 0$ due to the hardcore constraint and the indistinguishability of the particles. The effect of the operator $S_{\text{eff}}|_0^c$ is split into the different sites it creates excitations. The values $s_{\text{eff},j}, s_{\text{eff},j}^{d_0}, s_{\text{eff},j}^{d_0,d_1}, \dots$ are the different prefactors of the operators. Note that in contrast to the multi-particle-representation we need an additional index j because it is possible to obtain two operators that create excitations on the same site without being the same operator. For example take the two operators S_r^+ and $S_r^+ S_{r+1}^z$. They both create an excitation on site r , but the latter one might change the sign of the energy, depending on the state of the neighbouring site. Thus, the index j is a multi-index to distinguish all of these operators.

Because the effective Hamiltonian in Eq. (7.1.10) is particle conserving, we can now split the DSF according to particle number,

$$S^{\alpha\alpha}(\omega, Q) = S_0^{\alpha\alpha}(\omega, Q) + S_1^{\alpha\alpha}(\omega, Q) + S_2^{\alpha\alpha}(\omega, Q) + \dots, \quad (7.2.14)$$

where $S_0^{\alpha\alpha}(\omega, Q) = S_0^{\alpha\alpha}$ denotes the on site correlation, like M_z^2 for $\alpha = z$.

7.2.1 One-particle case

For the one-particle structure factor, the state

$$S_{\text{eff}}|_0^1(Q) |0\rangle = \frac{1}{\sqrt{N}} \sum_{r,d_0,j} e^{iQr} s_{\text{eff},j}^{d_0} |r + d_0\rangle \quad (7.2.15)$$

must be considered. Shifting the r sum by d_0 results in the expression

$$S_{\text{eff}}|_0^1(Q) |0\rangle = \frac{1}{\sqrt{N}} \sum_{r,d_0,j} e^{-iQd_0} e^{iQ(r+d_0)} s_{\text{eff},j}^{d_0} |r + d_0\rangle \quad (7.2.16a)$$

$$= \sum_{d_0,j} \underbrace{s_{\text{eff},j}^{d_0} e^{-iQd_0}}_{:=s_{\text{eff},j}^{d_0}(Q)} |Q\rangle \quad (7.2.16b)$$

$$= \sum_{d_0,j} s_{\text{eff},j}^{d_0}(Q) |Q\rangle \quad (7.2.16c)$$

which is in fact a one-particle state with momentum Q . From now on we refer to this one-dimensional Hilbert space as \mathbb{H}_Q^1 , which stands for the one-particle excitations with total momentum Q . In this case the evaluation of the resolvent in Eq. (7.1.10) is

analytically possible,

$$S_1^{\alpha\alpha}(\omega, Q) = -\frac{1}{\pi} \text{Im} \lim_{\delta \rightarrow 0+} \langle Q | \left(\sum_{d_0, j} s_{\text{eff}, j}^{d_0}(Q) \right)^* \frac{1}{\omega - (H(Q) - E_0) + i\delta} \left(\sum_{d_0, j} s_{\text{eff}, j}^{d_0}(Q) \right) | Q \rangle \quad (7.2.17a)$$

$$= - \left| \sum_{d_0, j} s_{\text{eff}, j}^{d_0}(Q) \right|^2 \frac{1}{\pi} \text{Im} \lim_{\delta \rightarrow 0+} \frac{1}{\omega - \omega(Q) + i\delta}, \quad (7.2.17b)$$

$$= - \left| \sum_{d_0, j} s_{\text{eff}, j}^{d_0}(Q) \right|^2 \frac{1}{\pi} \text{Im} \left(\mathcal{P} \frac{1}{\omega - \omega(Q)} - i\pi \delta(\omega - \omega(Q)) \right), \quad (7.2.17c)$$

$$= \left| \sum_{d_0, j} s_{\text{eff}, j}^{d_0}(Q) \right|^2 \delta(\omega - \omega(Q)), \quad (7.2.17d)$$

which is just the one-particle static structure factor multiplied with a delta function in energy space. Note that we have used Dirac's identity,

$$\lim_{\delta \rightarrow 0+} \frac{1}{\omega - \omega_0 + i\delta} = \mathcal{P} \frac{1}{\omega - \omega_0} - i\pi \delta(\omega - \omega_0), \quad (7.2.18)$$

in Eq. (7.2.17c).

7.2.2 Two-particle case

For the two-particle structure factor the state

$$S_{\text{eff}}|_0^2(Q) |0\rangle = \frac{1}{\sqrt{N}} \sum_{r, d_0, d_1, j} e^{iQr} s_{\text{eff}, j}^{d_0, d_1} |r + d_0, r + d_0 + d_1\rangle \quad (7.2.19)$$

must be considered. Shifting the exponent by $d_0 + d_1/2$, the center of mass, results in the expression

$$S_{\text{eff}}|_0^2(Q) |0\rangle = \sum_{d_0, d_1, j} e^{-iQ(d_0 + d_1/2)} s_{\text{eff}, j}^{d_0, d_1} \underbrace{\frac{1}{\sqrt{N}} \sum_r e^{iQ(r + d_0 + d_1/2)} |r + d_0, r + d_0 + d_1\rangle}_{:=|Q, d_1\rangle} \quad (7.2.20a)$$

$$= \sum_{d_0, d_1, j} \underbrace{e^{-iQ(d_0 + d_1/2)} s_{\text{eff}, j}^{d_0, d_1}}_{:=s_{\text{eff}, j}^{d_0, d_1}(Q)} |Q, d_1\rangle \quad (7.2.20b)$$

$$= \sum_{d_0, d_1, j} s_{\text{eff}, j}^{d_0, d_1}(Q) |Q, d_1\rangle \quad (7.2.20c)$$

where we have introduced $|Q, d_1\rangle$ which is the Fourier transformation of a two-particle state with distance d_1 . From now on we refer to this Hilbert space as \mathbb{H}_Q^2 , which stands for the two-particle excitations with total momentum Q . Note that the action of H_{eff} is

trivial in the zero and one-particle case. But it must be carefully analyzed in the multi-particle case due to the hardcore constraint. We emphasize the structure of the effective Hamiltonian in Eq. (5.4.49). Hence we analyze the action of the operators T_0, T_n^{+-}, T_n^{-+} separately. Starting with the simple operator T_0 yields

$$t_0(\infty)T_0|Q, d_1\rangle = t_0(\infty)T_0\frac{1}{\sqrt{N}}\sum_r e^{iQ(r+d_0+d_1/2)}|r+d_0, r+d_0+d_1\rangle \quad (7.2.21a)$$

$$= t_0(\infty)(-N+4)\frac{1}{\sqrt{N}}\sum_r e^{iQ(r+d_0+d_1/2)}|r+d_0, r+d_0+d_1\rangle \quad (7.2.21b)$$

$$= (E_0 + 4t_0(\infty))|Q, d_1\rangle. \quad (7.2.21c)$$

Note that we subtract the ground state energy in Eq. (7.1.10) which can therefore be left out in the action of H_{eff} . Next we analyze the action of the operator T_n^{+-} ,

$$\begin{aligned} \sum_n t_n^{+-}(\infty)T_n^{+-}|Q, d_1\rangle &= \sum_n (-1)^{n-1}t_n^{+-}(\infty)e^{iQn/2}|Q, d_1+n\rangle \\ &+ \sum_{n<d_1} (-1)^{n-1}t_n^{+-}(\infty)e^{iQn/2}|Q, d_1-n\rangle \\ &+ \sum_{n>d_1} (-1)^nt_n^{+-}(\infty)e^{iQn/2}|Q, n-d_1\rangle, \end{aligned} \quad (7.2.22)$$

and of the operator T_n^{-+} ,

$$\begin{aligned} \sum_n t_n^{+-}(\infty)T_n^{-+}|Q, d_1\rangle &= \sum_n (-1)^{n-1}t_n^{+-}(\infty)e^{-iQn/2}|Q, d_1+n\rangle \\ &+ \sum_{n<d_1} (-1)^{n-1}t_n^{+-}(\infty)e^{-iQn/2}|Q, d_1-n\rangle \\ &+ \sum_{n>d_1} (-1)^nt_n^{+-}(\infty)e^{-iQn/2}|Q, n-d_1\rangle. \end{aligned} \quad (7.2.23)$$

Note the different signs of the second and third term due to string operator property. The remaining task of evaluating the resolvent in Eq. (7.1.10) will be considered in section 7.3.

7.2.3 Three-particle case

For the three-particle structure factor the state

$$S_{\text{eff}}|_0^3(Q)|0\rangle = \frac{1}{\sqrt{N}}\sum_{r,d_0,d_1,d_2,j} e^{iQr}S_{\text{eff},j}^{d_0,d_1,d_2}|r+d_0, r+d_0+d_1, r+d_0+d_1+d_2\rangle \quad (7.2.24)$$

must be considered. Shifting the exponent by $d_0 + 2d_1/3 + d_2/3$ results in the expression

$$S_{\text{eff}}|_0^3(Q) |0\rangle = \sum_{d_0, d_1, d_2, j} e^{-iQ(d_0 + 2d_1/3 + d_2/3)} s_{\text{eff}, j}^{d_0, d_1, d_2} \quad (7.2.25a)$$

$$\cdot \underbrace{\frac{1}{\sqrt{N}} \sum_r e^{iQ(r + d_0 + 2d_1/3 + d_2/3)} |r + d_0, r + d_0 + d_1, r + d_0 + d_1 + d_2\rangle}_{:=|Q, d_1, d_2\rangle} \quad (7.2.25b)$$

$$= \sum_{d_0, d_1, d_2, j} e^{-iQ(d_0 + 2d_1/3 + d_2/3)} s_{\text{eff}, j}^{d_0, d_1, d_2} |Q, d_1, d_2\rangle \quad (7.2.25c)$$

$:= s_{\text{eff}, j}^{d_0, d_1, d_2}(Q)$

$$= \sum_{d_0, d_1, d_2, j} s_{\text{eff}, j}^{d_0, d_1, d_2}(Q) |Q, d_1, d_2\rangle \quad (7.2.25d)$$

where we have introduced $|Q, d_1, d_2\rangle$, which is the Fourier transformation of a three-particle state with distance d_1 between the first two particles and distance d_2 between the second two particles. From now on we refer to this Hilbert space as \mathbb{H}_Q^3 , which stands for the three-particle excitations with total momentum Q . Similary to the two-particle state we examine the action of the effective Hamiltonian on the three-particle state. The simple operator T_0 yields

$$t_0(\infty)T_0 |Q, d_1, d_2\rangle = t_0(\infty)(-N + 6) |Q, d_1, d_2\rangle \quad (7.2.26a)$$

$$= (E_0 + 6t_0(\infty)) |Q, d_1, d_2\rangle. \quad (7.2.26b)$$

Next we analyze the action of the operator T_n^{+-} ,

$$\begin{aligned} \sum_n t_n^{+-}(\infty)T_n^{+-} |Q, d_1, d_2\rangle &= \sum_n (-1)^{n-1} t_n^{+-}(\infty) e^{iQn/3} |Q, d_1 + n, d_2\rangle \\ &+ \sum_{n < d_1} (-1)^{n-1} t_n^{+-}(\infty) e^{iQn/3} |Q, d_1 - n, d_2 + n\rangle \\ &+ \sum_{n > d_1} (-1)^n t_n^{+-}(\infty) e^{iQn/3} |Q, n - d_1, d_2 + d_1\rangle \quad (7.2.27) \\ &+ \sum_{n < d_2} (-1)^{n-1} t_n^{+-}(\infty) e^{iQn/3} |Q, d_1, d_2 - n\rangle \\ &+ \sum_{d_1 + d_2 > n > d_2} (-1)^n t_n^{+-}(\infty) e^{iQn/3} |Q, d_1 + d_2 - n, n - d_2\rangle \\ &+ \sum_{n > d_1 + d_2} (-1)^{n-1} t_n^{+-}(\infty) e^{iQn/3} |Q, n - d_1 - d_2, d_1\rangle, \end{aligned}$$

and of the operator T_n^{-+} ,

$$\begin{aligned}
\sum_n t_n^{+-}(\infty) T_n^{-+} |Q, d_1, d_2\rangle &= \sum_n (-1)^{n-1} t_n^{+-}(\infty) e^{-iQn/3} |Q, d_1, d_2 + n\rangle \\
&+ \sum_{n < d_2} (-1)^{n-1} t_n^{+-}(\infty) e^{-iQn/3} |Q, d_1 + n, d_2 - n\rangle \\
&+ \sum_{n > d_2} (-1)^n t_n^{+-}(\infty) e^{-iQn/3} |Q, d_1 + d_2, n - d_2\rangle \quad (7.2.28) \\
&+ \sum_{n < d_1} (-1)^{n-1} t_n^{+-}(\infty) e^{-iQn/3} |Q, d_1 - n, d_2\rangle \\
&+ \sum_{d_1 + d_2 > n > d_1} (-1)^n t_n^{+-}(\infty) e^{-iQn/3} |Q, n - d_1, d_1 + d_2 - n\rangle \\
&+ \sum_{n > d_1 + d_2} (-1)^{n-1} t_n^{+-}(\infty) e^{-iQn/3} |Q, d_2, n - d_1 - d_2\rangle.
\end{aligned}$$

The remaining task of evaluating the resolvent in Eq. (7.1.10) will be considered in section 7.3.

7.3 Lanczos algorithm and continued fraction representation

As we have already seen in Eq. (7.2.14) the DSF can be divided into different quasi-particle subspaces. Furthermore we have shown that,

$$H_{\text{eff}} : \mathbb{H}_Q^c \rightarrow \mathbb{H}_Q^c, \quad c \in \mathbb{N}^+. \quad (7.3.29)$$

holds for the effective Hamiltonian.

We use this property to evaluate the resolvent in Eq. (7.1.10) by means of a Lanczos tridiagonalization and a continued fraction representation of the resolvent, see Ref. [59, 60]. The basic idea is to transform the effective Hamiltonian into a basis, in which its action on the states in \mathbb{H}_Q^c is given by a tridiagonal matrix. Then the resolvent can be expressed as a continued fraction of the kind

$$\langle 0 | S_{\text{eff}}^\alpha |_0^c(-Q) \frac{1}{\omega - (H_{\text{eff}}(Q) - E_0)} S_{\text{eff}}^\alpha |_0^c(Q) | 0 \rangle = \frac{b_0^2}{\omega - a_0 - \frac{b_1^2}{\omega - a_1 - \frac{b_2^2}{\ddots}}}, \quad (7.3.30)$$

where the coefficients a_n and b_n are the matrix elements of the tridiagonal matrix representation of the effective Hamiltonian

$$H_{\text{eff}}|_{Q,\text{tri}}^c - E_0 = \begin{pmatrix} a_0 & b_1 & 0 & 0 & \dots \\ b_1 & a_1 & b_2 & 0 & \dots \\ 0 & b_2 & a_2 & \ddots & \\ 0 & 0 & \ddots & \ddots & \\ \vdots & \vdots & & & \end{pmatrix}. \quad (7.3.31)$$

Here, the matrix itself depends on the momentum Q and the quasi-particle space c . To obtain these matrix elements we use the Lanczos tridiagonalization, see Ref. [59, 60].

It is worth emphasizing that we only need to know the action of the effective Hamiltonian on a state $\vec{v} \in \mathbb{H}_Q^c$ in order to obtain the required continued fraction coefficients a_n and b_n . This action was already calculated in the previous two sections and can now be used for the Lanczos tridiagonalization. For a more detailed discussion of the Lanczos algorithm, see Ref. [61].

The pattern to obtain the continued fraction coefficients reads

$$\vec{v}_0 = S_{\text{eff}}|_0^c(Q) |0\rangle \quad (7.3.32a)$$

$$b_n = |v_n| \quad (7.3.32b)$$

$$\vec{u}_n = \frac{\vec{v}_n}{b_n} \quad (7.3.32c)$$

$$a_n = \vec{u}_n^T H_{\text{eff}} \vec{u}_n \quad (7.3.32d)$$

$$\vec{v}_{n+1} = \begin{cases} H_{\text{eff}} \vec{u}_n - a_n \vec{u}_n - b_n \vec{u}_{n-1} & \text{if } n > 0 \\ H_{\text{eff}} \vec{u}_0 - a_0 \vec{u}_0 & \text{if } n = 0 \end{cases} \quad (7.3.32e)$$

with $n \in \mathbb{N}_0$. As we can see, the algorithm consists of the multiple application of the Hamiltonian H_{eff} on the start vector \vec{v}_0 and a Gram-Schmidt orthogonalization. Note that the starting vectors were already calculated in the previous sections.

7.3.1 Errors

In the following sections we investigate one-, two- and three-particle spectral densities. The one-particle case can be treated fairly simply as we have seen before. For the two- and three-particle cases, however, we need to employ the Lanczos algorithm, which induces additional numerical errors. On the one hand, it is impossible to achieve an infinite depth in the continued fraction in Eq. (7.3.30). We deal with this problem by the use of appropriate terminators [52, 59, 60].

On the other hand, the Hilbert spaces \mathbb{H}_Q^c $c > 1$ are of infinite dimension and the action of the effective Hamiltonian must be truncated to a suitable subspace. This is done by

introducing a maximum range between the multi-particle excitations. This means that the relative distances d_1 , in the case \mathbb{H}_Q^2 , and d_1, d_2 , in the case \mathbb{H}_Q^3 , will be restricted to a maximum range d_{\max} ,

$$|Q, d_1\rangle \rightarrow d_1 < d_{\max} \quad (7.3.33a)$$

$$|Q, d_1, d_2\rangle \rightarrow d_1, d_2 < d_{\max}. \quad (7.3.33b)$$

To obtain a negligible computation time, the maximum range in the two-particle case will be around 4000, while we restrict ourselves to a maximum of 200 in the three-particle case.

The error introduced by this truncation becomes significant once the correlation length times the maximum number of considered continued fraction coefficients is greater than these values. Otherwise we would truncate a large amount of the physics we want to describe. It is therefore negligible if we restrict ourselves to parameters $J < 1.9\Gamma$.

A more quantitative analysis of this fact will be considered in the following sections.

7.3.2 Termination

The result of the tridiagonalization is a finite set of continued fraction coefficients a_n and b_n . Considering the form of the DSF in Eq. (7.1.10) and the continued fraction (7.3.30), we still have to take the imaginary part of the limit $\delta \rightarrow 0+$. For any finite continued fraction this results in the sum of δ -functions. This is correct for any finite size system, but in the thermodynamic limit we expect the spectral density to be a continuous function of ω and Q with δ -functions only located at discrete states such as bound states.

The position of the upper and lower edge of multi-particle continua is determined by the single particle dispersion through

$$\omega_{\max}^c = \max_{q_1+q_2+\dots+q_c=Q} \sum_{i=1}^c \omega(q_i) \quad (7.3.34a)$$

$$\omega_{\min}^c = \min_{q_1+q_2+\dots+q_c=Q} \sum_{i=1}^c \omega(q_i), \quad (7.3.34b)$$

in which the max/min is obtained under the constraint of total momentum conservation. For a connected continuum it can be shown that the corresponding continued fraction coefficients approach limits which are directly connected to the position of the upper and lower edge of the continuum [52, 59, 60],

$$a_{\infty} = \frac{\omega_{\max}^c + \omega_{\min}^c}{2} \quad (7.3.35a)$$

$$b_{\infty} = \frac{\omega_{\max}^c - \omega_{\min}^c}{4}. \quad (7.3.35b)$$

One way to achieve a finite broadening is to take $i\delta$ as a finite value. Then all delta functions will become Lorentzians. This can be applied when trying to simulate finite resolution effects in experiments. An example is depicted in Fig. 7.2.

Another way is to use a suitable function to terminate the continued fraction and to obtain a continuous spectral density. The easiest way to explain this is the following example: Let

$$a_n = a \quad \forall n \quad (7.3.36a)$$

$$b_n = b \quad \forall n \quad (7.3.36b)$$

then the Green function can be written as

$$G(\omega) = \lim_{\delta \rightarrow 0+} \frac{b^2}{\omega + i\delta - a - \frac{b^2}{\omega + i\delta - a - \frac{b^2}{\ddots}}} = \frac{b^2}{\omega - a - \tau(\omega)}, \quad (7.3.37)$$

where $\tau(\omega)$ denotes our terminator. Due to the self-similarity of the terminator and the Green function in Eq. (7.3.37) we can deduct

$$\Rightarrow \tau(\omega) = G(\omega) \quad (7.3.38)$$

for this special case. Then,

$$\tau^2(\omega) + (a - \omega)\tau(\omega) + b^2 = 0 \quad (7.3.39)$$

holds. In this case we can calculate the corresponding spectral density exactly by

$$\Rightarrow S^{\alpha\alpha}(\omega) = -\frac{1}{\pi} \text{Im} G(\omega) \quad (7.3.40a)$$

$$= -\frac{1}{\pi} \text{Im} \frac{1}{2} \underbrace{\left(\omega - a - i\sqrt{4b^2 - (\omega - a)^2} \right)}_{\tau(\omega)} \quad (7.3.40b)$$

This simple example shows the main advantage of terminators in comparison to truncation of the finite continued fraction, see Fig. 7.2. For our simple example spectral density the calculation with a terminator even obtains the exact spectral density. In practice the condition (7.3.36a) and (7.3.36b) does not hold exactly, however once the continued fraction coefficients have converged close enough to the limits a_∞ and b_∞ , we can insert the square root terminator (7.3.40b) to obtain a smooth continuous function of ω . Furthermore it is possible to check the level of convergence, because we can obtain the limits a_∞ and b_∞ from the one-particle dispersion analytically.

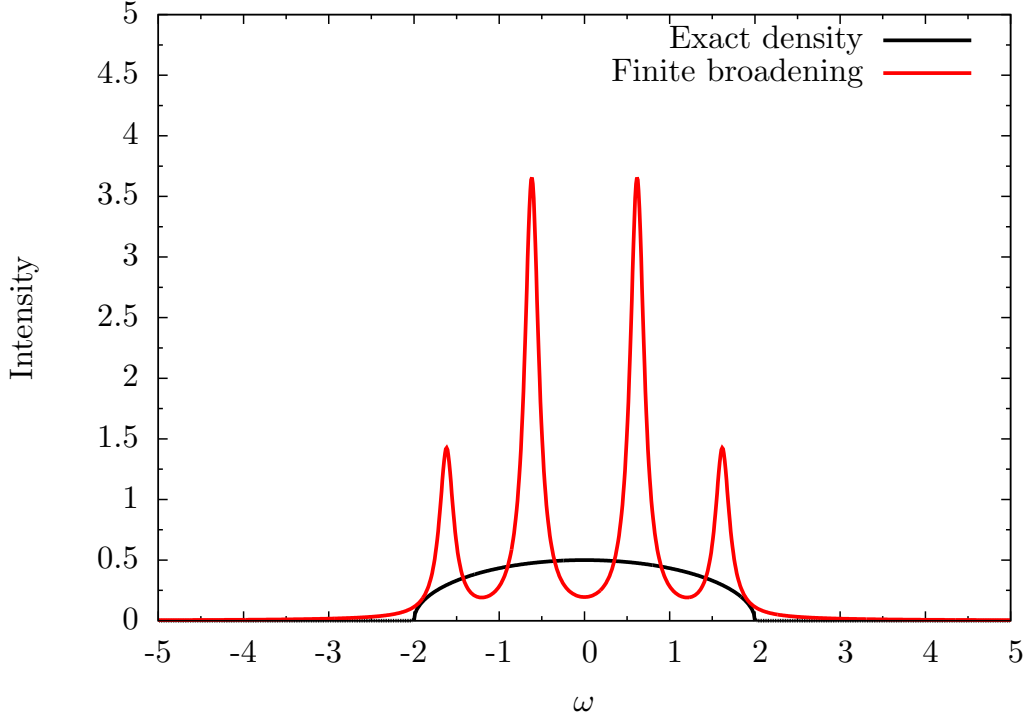


Figure 7.2: Graphical illustration of the finite broadening effect. The exact spectral density is shown as the black curve. This is also the curve obtained by the use of the square root terminator. The parameters of the exact density are $a = 0$ and $b = 1$. The red curve is the finite continued fraction of depth four with a finite broadening of $\delta = 0.1$.

7.3.3 Band edge singularities

Another piece of information that can be obtained from the sequence a_n and b_n are the exponents of the band edge singularities, see also Fig. 7.3. They are directly connected to the asymptotically terms in $a_n \rightarrow a_\infty$ and $b_n \rightarrow b_\infty$. A more detailed analysis reveals that

$$a_n = a_\infty + b_\infty \frac{\beta^2 - \alpha^2}{2n^2} + \mathcal{O}\left(\frac{1}{n^3}\right) \quad (7.3.41a)$$

$$b_n = b_\infty + b_\infty \frac{1 - 2\alpha^2 - 2\beta^2}{8n^2} + \mathcal{O}\left(\frac{1}{n^3}\right), \quad (7.3.41b)$$

holds for algebraic singularities at the band edges, see Ref. [59]. This relation allows us to obtain the band edge singularities up to the signs by fitting a function of the kind

$$f(x) = C + \frac{D}{x^2} \quad (7.3.42)$$

to the obtained continued fraction coefficients.

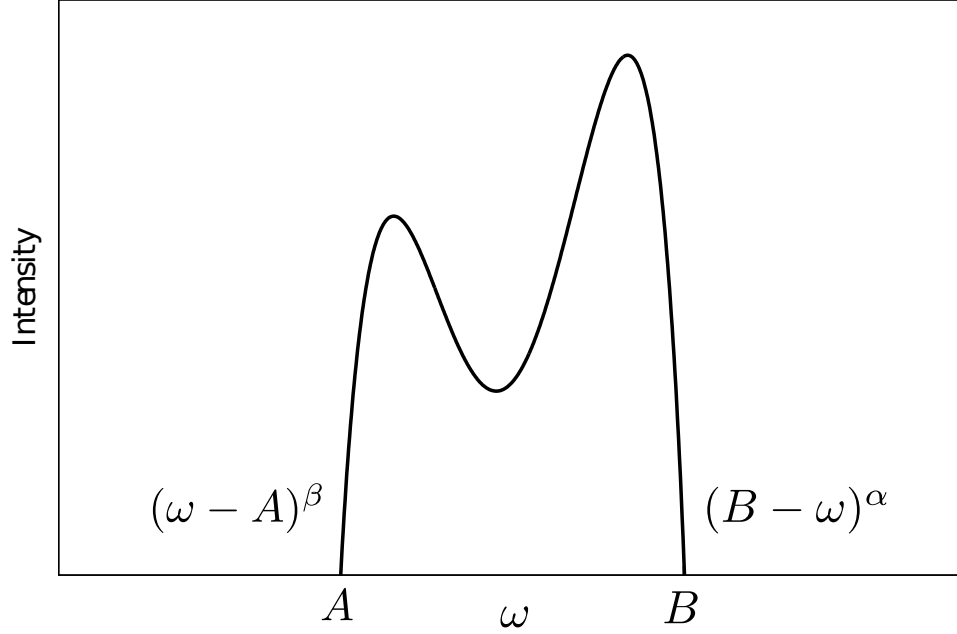


Figure 7.3: Graphical illustration of the band edge singularities in the DSF.

This approach is limited by two facts. On the one hand we need to choose a lower bound for n high enough, so that the terms in $\mathcal{O}\left(\frac{1}{n^3}\right)$ are already small to obtain a useful fit. On the other hand we need to choose an upper bound for n low enough, so that the limitation of the Hilbert space in the Lanczos tridiagonalization does not spoil the convergence of the sequences $\{a_n, b_n\}$.

Due to these complementary requirements, the obtained exponents can contain rather large numerical errors.

For two free hardcore particles on a chain, the band edge singularities are known to be $\alpha = \beta = 1/2$, see Ref. [62, 63]. We expect this behaviour also to be true in the case of the TFIM because here the particle interaction does not exist in the exact solution. In general we expect to see a change in the singularities once a bound state merges with a continuum of states, see also Ref. [52].

In the case $\alpha = \beta = 1/2$ the constraints (7.3.41a) and (7.3.41b) yield

$$a_n = a_\infty + \mathcal{O}\left(\frac{1}{n^3}\right) \quad (7.3.43a)$$

$$b_n = b_\infty + \mathcal{O}\left(\frac{1}{n^3}\right). \quad (7.3.43b)$$

We confirm this assumption in the two-particle case later in this chapter.

7.4 S^{zz} dynamical structure factor

In this section we investigate the transverse structure factor S^{zz} . Due to the fact that the observable σ^z stays local in the Jordan-Wigner representation of the TFIM, the DSF can also be obtained analytically. Exact expressions can be found in Ref. [38] and in the zero temperature case read

$$S^{zz}(Q, \omega) = \int_{-\pi}^{\pi} dk_1 \frac{1 - f(Q, k_1)}{4} \delta(\omega - \omega(k_1 - Q/2) - \omega(k_1 + Q/2)), \quad (7.4.44)$$

with

$$f(Q, k_1) = \frac{(\Gamma + \frac{J}{2} \cos(k_1 - Q/2)) (\Gamma + \frac{J}{2} \cos(k_1 + Q/2))}{\omega(k_1 - Q/2) \omega(k_1 + Q/2)}. \quad (7.4.45)$$

As we can see in the δ -function in Eq. (7.4.44) the DSF only consists of a two-particle continuum. Note that even with rising parameter J , no weight is shifted towards higher particle spaces. We emphasize that this fact can easily be explained within the string operator algebra. The corresponding local operator $\sigma_j^z = O_{j,0}$ is part of the string algebra, therefore our effective observable after the CUT consists of a linear combination of string operators,

$$\sigma_{j,\text{eff}}^z = \sum_d o_{j+d} O_{j+d,0} + \sum_{d,n} o_{j+d,n}^{+-} (O_{j+d,n}^{+-} + \text{h.c.}) + o_{j+d,n}^{++} (O_{j+d,n}^{++} + \text{h.c.}) \quad (7.4.46)$$

where the maximum range n is limited by the order of calculation. Therefore, our starting vector can at most create two excitations in the system.

Another side effect of the string property is that we can again reach very high orders, even for our local observable transformation. Because we have to transform a non translational-invariant operator, we additionally have to consider the positions $j+d$ and the starting site j . Therefore the computation time increases significantly but we were still able to achieve a maximum order of 128.

Once the local observable transformation is completed, we calculate the starting vector $\sigma_{\text{eff}}^z|_0^2(Q)|0\rangle$. Note that for computational reasons we consider the Pauli matrices σ instead of the spin operators S . This modifies our sum rule in Eq. (7.1.6). Then we apply the Lanczos algorithm in order to obtain the continued fraction coefficients. Note that we also need the effective Hamiltonian H_{eff} for the Lanczos tridiagonalization. With the help of the continued fraction coefficients and the square root terminator we finally obtain the DSF.

Note that the restriction to a fixed quasi-particle subspace is only possible with the effective Hamiltonian and the effective observable, because in the original Hamiltonian particle number conservation does not hold.

Overview plots for the DSF obtained in this way are shown in Figs. 7.4, 7.5 and 7.6,

all for an order 128. In these plots we see the two-particle continuum in dependence of total momentum Q and energy ω .

First note that the overall two-particle intensity rises for larger parameters J . This is due to the fact the transverse magnetization decreases and therefore spectral weight is gained in the two-particle channel.

Furthermore we see that for small parameters most of the weight is concentrated in the lower branch of the Brillouin zone while this swaps upon going to larger parameters. Note the singularity inside the continuum on the right side of the Brillouin zone that separates two regions with low and high spectral weight, clearly visible for the case $J = 1.9\Gamma$. Knowing the exact expression (7.4.44) we can argue that this originates from the δ -function and therefore from the two-particle density of states, as the function $f(Q, k_1)$ is smooth and differentiable everywhere as long as $J < 2\Gamma$.

An additional feature is the rise of the two-particle bandwidth of the DSF upon increasing J . For $J = 0$ the two-particle continuum is zero everywhere. Then, a finite particle hopping creates a two-particle continuum centered around the line $\omega = 2\Gamma$. This can be attributed to the one-particle energy $\omega(q)$ becoming more and more dispersive with rising parameter. Note that the minimal two-particle energy is always located at $Q = 0$ which can be explained by two particles having momenta $q_1 = \pi$ and $q_2 = -\pi$ and therefore an energy which is twice the energy gap.

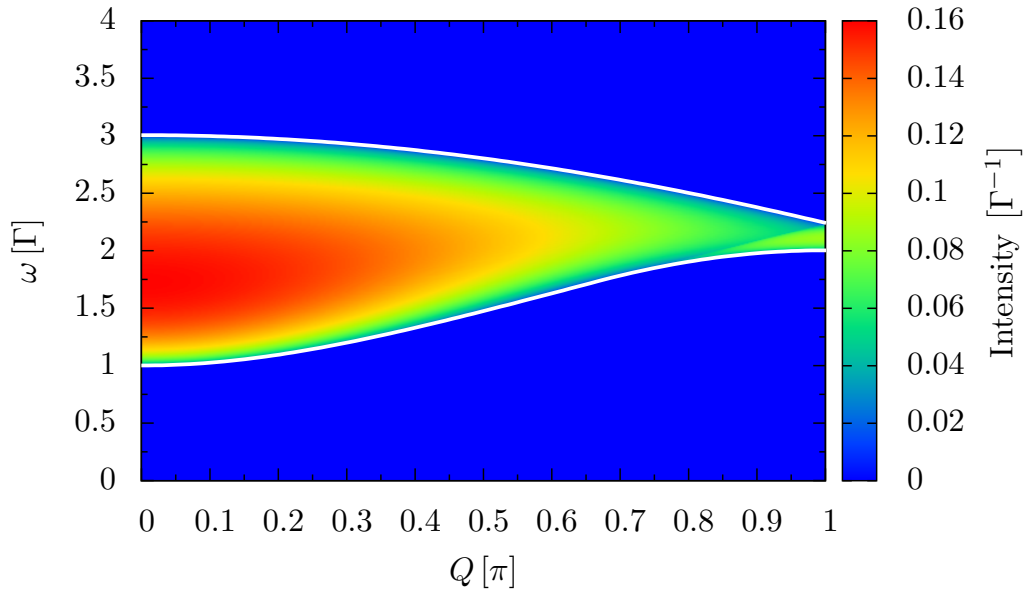


Figure 7.4: The DSF S^{zz} for the parameter $J = \Gamma$. The maximum range for the Lanczos algorithm is $d_{\max} = 1000$ sites, the continued fraction was evaluated to a depth of 50 and then terminated by the square root terminator. The color indicates the spectral density, see legend to the right. The upper and lower edge of the two-particle continuum are indicated by white lines.

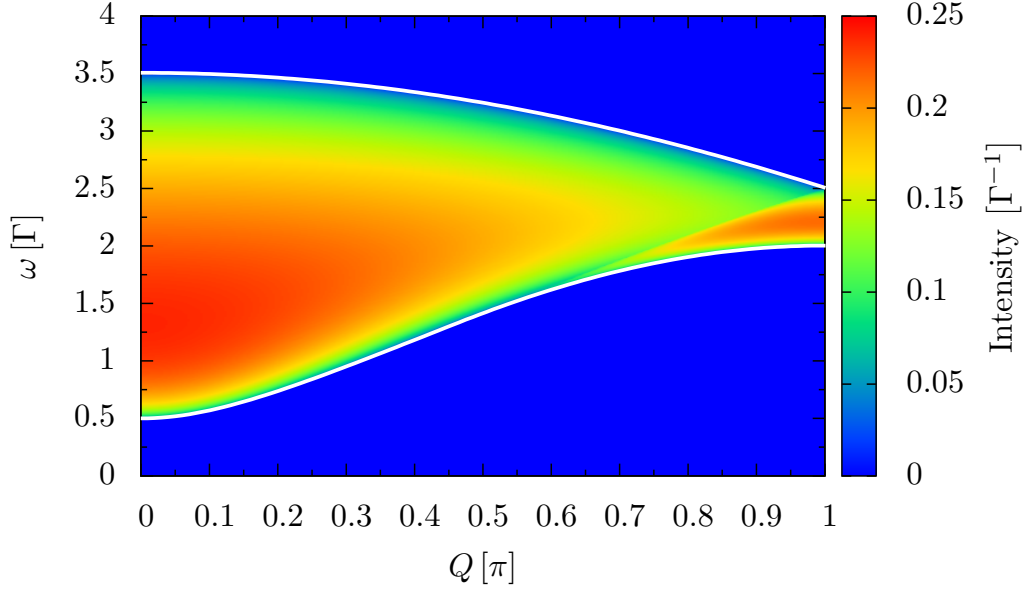


Figure 7.5: The DSF S^{zz} for the parameter $J = 1.5\Gamma$. The maximum range for the Lanczos algorithm is $d_{\max} = 1000$ sites, the continued fraction was evaluated to a depth of 50 and then terminated by the square root terminator. The color indicates the spectral density, see legend to the right. The upper and lower edge of the two-particle continuum are indicated by white lines.

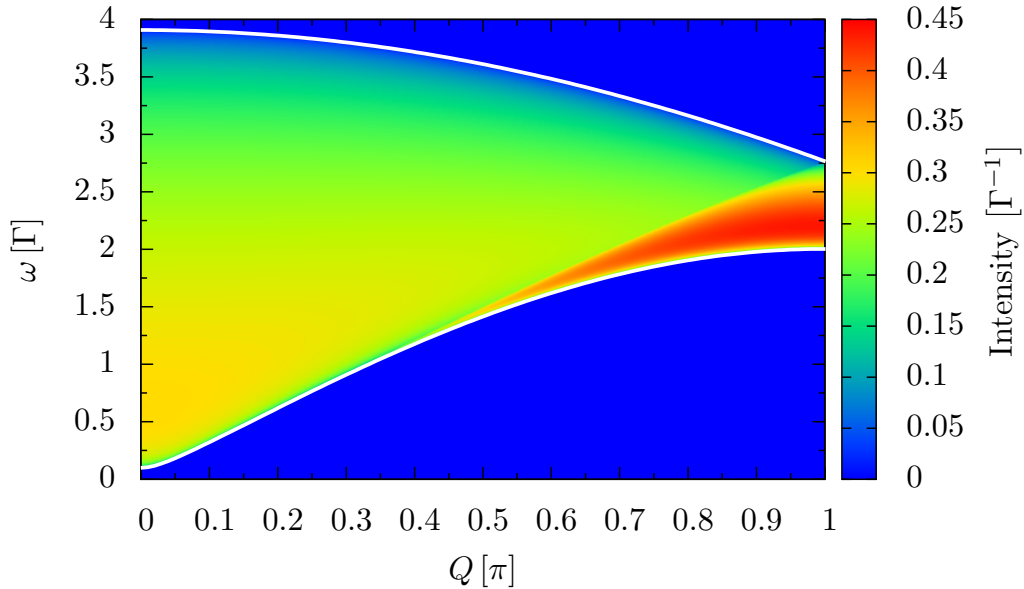


Figure 7.6: The DSF S^{zz} for the parameter $J = 1.9\Gamma$. The maximum range for the Lanczos algorithm is $d_{\max} = 1000$ sites, the continued fraction was evaluated to a depth of 50 and then terminated by the square root terminator. The color indicates the spectral density, see legend to the right. The upper and lower edge of the two-particle continuum are indicated by white lines.

We want to investigate more profoundly how the CUT calculation differs from the exact calculation by examining the DSF for fixed parameters J and total momenta Q . This is depicted in Figs. 7.7, 7.8 and 7.9. The plot shows S^{zz} for the parameters $J = \Gamma$, $J = 1.5\Gamma$ and $J = 1.9\Gamma$ and for the momenta $Q = 0.1\pi$, $Q = \pi/2$ and $Q = \pi$, calculated by the CUT in order 128 in comparison with the exact result.

First note the very good agreement for all parameters and momenta. The form of the DSF is very close to a half ellipse, which is reasonable because the continued fraction coefficients converge very quickly towards their final values a_∞ and b_∞ . This fast convergence is close to the case in Eq. (7.3.40b), where the exact DSF is given by a half ellipse.

With rising parameter J more spectral weight is concentrated at the lower band edge, which can be attributed to a complex interplay between momentum- and energy-conservation. For the parameter $J = 1.9$ and $Q = \pi/2$ we also see the singularity inside the continuum of the DSF which separates the two regions of spectral weight.

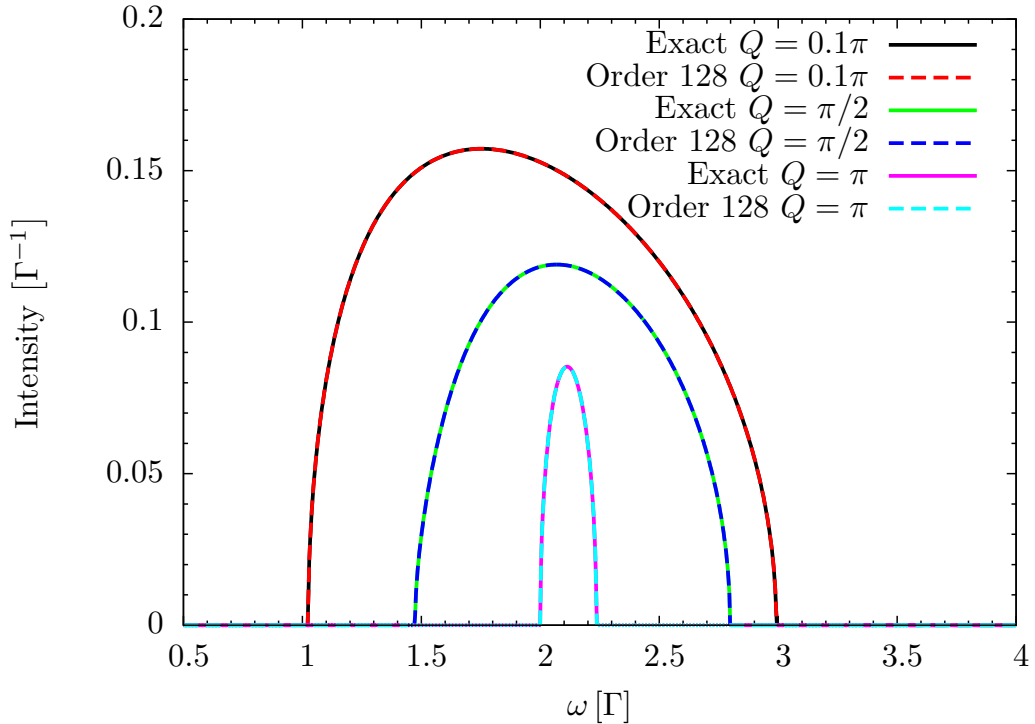


Figure 7.7: DSF S^{zz} for the parameter $J = \Gamma$ for three total momenta Q . The maximum range for the Lanczos algorithm is $d_{\max} = 4000$ sites, the continued fraction was evaluated to a depth of 100 and then terminated by the square root terminator.

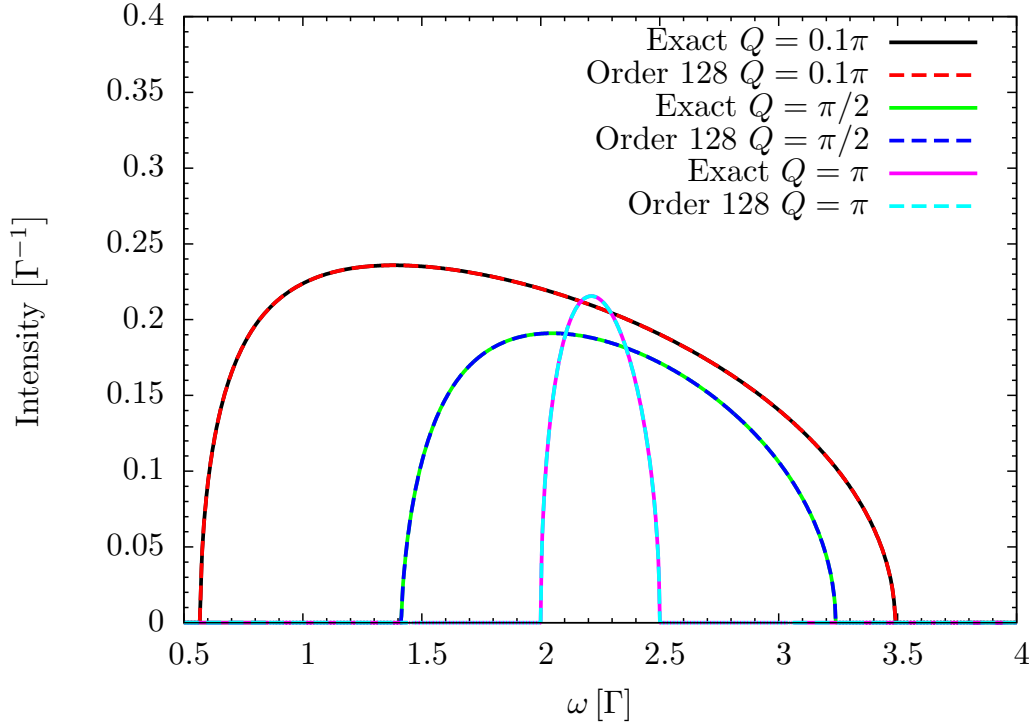


Figure 7.8: DSF S^{zz} for the parameter $J = 1.5\Gamma$ for three total momenta Q . The maximum range for the Lanczos algorithm is $d_{\max} = 4000$ sites, the continued fraction was evaluated to a depth of 100 and then terminated by the square root terminator.

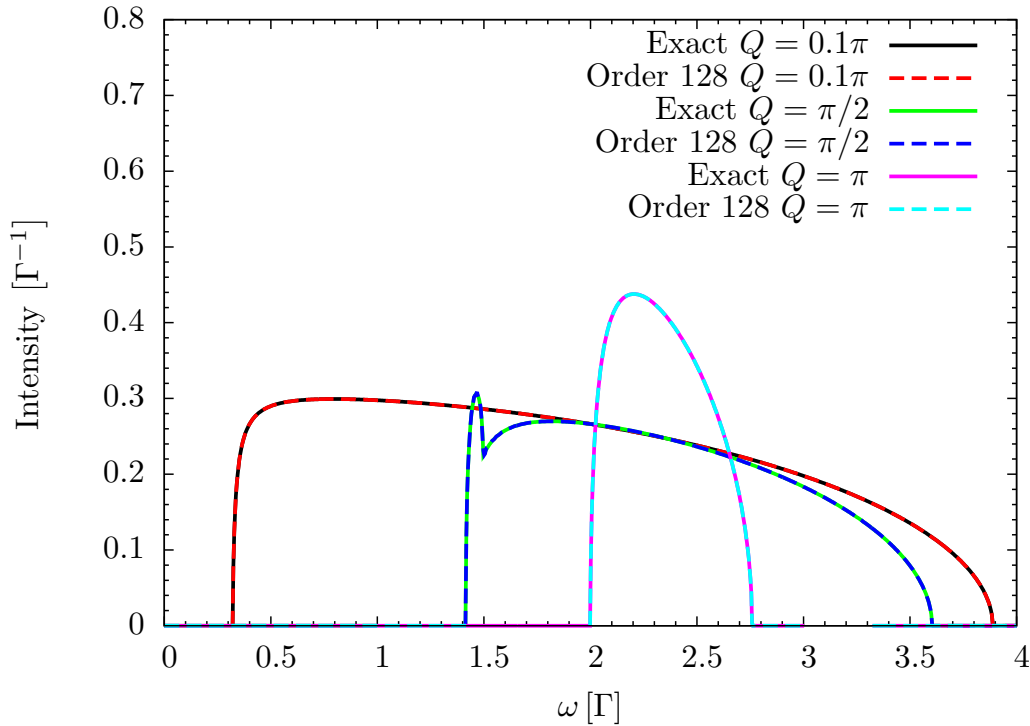


Figure 7.9: DSF S^{zz} for the parameter $J = 1.9\Gamma$ for three total momenta Q . The maximum range for the Lanczos algorithm is $d_{\max} = 4000$ sites, the continued fraction was evaluated to a depth of 100 and then terminated by the square root terminator.

To investigate the numerical errors in more detail, we look at the absolute difference between the exact DSF and the CUT calculation. This quantity is depicted in Figs. 7.10, 7.11 and 7.12 for the same parameters and momenta as above. Note that the left hand scala is logarithmic. By comparing the different graphs it becomes obvious that the error strongly depends on the total momentum Q . The error is lower in the middle of the continuum than at the band edge singularities. This is expected due to the strong change of the DSF at these points.

On average the error is below $10^{-6}\Gamma^{-1}$ even for large parameters J . We deduce that the errors are mainly produced by inaccuracies in the Lanczos tridiagonalization and the limitation of the maximum range in the transformation of the observable by the CUT. Nonetheless the errors are still very small and justify our approach.

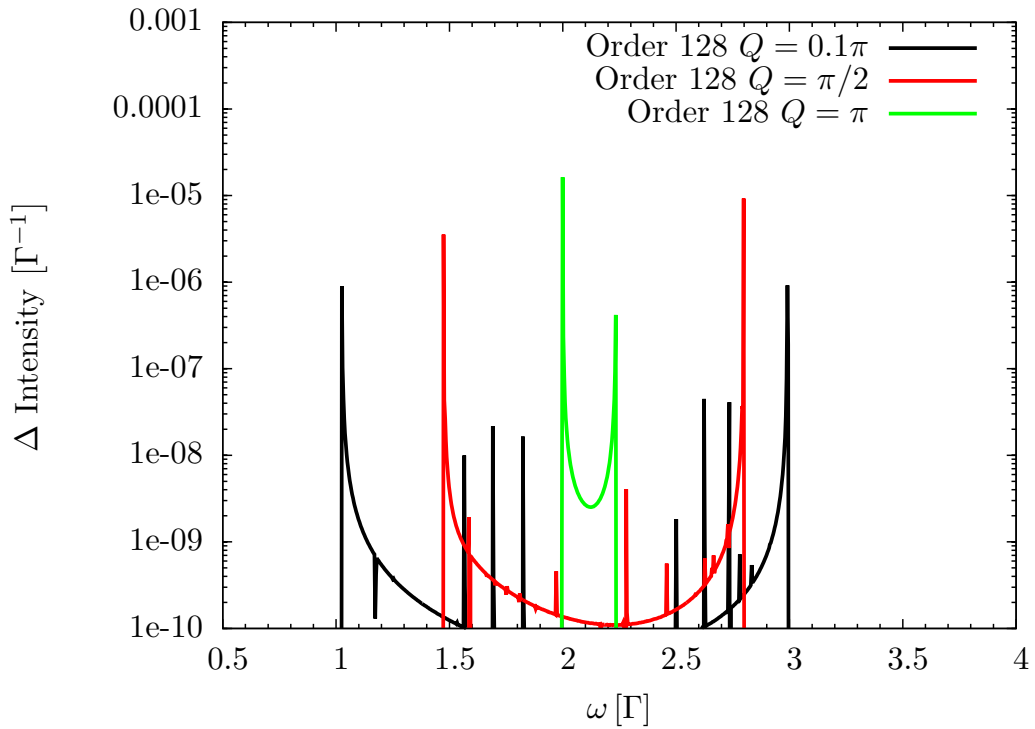


Figure 7.10: Difference of the exact DSF S^{zz} and the CUT calculation for the parameter $J = \Gamma$. The maximum range for the Lanczos algorithm is $d_{\max} = 4000$ sites, the continued fraction was evaluated to a depth of 100 and then terminated by the square root terminator.

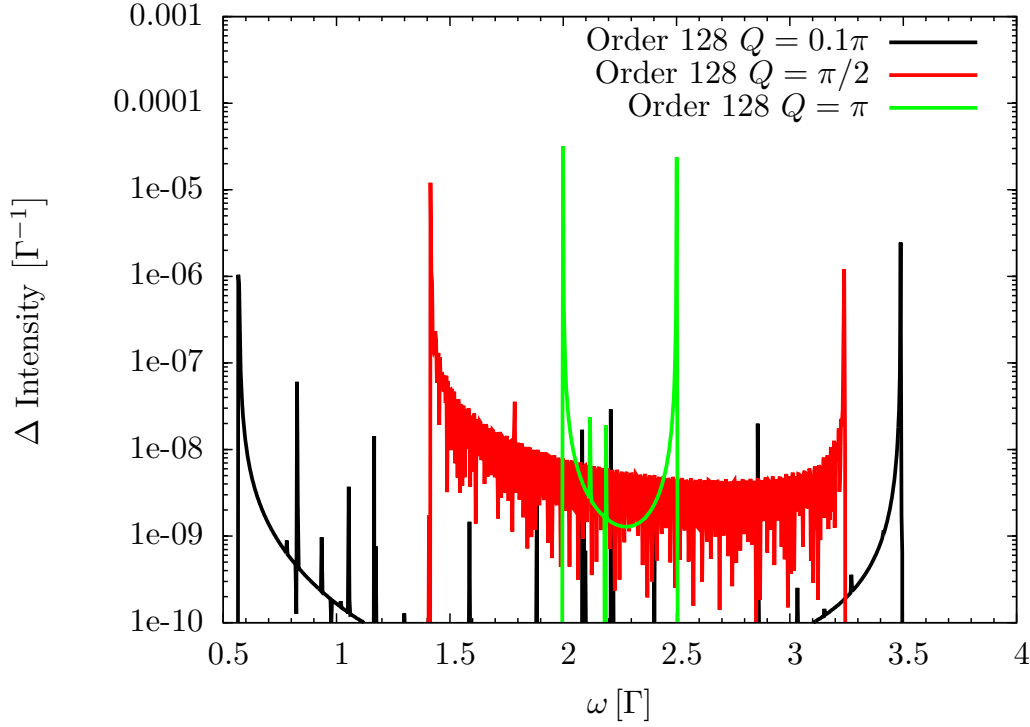


Figure 7.11: Difference of the exact DSF S^{zz} and the CUT calculation for the parameter $J = 1.5\Gamma$. The maximum range for the Lanczos algorithm is $d_{\max} = 4000$ sites, the continued fraction was evaluated to a depth of 100 and then terminated by the square root terminator.

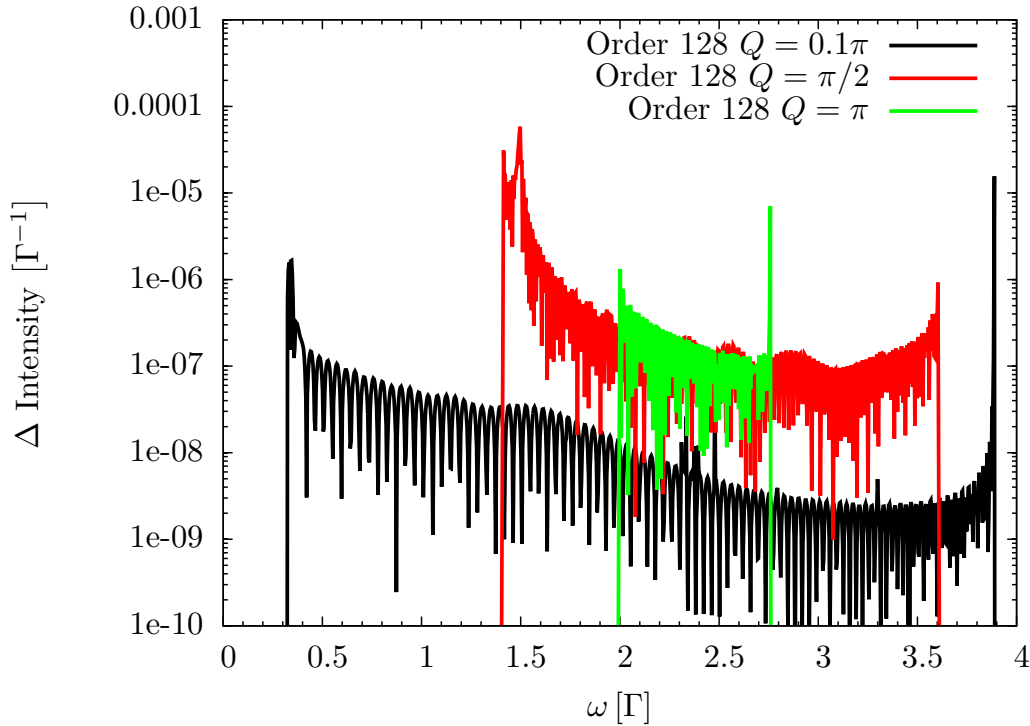


Figure 7.12: Difference of the exact DSF S^{zz} and the CUT calculation for the parameter $J = 1.9\Gamma$. The maximum range for the Lanczos algorithm is $d_{\max} = 4000$ sites, the continued fraction was evaluated to a depth of 100 and then terminated by the square root terminator.

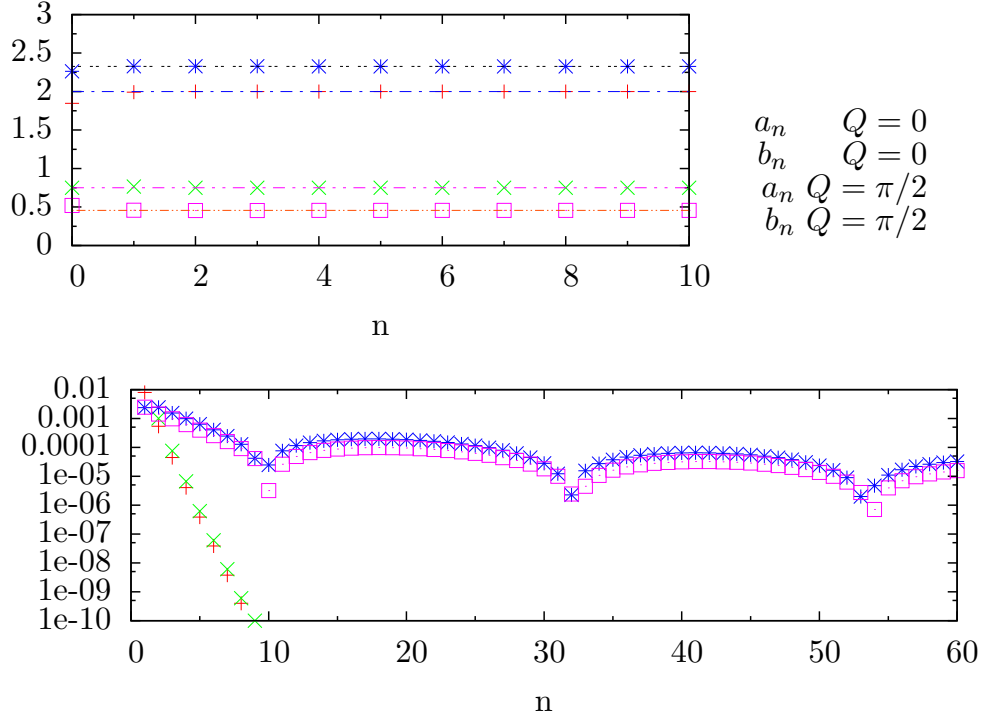


Figure 7.13: Continued fraction coefficients for the case $J = 1.5\Gamma$ and total momenta $Q = 0$ and $Q = \pi/2$. The upper plot shows the first ten coefficients converging rapidly to their limit values indicated by horizontal lines. The lower plot shows the absolute difference between the coefficients and their final values.

Next we investigate how the continued fraction coefficients approach their limit values and how the limitation of the considered Hilbert space hampers the convergence. The continued fraction coefficients for the case $J = 1.5\Gamma$ and total momenta $Q = 0$ and $Q = \pi/2$ are shown in Fig. 7.13.

The coefficients for the case $Q = 0$ approach their limit even exponentially. Therefore we know by Eq. (7.3.41a) and Eq. (7.3.41b) that the exponent of the band edges are both $1/2$, as expected.

For the case $Q = \pi/2$ the coefficients do not converge so rapidly, which is still plausible. Therefore we plotted the coefficients for this case versus $1/n^2$ to check if they are in $\mathcal{O}(1/n^2)$, see Fig. 7.14. Both coefficients oscillate around the final value which can not be described by Eq. (7.3.41a) and Eq. (7.3.41b). This again verifies that the exponents are $1/2$.

Note that the limitation to a finite Hilbert space can have a strong effect on the convergence of the continued fraction coefficients. This is shown in Fig. 7.15. By reducing the maximum range to 200 sites the convergence of the continued fraction coefficients is first lowered and finally spoiled completely at $n \approx 55$, which supports our previous statement concerning the extraction of exponents from the continued fraction coefficients.

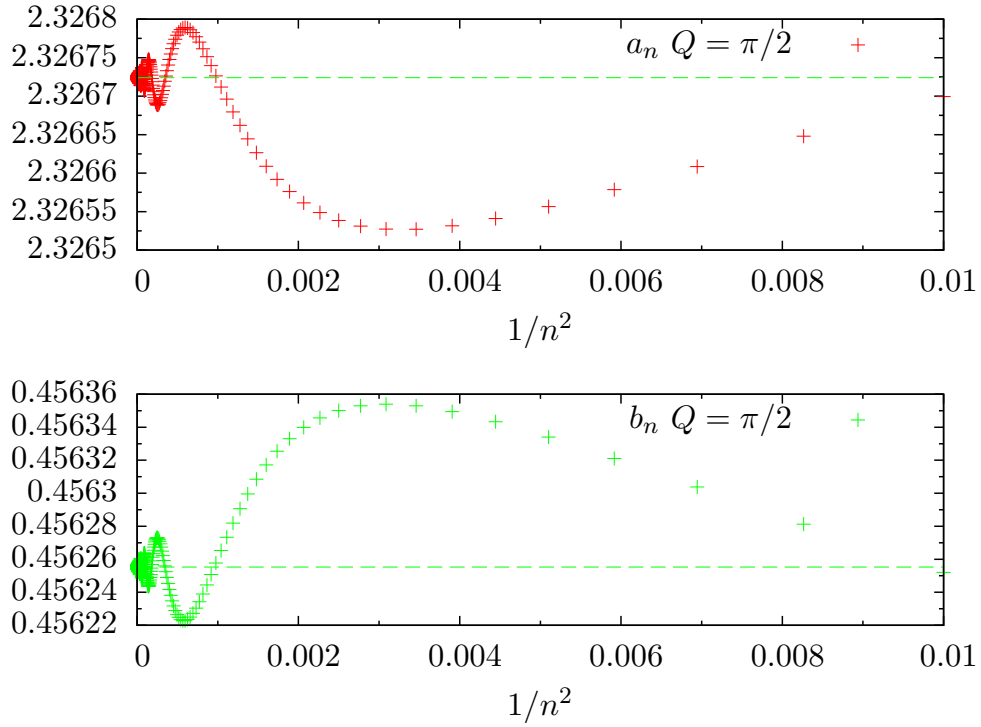


Figure 7.14: Continued fraction coefficients for the case $J = 1.5\Gamma$ and total momentum $Q = \pi/2$. The upper plot shows the coefficients a_n and the lower one the coefficients b_n . The limit values are indicated by horizontal lines. Note that the x-axis scale is $1/n^2$.

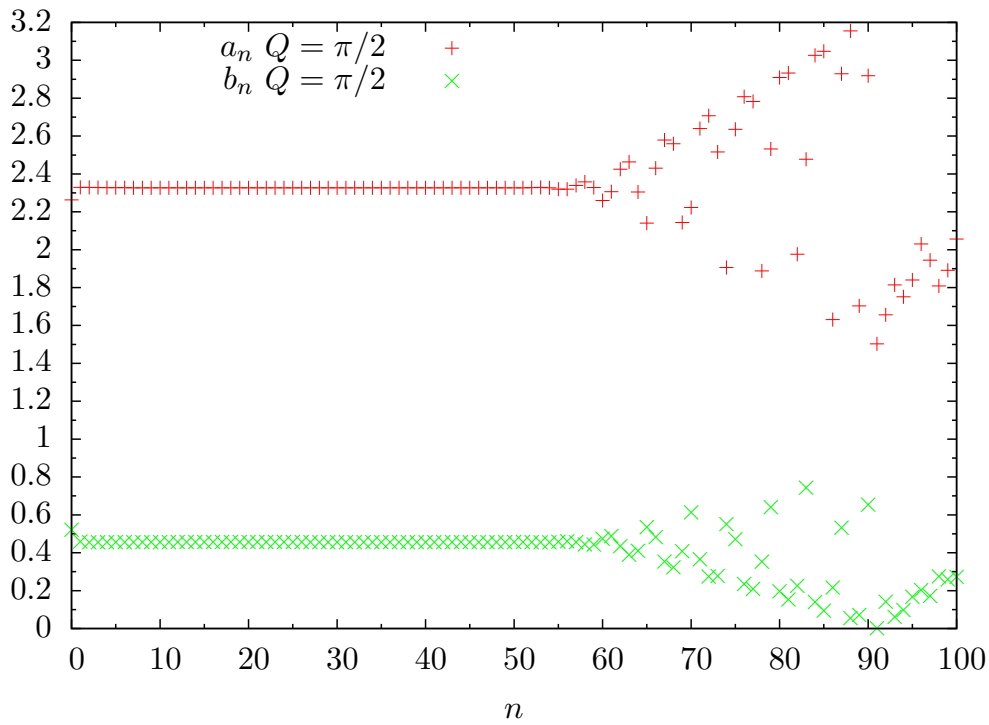


Figure 7.15: Continued fraction coefficients for the case $J = 1.5\Gamma$ and total momentum $Q = \pi/2$. The maximum range for the Lanczos algorithm is lowered to $d_{\max} = 200$ sites. At $n \approx 55$ the restriction of the Hilbert space spoils the convergences of the coefficients.

7.5 S^{xx} dynamical structure factor

In this section we discuss the results for the longitudinal structure factor S^{xx} . Since σ^x creates an odd number of particles and the generator of the CUT preserves the parity of an observable, the DSF S^{xx} consists of $1, 3, 5, \dots$ particle contributions.

In Ref. [19] Hamer et al. proposed an analytic expression for the one-particle contribution. To our knowledge no data is available in literature for higher quasi-particle contributions.

In the first part of this section we present our results for the one-particle contribution to the longitudinal DSF. We compare our results to those of Hamer et al. In the second part we consider the three-particle contribution to S^{xx} as an example of higher quasi-particle spaces.

Note that the local observable σ_j^x transforms into a non-local operator under the Jordan-Wigner transformation, acting on an extensive number of sites. Therefore, no easy analysis of this observable in fermionic terms is possible. This problem is avoided in the string operator basis (5.1.7). On the other hand, the observable σ_j^x is not part of the string algebra, therefore its structure is more complicated, see Eq. (5.4.56a). This complicated structure prevents us from achieving very high orders, because the number of representatives to track grows exponentially with every order.

We were, however, able to obtain results up to order 38. Here the computational effort reaches its limit, because the contributions to the differential equation system take more than 8 GB of memory.

7.5.1 One-particle contributions

As explained in section 7.2.1 the one-particle structure factor consists of the equal time structure factor and a δ -function in energy space,

$$S_1^{xx}(\omega, Q) = \underbrace{\left| \sum_{d_0, j} s_{\text{eff}, j}^{d_0}(Q) \right|^2}_{S_1^{xx}(Q)} \delta(\omega - \omega(Q)). \quad (7.5.47)$$

Therefore our quantity of interest is the one-particle equal time structure factor $S_1^{xx}(Q)$. Within the CUT framework this quantity can be extracted from the effective observable $\sigma_{j, \text{eff}}^x$, by Fourier transformation of the terms that create exactly one particle. Note that for computational reasons we consider the Pauli matrices σ instead of the spin operators S . This only modifies our sum rule in Eq. (7.1.6).

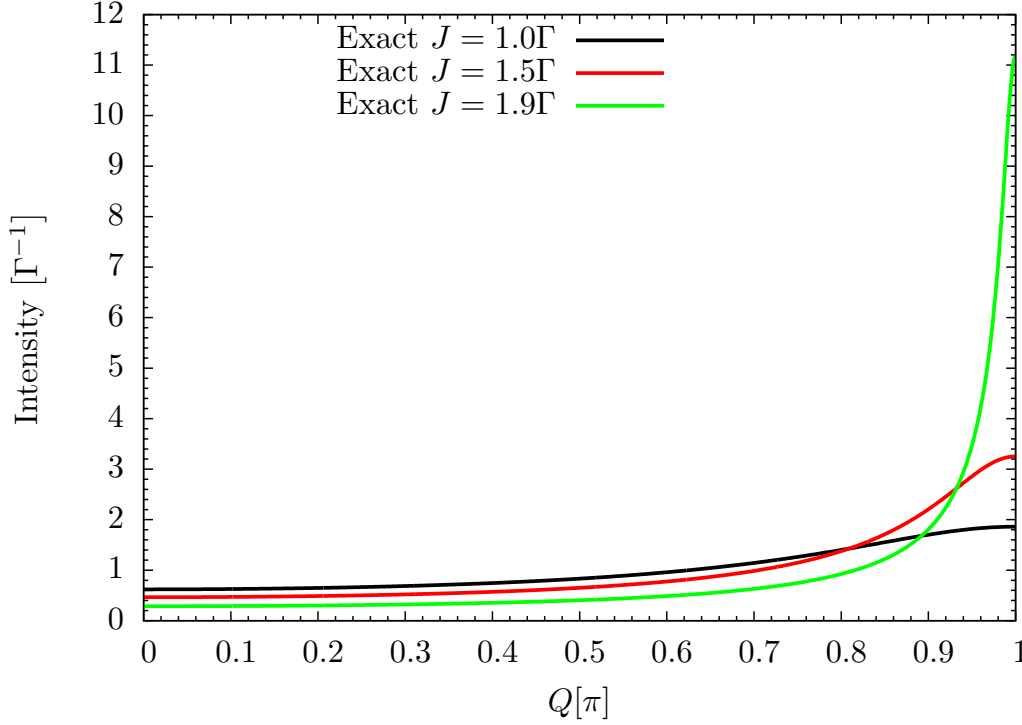


Figure 7.16: Overview of the one-particle equal time structure factor $S_1^{xx}(Q)$ for different parameters J . For $J \rightarrow 2\Gamma$ the value at $Q = \pi$ diverges although the integral remains finite.

In 2006 Hamer et al. analyzed the one-particle spectral weights of the TFIM and proposed the analytic expression

$$S_1^{xx}(Q) = \frac{\left[1 - \left(\frac{J}{2\Gamma}\right)^2\right]^{\frac{1}{4}}}{\omega(Q)}. \quad (7.5.48)$$

In the following we refer to this expression as the exact one and compare it to our results. An overview of the exact equal time structure factor is given in Fig. 7.16. We can see that the structure factor at $Q = \pi$ diverges when $J \rightarrow 2\Gamma$. Note that the divergence of the structure factor is expected and the exponents can be described within a general scaling theory developed by Sachdev [16].

In Figs. 7.17, 7.18 and 7.19 we compare the CUT results with the exact expression for the parameters $J = \Gamma$, $J = 1.5\Gamma$ and $J = 1.9\Gamma$. As expected the results become worse upon approaching the QCP. A closer analysis reveals that the highest absolute error occurs at the critical wave vector $Q = \pi$. The DSF diverges at this point, so that the relative error, not shown in the graphs, remains essentially constant over the whole Brillouin zone.

The plot for the parameter $J = 1.9\Gamma$ also shows that the results improve on passing to higher orders. Consequently our results differ only by about of 1% even close to the QCP at $J = 1.9\Gamma$. Therefore, we agree with the results obtained by Hamer et al.

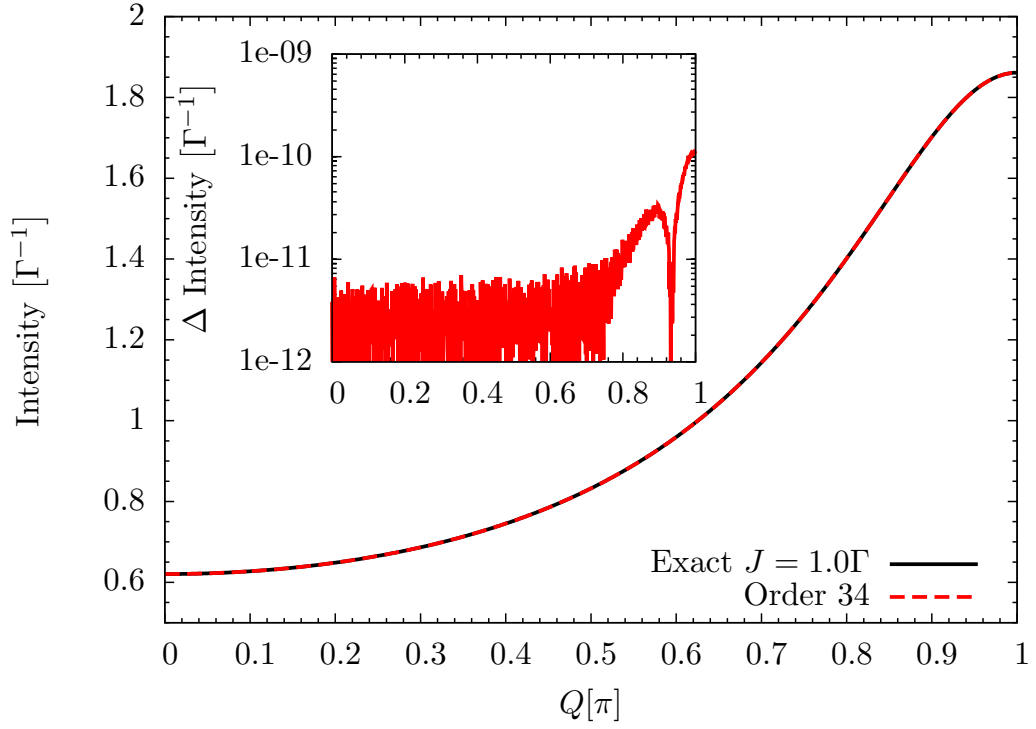


Figure 7.17: One-particle equal time structure factor $S_1^{xx}(Q)$ for the parameter $J = \Gamma$. Comparison of the exact expression with the CUT results. The inset shows the absolute difference between the exact curve and the CUT.

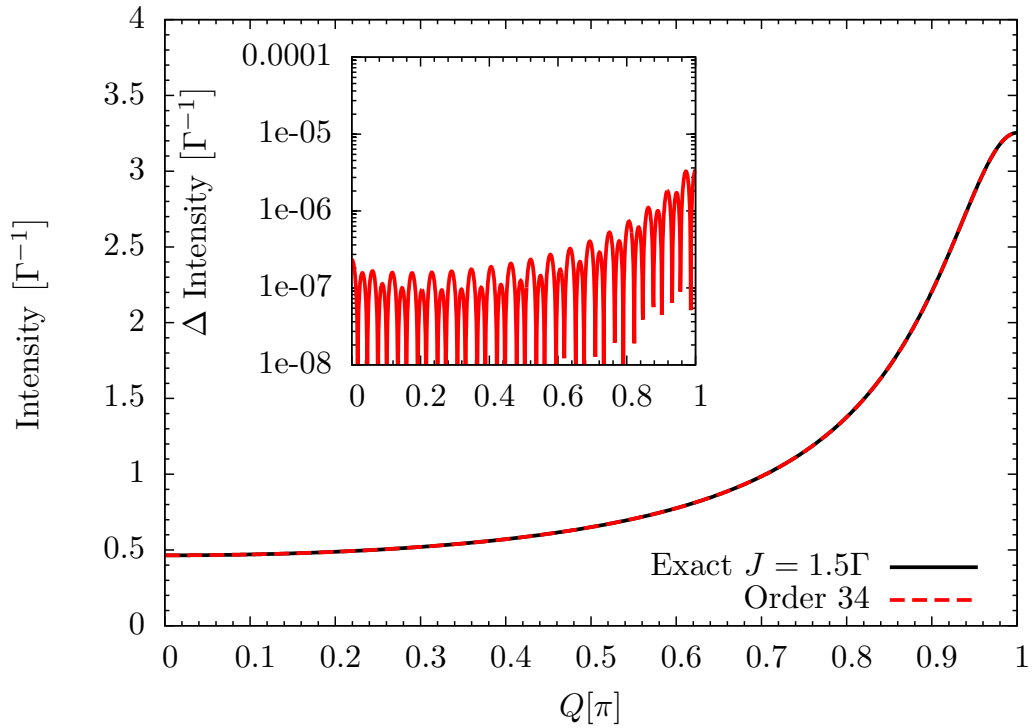


Figure 7.18: One-particle equal time structure factor $S_1^{xx}(Q)$ for the parameter $J = 1.5\Gamma$. Comparison of the exact expression with the CUT results. The inset shows the absolute difference between the exact curve and the CUT.

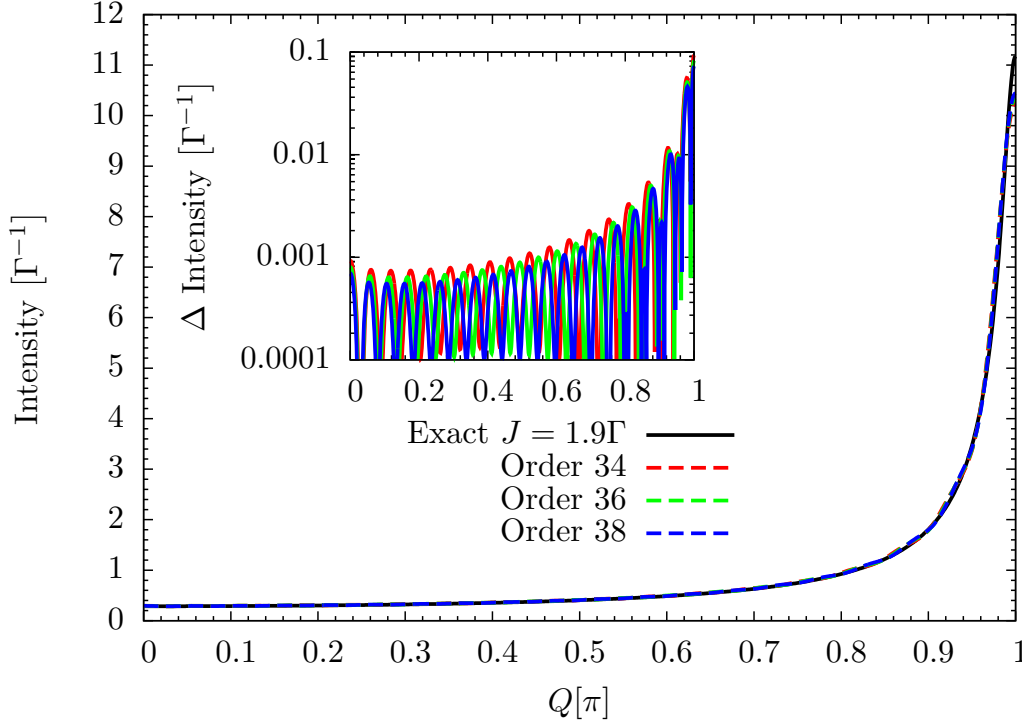


Figure 7.19: One-particle equal time structure factor $S_1^{xx}(Q)$ for the parameter $J = 1.9\Gamma$. Comparison of the exact expression with the CUT results. The inset shows the absolute difference between the exact curve and the CUT.

Another quantity of interest is the integrated equal time structure factor, known as the one-particle spectral weight,

$$S_1^{xx} = \frac{1}{\pi} \int_0^\pi S_1^{xx}(Q) dQ. \quad (7.5.49)$$

As explained before, the absolute spectral weight for all particle channels is fixed by a sum rule. Therefore the relative one-particle spectral weight measures the intensity of one-particle excitations in comparison to the weight in higher particle excitations.

This quantity is depicted in Fig. 7.20. As we can see, this quantity shows a very sharp edge at $J \approx 2\Gamma$ and has a singularity at the QCP. To explain this sharp edge we also display the correlation length ξ on the upper x-axis. This quantity is given approximately by the expression

$$\xi \approx \frac{v}{\Delta} \quad (7.5.50)$$

where Δ is the energy gap and v is the spin wave velocity. The latter can be obtained by fitting $2v \cos(Q/2)$ to the maximum of the dispersion. Hence the correlation length diverges at the QCP when the energy gap closes. The CUT agrees very well with the exact results as long as the order of calculation is below the correlation length, because with every order we can describe approximately one additional range of physical processes.

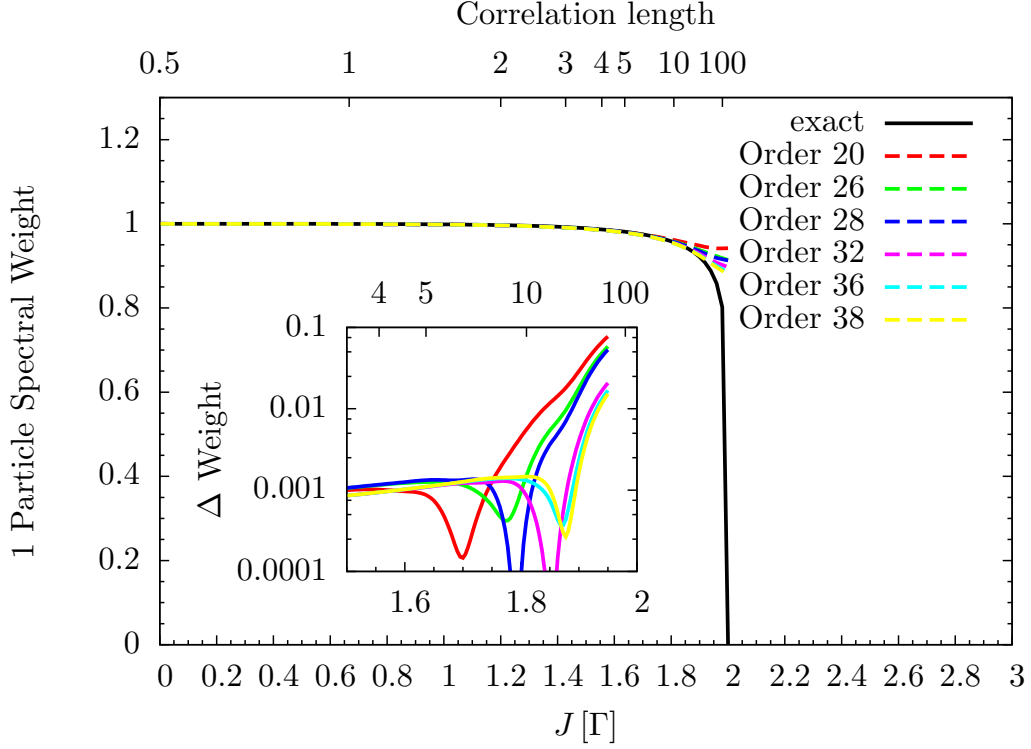


Figure 7.20: One-particle spectral weight as function of the parameter J . Comparison of the exact expression with the CUT results. The inset shows the absolute difference between the exact curve and the CUT.

In our previous considerations this was no problem because we were able to achieve orders > 100 . Due to the very sharp edge of the one-particle spectral weight the CUT is not able to capture this feature. But the agreement improves on increasing order.

7.5.2 Three-particle contributions

As in the two-particle $S^{zz}(\omega, Q)$ case, the three-particle case $S_3^{xx}(\omega, Q)$ consists of a continuum of states. We are again limited to a maximum order 38, including the reduction of the DES, due to the complicated structure of the local observable σ^x .

Once the local observable transformation is completed, we calculate the starting vector $\sigma_{\text{eff}}^x|_0^3(Q)|0\rangle$. Then we apply the Lanczos algorithm in order to obtain the continued fraction coefficients. Note that we also need the effective Hamiltonian H_{eff} for the Lanczos tridiagonalization. With the help of the continued fraction coefficients and the square root terminator we then obtain the DSF.

In contrast to the two-particle case we have to deal with two relative distances d_1 and d_2 . If we restrict these distances to d_{max} , the considered Hilbertspace has a size of d_{max}^2 and it is therefore limited to smaller values than in the two-particle case. Therefore the coefficients must be carefully checked to avoid spoiled convergence due to the finite range in the multi-particle states.

We again stress that the restriction to a fixed particle number space is only possible with the effective Hamiltonian and the effective observable, because the original Hamiltonian

is not particle number conserving.

Overview plots for the DSF obtained in this way are found in Figs. 7.21, 7.22 and 7.23, all for an order 38. In these plots we see the three-particle continuum in dependence of total momentum Q and energy ω .

Note that the overall intensity rises when increasing the coupling J , because spectral weight is transferred from the one-particle sector to the higher quasi-particle channels, compare Refs. [24–26].

In addition we notice that most of the spectral weight is concentrated in the lower half of the Brillouin zone for small parameters J . This slowly shifts for growing parameters similar to the S^{zz} case.

For $J = 1.9\Gamma$ most of the spectral weight is concentrated rather sharply at the lower edge of the continuum. This is in partial agreement with the S^{zz} case, where this tendency can be observed as well. Still the shape of the DSF differs strongly from the semi ellipse case.

Furthermore, we notice a slight wiggling for the case $J = 1.9\Gamma$, which must be attributed to the finite order calculation and to inaccuracies due to the restriction to a finite Hilbert space. Still we expect the errors to be rather small, especially when comparing it to the results for the one-particle structure factor.

Another observation is that the minimal three-particle energy is now located at $Q = \pi$. This can be understood in terms of three particles having momenta $q_1 = \pi$, $q_2 = -\pi$ and $q_3 = \pi$, all with the minimal energy Δ .

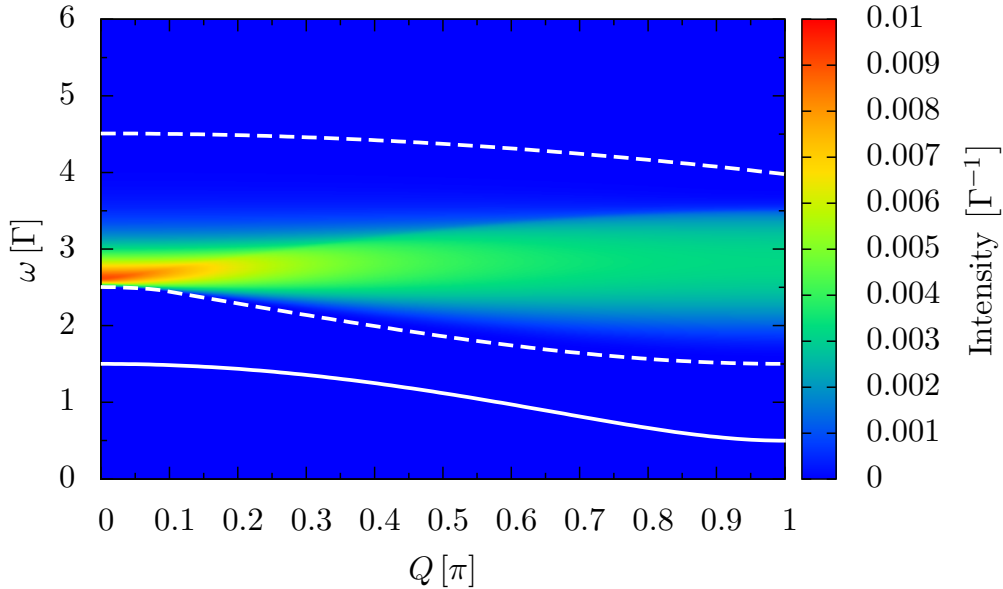


Figure 7.21: The DSF S_3^{xx} for the parameter $J = \Gamma$. The maximum range for the Lanczos algorithm is $d_{\max} = 100$ sites, the continued fraction was evaluated to a depth of 50 and then terminated by the square root terminator. The color indicates the spectral density, see legend to the right. The dispersion is indicated by the white solid line. The upper and lower edge of the two-particle continuum are indicated by white dashed lines.

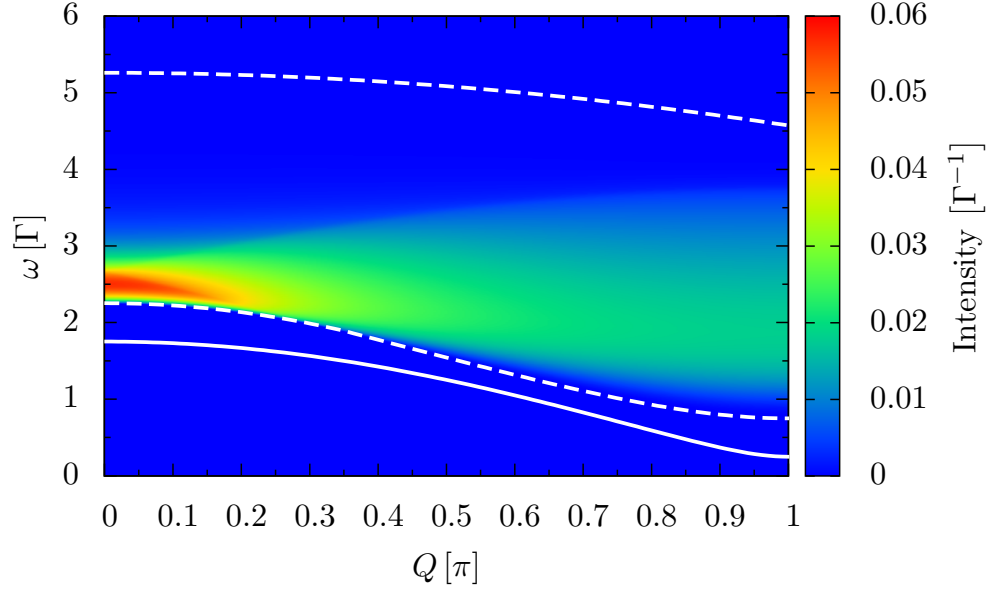


Figure 7.22: The DSF S_3^{xx} for the parameter $J = 1.5\Gamma$. The maximum range for the Lanczos algorithm is $d_{\max} = 100$ sites, the continued fraction was evaluated to a depth of 50 and then terminated by the square root terminator. The color indicates the spectral density, see legend to the right. The dispersion is indicated by the white solid line. The upper and lower edge of the two-particle continuum are indicated by white dashed lines.

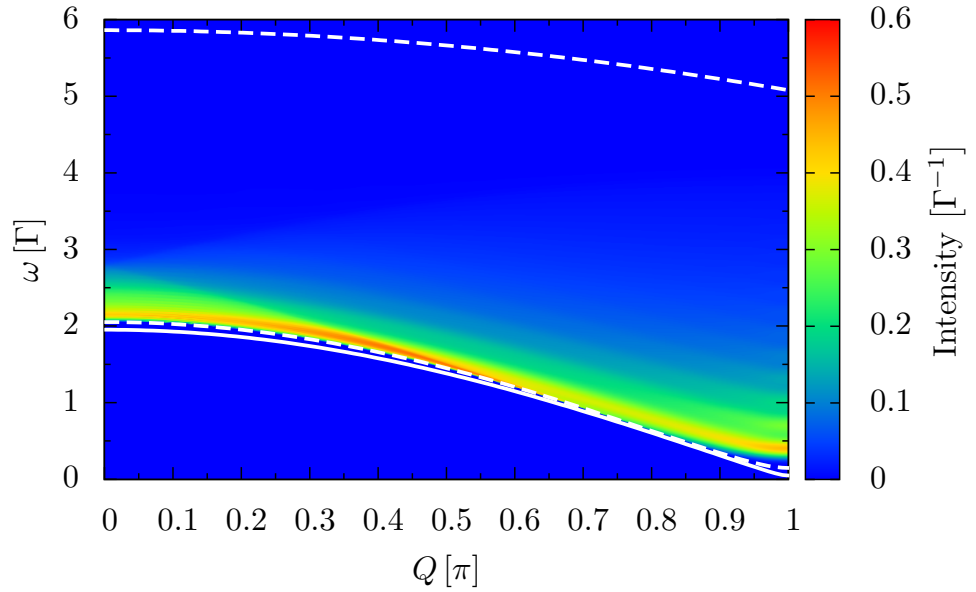


Figure 7.23: The DSF S_3^{xx} for the parameter $J = 1.9\Gamma$. The maximum range for the Lanczos algorithm is $d_{\max} = 100$ sites, the continued fraction was evaluated to a depth of 50 and then terminated by the square root terminator. The color indicates the spectral density, see legend to the right. The dispersion is indicated by the white solid line. The upper and lower edge of the two-particle continuum are indicated by white dashed lines.

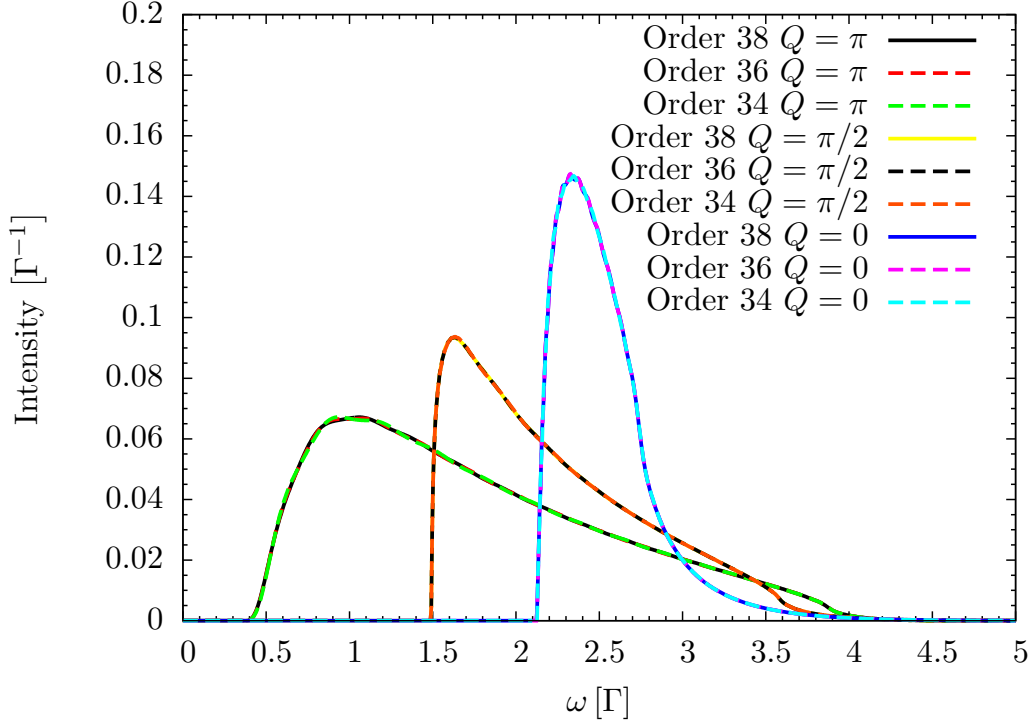


Figure 7.24: DSF S_3^{xx} for the parameter $J = 1.75\Gamma$ for three chosen total momenta Q . The maximum range for the Lanczos algorithm is $d_{\max} = 200$ sites, the continued fraction was evaluated to a depth of 100 and then terminated by the square root terminator.

To investigate the errors more quantitatively consider Fig. 7.24. Here we see S_3^{xx} for the parameter $J = 1.75\Gamma$ and momenta $Q = 0$, $Q = \pi/2$ and $Q = \pi$ for different orders. For this case, the results differ only slightly depending on the order of calculation and show good agreement even close to the QCP. We can also observe again, that most of the spectral weight is concentrated at the lower band edge for large values of J . For the two-particle case $S^{zz}(\omega, Q)$, we saw that the band edge singularities are $1/2$ as expected. Now we investigate the three-particle case $S_3^{xx}(\omega, Q)$. As in the two-particle case we use the constraint (7.3.41a) and (7.3.41a) by fitting a linear function to the continued fraction coefficients in dependence of $1/n^2$. This is shown in Figs. 7.25, 7.26 and 7.27, for the case $J = 1.5\Gamma$ with total momentum $Q = 0$, $Q = \pi/2$ and $Q = \pi$.

Note that no divergence is observed in Fig. 7.24, therefore we expect the exponents of the band edge singularities to be positive. In contrast to the two-particle case we clearly see no exponential decay towards the limit values. For all momenta both a_n and b_n show a linear behaviour for small enough $1/n^2$. We stress that the $\mathcal{O}(1/n^3)$ terms matter strongly up to $1/n^2 \approx 0.0002 \Rightarrow n \approx 70$.

Interestingly the slope for a_n differs from zero for $Q = 0$, which indicates that the lower and upper band edge singularity differ, cf. Eq. (7.3.41a). On the other hand, the slope is close to zero for $Q = \pi$, which indicates that the band edge singularities strongly depend on total momentum Q .

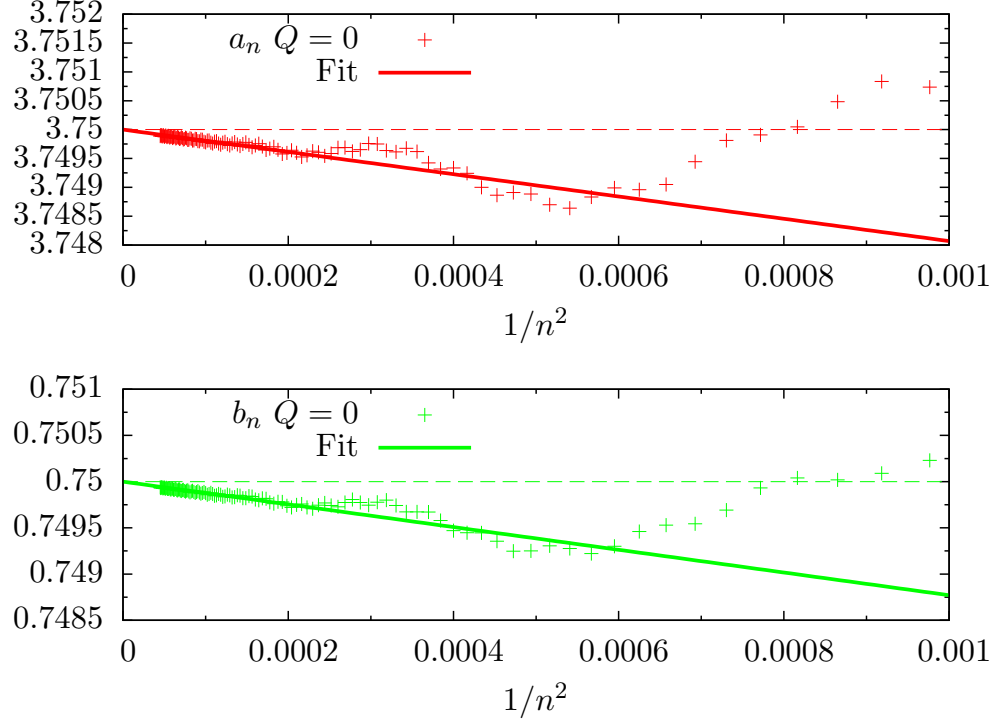


Figure 7.25: Continued fraction coefficients for the case $J = 1.5\Gamma$ and total momentum $Q = 0$. The upper panel shows the coefficients a_n and the lower panel shows the coefficients b_n . The limit values are indicated by horizontal lines. The red/green lines indicated linear fits for small $1/n^2$. Note that the x-axis scale is $1/n^2$.

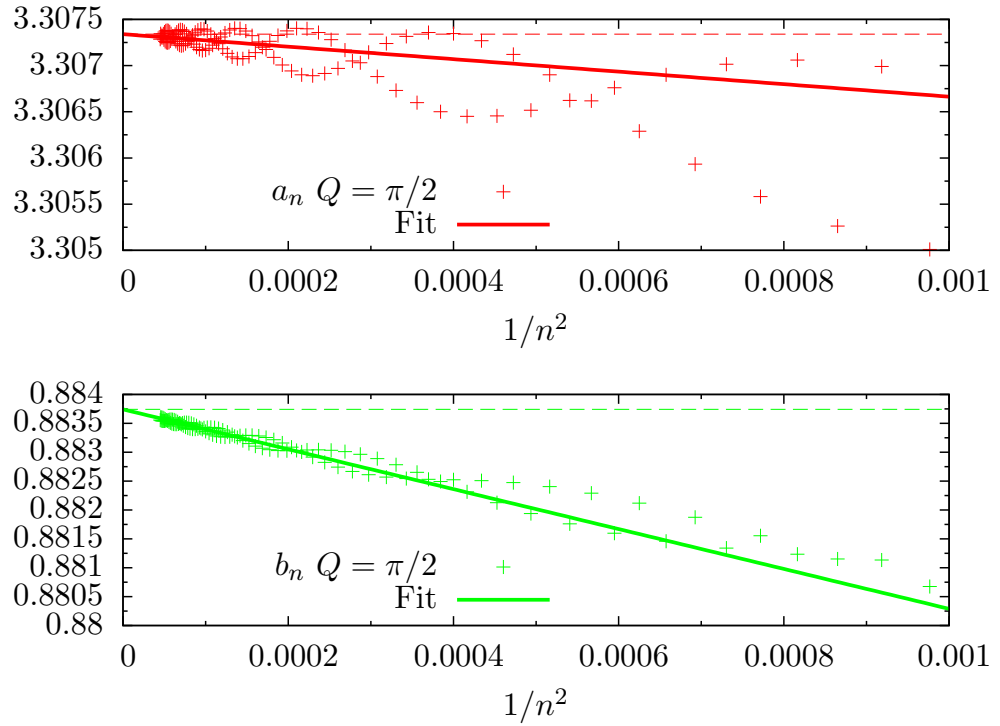


Figure 7.26: Continued fraction coefficients for the case $J = 1.5\Gamma$ and total momentum $Q = \pi/2$. The upper panel shows the coefficients a_n and the lower panel shows the coefficients b_n . The limit values are indicated by horizontal lines. Note that the x-axis scale is $1/n^2$.

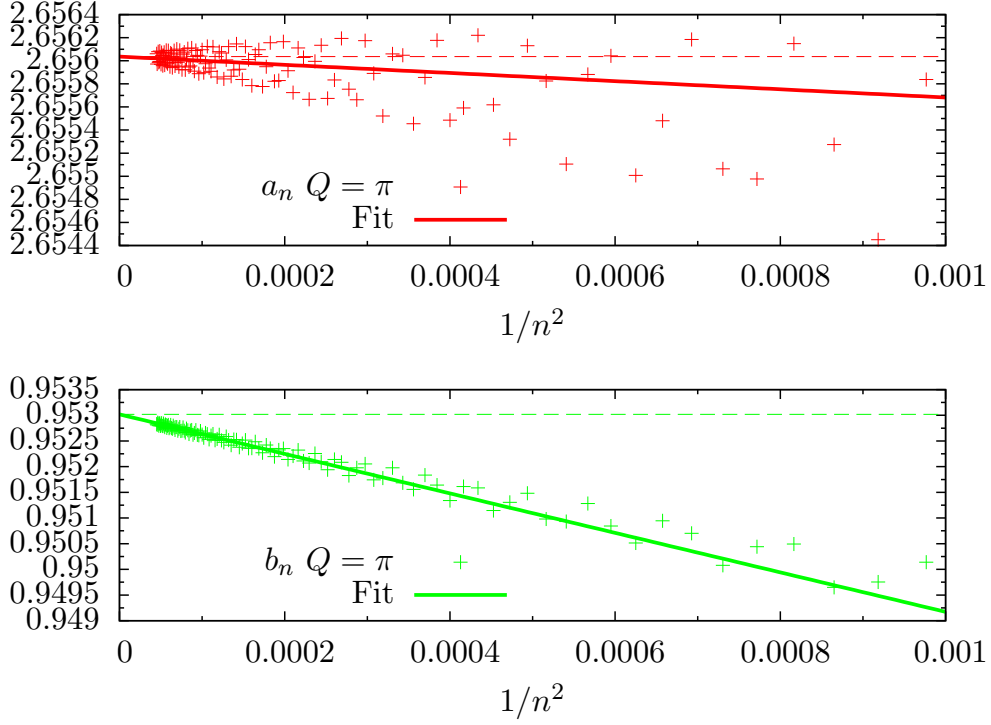


Figure 7.27: Continued fraction coefficients for the case $J = 1.5\Gamma$ and total momentum $Q = \pi$. The upper panel shows the coefficients a_n and the lower panel shows the coefficients b_n . The limit values are indicated by horizontal lines. Note that the x-axis scale is $1/n^2$.

Band Edge Singularities for $S_3^{xx}(\omega, Q)$		
Q	α	β
0	(2.47 ± 0.05)	(0.98 ± 0.02)
$\pi/2$	(2.97 ± 0.04)	(2.70 ± 0.04)
π	(2.95 ± 0.05)	(2.82 ± 0.04)

Table 7.1: Exponents for the Band Edge Singularities for $S_3^{xx}(\omega, Q)$

The values for the band edge singularities obtained by the linear fit, using the Levenberg-Marquardt algorithm [50, 51], are shown in Tab. 7.1. For $Q = \pi$ and $Q = \pi/2$ both exponents seem to be 3 while in the case $Q = 0$ the exponents differ and we assume that $\alpha = 2.5$ and $\beta = 1$ holds.

In Ref. [64] a general expression for the multi-particle band edge singularities is derived for a hardcore boson toy model. It reads,

$$S_n \propto \omega^{\frac{n^2-3}{2}} \quad \text{for } n > 1, \quad (7.5.51)$$

independent of total momentum Q . For the three-particle case this yields $S_n \propto \omega^3$, which is in agreement with our results for $Q = \pi$ and $Q = \pi/2$, but differs for $Q = 0$. A possible explanation for this could be the more complicated structure of our effective Hamiltonian.

7.6 Conclusions of the present chapter

In this chapter we investigated the dynamical structure factor for the longitudinal and transverse case of the TFIM. With the help of the CUT it is possible to divide the DSF into contributions from different quasi-particle spaces that are not mixed by the effective Hamiltonian. We then used a continued fraction representation of the resolvent and the Lanczos tridiagonalization to find results for the DSF.

For S^{zz} , exact results are known and could also be reproduced by the CUT. We investigated how the numerical limitations, such as the restriction of the Hilbert space, affects the results. These findings are useful for cases, in which no exact expression is known.

For the one-particle contributions of S^{xx} Hamer et al. [19] proposed an exact expression in 2006. Our results are in good agreement with this expression and verify their findings at least for small parameters J .

Subsequently new results are shown for the three-particle case of S^{xx} . It strongly differs from the semi elliptic two quasi-particle continuum in the S^{zz} case. For higher parameters, most of the spectral weight is concentrated at the lower band edge. With the help of the continued fraction coefficients we also extracted information about the band edge singularities.

These results show that higher particle spaces are also accessible with the help of effective Hamiltonians and observables derived by the CUT method. For parameters $J > 2\Gamma$, the present perturbative approach is of course not useful anymore, however we are still able to describe relatively long correlation lengths in the polarized phase.

8 Conclusion

In this thesis we investigated the transverse field Ising model (TFIM) by means of continuous unitary transformations (CUT).

8.1 Results

First the general framework of continuous unitary transformations was introduced, with a special focus on the enhanced perturbative realization of the method (epCUT and deepCUT). The string algebra was introduced as our operator basis on which we perform the CUT. The closing property of the algebra under the commutator was shown for a one dimensional chain. Next the TFIM was written in terms of string operators and the CUT method was applied in this operator basis. We have shown that the derivation of effective models up to very high orders in the parameter J is possible. Furthermore, it was possible to derive the flow equation up to infinite order. This is a remarkable step, because the TFIM is a non-trivial model in the thermodynamic limit.

Next we investigated the static properties of the TFIM and compared them to the exact results calculated by Pfeuty. The ground state energy per site, the transverse magnetization as well as the energy dispersion agreed very well up to the critical point $J = 2\Gamma$. Above the critical point only the ground state energy and the transverse magnetization were close to the exact calculation. For this case the dispersion was only in partial agreement. Still, this is a remarkable result, because our quasi-particle picture breaks down at the quantum critical point (QCP) and the elementary excitations for $J > 2\Gamma$ are non-local domain walls, hard to describe by means of local spin flips.

Next we investigated the dynamical structure factor (DSF) for the TFIM at zero temperature. We started by introducing the general framework to calculate Green functions within our effective model. We used the Lanczos algorithm and a continued fraction representation to calculate the resolvent representing the DSF.

In the next section the transverse DSF was calculated and compared to the exact results. For these spectral properties, high orders are available within the string operator basis. All results agree well with the exact results. Many of the small deviations were located at the edges of the continuum, which can be explained by the square root singularity located at these points.

Next, the longitudinal DSF was considered. Here the order of calculation was limited to a maximum of 38. However we were still able to confirm the results by Hamer et al.

for small enough parameters J .

A novel result is the calculation of three-particle contributions to the DSF. This is a very complicated problem, because the interaction of multiple particles on the chain must be considered. Still all results show good convergence for sufficiently high orders and are therefore considered to be quantitatively correct. The three-particle continuum shows an accumulation of spectral weight at the lower edge. We also obtained exponents for the band edge singularities by investigating the convergence of the continued fraction coefficients.

8.2 Outlook

Further investigations could include the S^{yy} DSF or finite temperature effects, leading to a broadening of single particle lines as well as low frequency responses due to intraband scattering. However this remains a difficult task, because the full statistical operator must be considered in order to calculate the needed Green functions.

Furthermore, the method of CUT is not restricted to one dimensional systems, therefore higher dimensions can be considered to further investigate multi-particle excitations in these systems. For example the 2d transverse field Ising model should be in the same universality class as the 3d classical Ising model, which is not exactly solvable so far. Therefore, calculation of critical exponents could be an interesting research topic.

List of Figures

2.1	Phase diagram for a generic high-temperature superconductor of the cuprate family. T denotes the temperature and δ the degree of doping.	7
3.1	In the limit $J = 0$ the fully polarized state becomes the ground state of the TFIM.	11
3.2	Elementary excitation of the TFIM in the strong field limit.	12
3.3	The two ground states of the TFIM in the strong interaction limit. . . .	12
3.4	Domain walls are the elementary excitations of the TFIM in the strong interaction limit.	12
3.5	Ground state energy per site of the TFIM as function of J . The gray shaded region shows the ferromagnetically ordered phase while the black dashed line indicates the value of the groundstate energy at the phase transition, see section 3.4.	14
3.6	Energy dispersion of the elementary excitations of the TFIM for various values of J as function of wave vector q . Note that the dispersion is symmetric in the region $q < 0$, which is not shown here.	15
3.7	Transverse magnetization M_z as a function of J in the TFIM. The gray shaded region shows the ferromagnetically ordered phase while the black dashed line indicates the value of the transverse magnetization at the phase transition, see section 3.4.	15
3.8	Longitudinal magnetization M_x as a function of J . The gray shaded region shows the ferromagnetically ordered phase.	17
3.9	Phase diagram of the TFIM. The red curve indicates the order parameter and is only non-zero for $T = 0$, i.e. in the M_x - J -plane. The green curves indicate the quantum critical region (qc), here the physics is mainly dominated by quantum and thermal fluctuations. The blue line shows the ferromagnetic ordered phase (fm order) which does not extend to finite temperatures $T > 0$. The elementary excitations of the ferromagnetic ordered phase are domain walls. For small parameters $J < 2\Gamma$ the system is in the polarized state (polarized) with single spin flips as elementary excitations.	18

4.1	Illustration of Wegner's generator. The boxes represent the matrix elements. The red boxes indicate the initial non diagonal parts of the Hamiltonian. The grey boxes indicate the Hamiltonian during the flow. The black boxes indicate the effective Hamiltonian after the flow. Note that degenerate subspaces are not diagonalized, represented by bigger black boxes.	23
4.2	Illustration of the pc generator. The boxes represent the matrix elements. The red boxes indicate the initial non diagonal parts of the Hamiltonian. The grey boxes indicate the Hamiltonian during the flow. The black boxes indicate the effective Hamiltonian after the flow. Note that the band diagonal structure is preserved during the flow.	25
4.3	Illustration of the algorithm used to determine all contributions for a given maximum order, here 4, from Ref. [41]. The boxes represent the calculation of the commutator between the different orders of the generator $\eta^{(m)}$ and the Hamiltonian $H^{(n)}$ to obtain the contributions to the DES. The calculation for every order o is based on the previous orders and is achieved by calculating every commutator with $n + m = o$	29
4.4	Illustration of the algorithm used to determine all contributions for the observable transformation for a given maximum order, here 4, from Ref. [41]. The boxes represent the calculation of the commutator between the different orders of the generator $\eta^{(m)}$ and the observable $O^{(n)}$ to obtain the contributions to the DES. The calculation for every order o is based on the previous orders and is achieved by calculating every commutator with $n + m = o$	31
5.1	Graphical representation of a single string operator.	36
5.2	Graphical representation of the commutator of two string operators. The position of the blocks represent the different sites upon which a local string operator acts.	36
5.3	Vanishing commutators of string operators on a chain.	36
5.4	Simplifying the first commutator by factoring out (red) and multiplying the inner string operators to identity (blue).	37
5.5	Simplifying the second commutator by factoring out (red) and multiplying the inner string operators to identity (blue).	38
5.6	Contributing commutators of string operators on a chain. The single box in the third commutator represents a single σ^z matrix.	39
5.7	Simplifying the first contributing commutator by factoring out (red) and multiplying the inner string operators to identity (blue).	39
5.8	Simplifying the last contributing commutator by multiplying the inner string operators to identity (blue).	40
6.1	ROD for different orders and a fixed value of $J = 1.0\Gamma$	50

6.2	ROD for different values of J and a fixed order.	50
6.3	ROD at the critical point $J = 2\Gamma$ for different orders.	51
6.4	Ground state energy per site as function of J . Comparison of the exact result with various CUT orders.	53
6.5	Absolute difference between the exact ground state energy per site and the CUT calculation as function of J . The QCP is located at $\log_{10} \left(\frac{J}{2\Gamma} \right) = 0$	54
6.6	Ground state energy per site as function of J above the QCP. Comparison of the exact result with various CUT orders.	54
6.7	Energy dispersion for $J = 0.2\Gamma$. Comparison of the exact result with the CUT calculation.	56
6.8	Energy dispersion for $J = 1.0\Gamma$. Comparison of the exact result with the CUT calculation.	56
6.9	Energy dispersion for $J = 1.9\Gamma$. Comparison of the exact result with the CUT calculation. The inset shows the difference between the exact result and the CUT calculation.	57
6.10	Energy dispersion at the QCP $J = 2\Gamma$. Comparison of the exact result with the CUT calculation. The inset shows the difference between the exact result and the CUT calculation.	57
6.11	Energy dispersion at the QCP $J = 2.5\Gamma$. Comparison of the exact result with the CUT calculation. The second CUT curve was filtered by a low pass so that only the first 16 Fourier-coefficients contribute.	58
6.12	Fourier coefficients t_n^{+-} for $J = 2.5\Gamma$ and order 256. At $n \approx 25$ it becomes conspicuous that the Fourier coefficients not yet converged.	59
6.13	Energy gap for different parameters J . Comparison of the exact result with the CUT calculation. All orders > 0 yield the same results within numerical errors.	59
6.14	Transverse Magnetization as a function of J . Comparison of the exact result with the CUT calculation. The inset shows a close view on the QCP.	61
6.15	Absolute difference between the exact transverse magnetization and the CUT calculation as function of J . The QCP is located at $\log_{10} \left(\frac{J}{2\Gamma} \right) = 0$	62
7.1	Graphical illustration of the local observable transformation by the CUT. The initial observable is located at site r . Due to the CUT new terms appear in the effective observable, which also act on neighboring sites. In this model the maximum range of the effective observable is given by the order of the calculation, but most of the weight will be located near the site r if we are not too close to the QCP.	67
7.2	Graphical illustration of the finite broadening effect. The exact spectral density is shown as the black curve. This is also the curve obtained by the use of the square root terminator. The parameters of the exact density are $a = 0$ and $b = 1$. The red curve is the finite continued fraction of depth four with a finite broadening of $\delta = 0.1$	76

7.3	Graphical illustration of the band edge singularities in the DSF.	77
7.4	The DSF S^{zz} for the parameter $J = \Gamma$. The maximum range for the Lanczos algorithm is $d_{\max} = 1000$ sites, the continued fraction was evaluated to a depth of 50 and then terminated by the square root terminator. The color indicates the spectral density, see legend to the right. The upper and lower edge of the two-particle continuum are indicated by white lines.	79
7.5	The DSF S^{zz} for the parameter $J = 1.5\Gamma$. The maximum range for the Lanczos algorithm is $d_{\max} = 1000$ sites, the continued fraction was evaluated to a depth of 50 and then terminated by the square root terminator. The color indicates the spectral density, see legend to the right. The upper and lower edge of the two-particle continuum are indicated by white lines.	80
7.6	The DSF S^{zz} for the parameter $J = 1.9\Gamma$. The maximum range for the Lanczos algorithm is $d_{\max} = 1000$ sites, the continued fraction was evaluated to a depth of 50 and then terminated by the square root terminator. The color indicates the spectral density, see legend to the right. The upper and lower edge of the two-particle continuum are indicated by white lines.	80
7.7	DSF S^{zz} for the parameter $J = \Gamma$ for three total momenta Q . The maximum range for the Lanczos algorithm is $d_{\max} = 4000$ sites, the continued fraction was evaluated to a depth of 100 and then terminated by the square root terminator.	81
7.8	DSF S^{zz} for the parameter $J = 1.5\Gamma$ for three total momenta Q . The maximum range for the Lanczos algorithm is $d_{\max} = 4000$ sites, the continued fraction was evaluated to a depth of 100 and then terminated by the square root terminator.	82
7.9	DSF S^{zz} for the parameter $J = 1.9\Gamma$ for three total momenta Q . The maximum range for the Lanczos algorithm is $d_{\max} = 4000$ sites, the continued fraction was evaluated to a depth of 100 and then terminated by the square root terminator.	82
7.10	Difference of the exact DSF S^{zz} and the CUT calculation for the parameter $J = \Gamma$. The maximum range for the Lanczos algorithm is $d_{\max} = 4000$ sites, the continued fraction was evaluated to a depth of 100 and then terminated by the square root terminator.	83
7.11	Difference of the exact DSF S^{zz} and the CUT calculation for the parameter $J = 1.5\Gamma$. The maximum range for the Lanczos algorithm is $d_{\max} = 4000$ sites, the continued fraction was evaluated to a depth of 100 and then terminated by the square root terminator.	84

- 7.12 Difference of the exact DSF S^{zz} and the CUT calculation for the parameter $J = 1.9\Gamma$. The maximum range for the Lanczos algorithm is $d_{\max} = 4000$ sites, the continued fraction was evaluated to a depth of 100 and then terminated by the square root terminator. 84
- 7.13 Continued fraction coefficients for the case $J = 1.5\Gamma$ and total momenta $Q = 0$ and $Q = \pi/2$. The upper plot shows the first ten coefficients converging rapidly to their limit values indicated by horizontal lines. The lower plot shows the absolute difference between the coefficients and their final values. 85
- 7.14 Continued fraction coefficients for the case $J = 1.5\Gamma$ and total momentum $Q = \pi/2$. The upper plot shows the coefficients a_n and the lower one the coefficients b_n . The limit values are indicated by horizontal lines. Note that the x-axis scale is $1/n^2$ 86
- 7.15 Continued fraction coefficients for the case $J = 1.5\Gamma$ and total momentum $Q = \pi/2$. The maximum range for the Lanczos algorithm is lowered to $d_{\max} = 200$ sites. At $n \approx 55$ the restriction of the Hilbert space spoils the convergences of the coefficients. 86
- 7.16 Overview of the one-particle equal time structure factor $S_1^{xx}(Q)$ for different parameters J . For $J \rightarrow 2\Gamma$ the value at $Q = \pi$ diverges although the integral remains finite. 88
- 7.17 One-particle equal time structure factor $S_1^{xx}(Q)$ for the parameter $J = \Gamma$. Comparison of the exact expression with the CUT results. The inset shows the absolute difference between the exact curve and the CUT. . . . 89
- 7.18 One-particle equal time structure factor $S_1^{xx}(Q)$ for the parameter $J = 1.5\Gamma$. Comparison of the exact expression with the CUT results. The inset shows the absolute difference between the exact curve and the CUT. 89
- 7.19 One-particle equal time structure factor $S_1^{xx}(Q)$ for the parameter $J = 1.9\Gamma$. Comparison of the exact expression with the CUT results. The inset shows the absolute difference between the exact curve and the CUT. 90
- 7.20 One-particle spectral weight as function of the parameter J . Comparison of the exact expression with the CUT results. The inset shows the absolute difference between the exact curve and the CUT. 91
- 7.21 The DSF S_3^{xx} for the parameter $J = \Gamma$. The maximum range for the Lanczos algorithm is $d_{\max} = 100$ sites, the continued fraction was evaluated to a depth of 50 and then terminated by the square root terminator. The color indicates the spectral density, see legend to the right. The dispersion is indicated by the white solid line. The upper and lower edge of the two-particle continuum are indicated by white dashed lines. 92

- 7.22 The DSF S_3^{xx} for the parameter $J = 1.5\Gamma$. The maximum range for the Lanczos algorithm is $d_{\max} = 100$ sites, the continued fraction was evaluated to a depth of 50 and then terminated by the square root terminator. The color indicates the spectral density, see legend to the right. The dispersion is indicated by the white solid line. The upper and lower edge of the two-particle continuum are indicated by white dashed lines. 93
- 7.23 The DSF S_3^{xx} for the parameter $J = 1.9\Gamma$. The maximum range for the Lanczos algorithm is $d_{\max} = 100$ sites, the continued fraction was evaluated to a depth of 50 and then terminated by the square root terminator. The color indicates the spectral density, see legend to the right. The dispersion is indicated by the white solid line. The upper and lower edge of the two-particle continuum are indicated by white dashed lines. 93
- 7.24 DSF S_3^{xx} for the parameter $J = 1.75\Gamma$ for three chosen total momenta Q . The maximum range for the Lanczos algorithm is $d_{\max} = 200$ sites, the continued fraction was evaluated to a depth of 100 and then terminated by the square root terminator. 94
- 7.25 Continued fraction coefficients for the case $J = 1.5\Gamma$ and total momentum $Q = 0$. The upper panel shows the coefficients a_n and the lower panel shows the coefficients b_n . The limit values are indicated by horizontal lines. The red/green lines indicated linear fits for small $1/n^2$. Note that the x-axis scale is $1/n^2$ 95
- 7.26 Continued fraction coefficients for the case $J = 1.5\Gamma$ and total momentum $Q = \pi/2$. The upper panel shows the coefficients a_n and the lower panel shows the coefficients b_n . The limit values are indicated by horizontal lines. Note that the x-axis scale is $1/n^2$ 95
- 7.27 Continued fraction coefficients for the case $J = 1.5\Gamma$ and total momentum $Q = \pi$. The upper panel shows the coefficients a_n and the lower panel shows the coefficients b_n . The limit values are indicated by horizontal lines. Note that the x-axis scale is $1/n^2$ 96

List of Tables

6.1	Exponents of the power laws for the ground state energy obtained by fitting linear functions.	53
6.2	Exponents of the power laws for the transverse magnetization obtained by fitting linear functions.	61
7.1	Exponents for the Band Edge Singularities for $S_3^{xx}(\omega, Q)$	96

Bibliography

- [1] J. G. Bednorz and K. A. Müller. Possible high T_c superconductivity in the Ba-La-Cu-O system. *Zeitschrift für Physik B*, 64:189–193, 1986.
- [2] A. J. Leggett. What do we know about high T_c ? *Nature Physics*, 2:134–136, March 2006.
- [3] H. Luetkens, H. H. Klauss, M. Kraken, F. J. Litterst, T. Dellmann, R. Klingeler, C. Hess, R. Khasanov, A. Amato, C. Baines, M. Kosmala, O. J. Schumann, M. Braden, J. Hamann-Borrero, N. Leps, A. Kondrat, G. Behr, J. Werner, and B. Büchner. The electronic phase diagram of the $\text{LaO}_{1-x}\text{F}_x\text{FeAs}$ superconductor. *Nature Materials*, 8:305–309, April 2009.
- [4] C. W. Chu, F. Chen L. Gao, Z. J. Huang, R. L. Meng, and Y. Y. Xue. Superconductivity above 150 K in $\text{HgBa}_2\text{Ca}_2\text{Cu}_3\text{O}(8+\delta)$ at high pressures. *Nature*, 365:323–325, September 1993.
- [5] A. H. Silver R. C. Jaklevic, J. Lambe and J. E. Mercereau. Quantum Interference Effects in Josephson Tunneling. *Physical Review Letters*, 12:159–160, February 1964.
- [6] J. Bardeen, L. N. Cooper and J. R. Schrieffer. Theory of Superconductivity. *Physical Review*, 108:1175–1204, December 1957.
- [7] S. Sanna, G. Allodi, G. Concas, A. D. Hillier, and R. D. Renzi. Nanoscopic Coexistence of Magnetism and Superconductivity in $\text{YBa}_2\text{Cu}_3\text{O}_{6+x}$ Detected by Muon Spin Rotation. *Physical Review Letters*, 93(20):207001, November 2004.
- [8] J. Orenstein and A. J. Millis. Advances in the Physics of High-Temperature Superconductivity. *Science*, 288(5465):468–474, 2000.
- [9] P. W. Anderson. The Resonating Valence Bond State in La_2CuO_4 and Superconductivity. *Science*, 235(4793):1196–1198, 1987.
- [10] W. Heisenberg. Zur Theorie des Ferromagnetismus. *Zeitschrift für Physik A*,

49:619–636, 1928.

- [11] P. G. de Gennes. Collective motions of hydrogen bonds. *Solid State Communications*, 6:132–137, 1963.
- [12] R. B. Stinchcombe. Ising model in a transverse field. *Journal of Physics C*, 6(15):2459, 1973.
- [13] H. M. Rønnow, R. Parthasarathy, J. Jensen, G. Aeppli, T. F. Rosenbaum, and D. F. McMorrow. Quantum Phase Transition of a Magnet in a Spin Bath. *Science*, 308(5720):389–392, 2005.
- [14] P. B. Chakraborty, P. Henelius, H. Kjønsberg, A. W. Sandvik, and S. M. Girvin. Theory of the magnetic phase diagram of LiHoF_4 . *Physical Review B*, 70(14):144411, October 2004.
- [15] C. N. Yang. Concept of Off-Diagonal Long-Range Order and the Quantum Phases of Liquid He and of Superconductors. *Review of Modern Physics*, 34:694–704, October 1962.
- [16] S. Sachdev. *Quantum Phase Transitions*. Cambridge University Press, 2001.
- [17] K. G. Wilson and J. Kogut. The renormalization group and the ϵ expansion. *Physics Reports*, 12(2):75 – 199, 1974.
- [18] A. J. A. James, W. D. Goetze and F. H. L. Essler. Finite-temperature dynamical structure factor of the Heisenberg-Ising chain. *Physical Review B*, 79:214408, June 2009.
- [19] C. J. Hamer, J. Oitmaa, Z. Weihong and R.H. McKenzie. Critical behavior of one-particle spectral weights in the transverse Ising model. *Physical Review B*, 74:060402, August 2006.
- [20] H. Fröhlich. Theory of the Superconducting State. I. The Ground State at the Absolute Zero of Temperature. *Physical Review*, 79:845–856, September 1950.
- [21] F. Wegner. Flow-equations for Hamiltonians. *Annalen der Physik*, 506(2):77–91, 1994.
- [22] S. D. Glazek and K. G. Wilson. Renormalization of Hamiltonians. *Physical Review D*, 48:5863–5872, December 1993.
- [23] S. D. Glazek and K. G. Wilson. Perturbative renormalization group for Hamiltonians. *Physical Review D*, 49:4214–4218, April 1994.

- [24] K. P. Schmidt, C. Knetter and G.S. Uhrig. Spectral properties of the dimerized and frustrated $S = 1/2$ chain. *Physical Review B*, 69:104417, March 2004.
- [25] C. Knetter, K. P. Schmidt and G.S. Uhrig. High order perturbation theory for spectral densities of multi-particle excitations: $S = 1/2$ two-leg Heisenberg ladder. *European Physical Journal B*, 36(4):525–544, 2003.
- [26] T. Fischer, S. Duffe and G. S. Uhrig. Microscopic model for Bose-Einstein condensation and quasiparticle decay. *Europhysics Letters*, 96(4):47001, 2011.
- [27] S. Hamerla, S. Duffe and G.S. Uhrig. Derivation of the t - J model for finite doping. *Physical Review B*, 82:235117, December 2010.
- [28] J. Vidal, K. P. Schmidt and S. Dusuel. Perturbative approach to an exactly solved problem: Kitaev honeycomb model. *Physical Review B*, 78:245121, December 2008.
- [29] J. Vidal, S. Dusuel and K. P. Schmidt. Low-energy effective theory of the toric code model in a parallel magnetic field. *Physical Review B*, 79:033109, January 2009.
- [30] H. Y. Yang and K. P. Schmidt. Effective models for gapped phases of strongly correlated quantum lattice models. *Europhysics Letters*, 94(1):17004, 2011.
- [31] P. Pfeuty. The One-Dimensional Ising Model with a Transverse Field. *Annals of Physics*, 57:79–90, 1970.
- [32] E. Lieb, T. Schultz and D. Mattis. Two soluble models of an antiferromagnetic chain. *Annals of Physics*, 16:407–466, 1961.
- [33] T. Niemeijer. Some exact calculations on a chain of spins $1/2$.
- [34] E. Ising. Beitrag zur Theorie des Ferromagnetismus. *Zeitschrift für Physik*, 31:253–258, February 1925.
- [35] P. Jordan and E. Wigner. Über das Paulische Äquivalenzverbot. *Zeitschrift für Physik A*, 47:631–651, 1928.
- [36] N. Bogoliubov. *Journal of Physics (USSR)*, 11:23, 1947.
- [37] O. Derzhko and T. Krokhamalskii. Dynamic structure factor of the spin- $\frac{1}{2}$ transverse Ising chain. *Physical Review B*, 56:11659–11665, November 1997.
- [38] O. Derzhko, T. Verkholyak, T. Krokhamalskii and H. Büttner. Dynamic probes of quantum spin chains with the Dzyaloshinskii-Moriya interaction. *Physical Review B*, 73(21):214407, June 2006.

- [39] S. W. Lovesey. *Theory of Neutron Scattering from Condensed Matter*. Oxford University Press, 1987.
- [40] H. Krull. *Verbesserte perturbative kontinuierliche unitäre Transformation mit direkter Auswertung*. Diplomarbeit, TU Dortmund, 2011.
- [41] H. Krull, N. A. Drescher and G. S. Uhrig. Enhanced perturbative continuous unitary transformations. *Physical Review B*, 86:125113, September 2012.
- [42] A. Mielke. Flow equations for band-matrices. *European Physical Journal B*, 5:605–611, 1998.
- [43] C. Knetter and G.S. Uhrig. Perturbation theory by flow equations: dimerized and frustrated $S = 1/2$ chain. *European Physical Journal B*, 13:209–225, 2000.
- [44] S. Dusuel and G.S. Uhrig. The quartic oscillator: a non-perturbative study by continuous unitary transformations. *Journal of Physics A*, 37(39):9275, 2004.
- [45] S. Duffe and G. S. Uhrig. Hole dispersions for antiferromagnetic spin-1/2 two-leg ladders by self-similar continuous unitary transformations. *The European Physical Journal B*, 84:475–490, 2011.
- [46] A. Reischl. *Derivation of Effective Models using Self-Similar Continuous Unitary Transformations in Real Space*. PhD thesis, 2006.
- [47] S. Duffe. *Effective Hamiltonians for Undoped and Hole-Doped Antiferromagnetic Spin-1/2 Ladders by Self-Similar Continuous Unitary Transformations in Real Space*. PhD thesis, TU Dortmund, 2010.
- [48] G. Jost B. Chapman and R. van der Pas. *Using OpenMP: Portable Shared Memory Parallel Programming (Scientific and Engineering Computation)*. The MIT Press, 2007.
- [49] H. A. Kramers and G. H. Wannier. Statistics of the two-dimensional ferromagnet. part i. *Physical Review*, 60:252–262, August 1941.
- [50] K. Levenberg. A Method for the Solution of Certain Non-Linear Problems in Least Squares.
- [51] D. Marquardt. An Algorithm for Least-Squares Estimation of Nonlinear Parameters.
- [52] T. Fischer. *Description of quasiparticle decay by continuous unitary transformations*. PhD thesis, 2012.

- [53] A. J. A. James, F. H. L. Essler and R. M. Konik. Finite-temperature dynamical structure factor of alternating Heisenberg chains. *Physical Review B*, 78(9):094411, September 2008.
- [54] A. J. A. James, W. D. Goetze and F. H. L. Essler. Finite-temperature dynamical structure factor of the Heisenberg-Ising chain. *Physical Review B*, 79(21):214408, June 2009.
- [55] A. E. Feiguin and S. R. White. Time-step targeting methods for real-time dynamics using the density matrix renormalization group. *Physical Review B*, 72:020404, July 2005.
- [56] D. Chandler. *Introduction to Modern Statistical Mechanics*. Oxford University Press, 1987.
- [57] C. Knetter and G. S. Uhrig. Dynamic structure factor of the two-dimensional shastry-sutherland model. *Physical Review Letters*, 92:027204, January 2004.
- [58] K. P. Schmidt. *Spectral Properties of Quasi One-dimensional Quantum Antiferromagnets Perturbative Continuous Unitary Transformations*. PhD thesis, 2004.
- [59] D. G. Pettifor and D. L. Weaire. *The Recursion Method and its Applications*, volume 58. Springer Verlag, Berlin, 1985.
- [60] V. S. Viswanath and G. Müller. *The Recursion Method*. Springer Verlag, Berlin, 1994.
- [61] W. Vetterling W. Press, S. Teukolsky and B. Flannery. *Numerical Recipes in C*. Cambridge University Press, Cambridge, UK, 2nd edition, 1992.
- [62] G. S. Uhrig and H. J. Schulz. Magnetic excitation spectrum of dimerized antiferromagnetic chains. *Physical Review B*, 54:R9624–R9627, October 1996.
- [63] G. S. Uhrig and H. J. Schulz. Erratum: Magnetic excitation spectrum of dimerized antiferromagnetic chains. *Physical Review B*, 58:2900–2900, August 1998.
- [64] S. Kirschner. *Multi-particle spectral densities*. Diplomarbeit, Universität zu Köln, 2004.

Danksagung

An dieser Stelle möchte ich mich bei Prof. Dr. Götz S. Uhrig für die Vergabe des interessanten Themas und die hervorragende Betreuung während der Masterarbeit bedanken. Dr. Kai P. Schmidt danke ich für die Übernahme des Zweitgutachtens der Arbeit.

Besonders bedanken möchte ich mich auch bei Nils Drescher, der mir bei einem großen Teil der Programmierarbeit geholfen hat und auch die Arbeit korrekturgelesen hat.

Meinen Bürokollegen danke ich für die interessanten Diskussionen, die auch über die Physik hinaus gingen.

Bei Laura Möller und Frederik Keim bedanke ich mich für das Korrekturlesen und die Hilfestellung.

Ich möchte mich auch bei der gesamten Arbeitsgruppe bedanken, die immer Hilfsbereit ist und in der es immer ein angenehmes Arbeitsklima gibt.

Zuletzt möchte ich meiner Familie danken, die mir jederzeit helfend zur Seite steht und mein Studium erst ermöglicht hat.

Eidesstattliche Versicherung

Ich versichere hiermit an Eides statt, dass ich die vorliegende Masterarbeit mit dem Titel "Analysis of the transverse field Ising model by continuous unitary transformations" selbständig und ohne unzulässige fremde Hilfe erbracht habe. Ich habe keine anderen als die angegebenen Quellen und Hilfsmittel benutzt sowie wörtliche und sinngemäße Zitate kenntlich gemacht. Die Arbeit hat in gleicher oder ähnlicher Form noch keiner Prüfungsbehörde vorgelegen.

Ort, Datum

Unterschrift

Belehrung

Wer vorsätzlich gegen eine die Täuschung über Prüfungsleistungen betreffende Regelung einer Hochschulprüfungsordnung verstößt handelt ordnungswidrig. Die Ordnungswidrigkeit kann mit einer Geldbuße von bis zu 50.000,00€ geahndet werden. Zuständige Verwaltungsbehörde für die Verfolgung und Ahndung von Ordnungswidrigkeiten ist der Kanzler/die Kanzlerin der Technischen Universität Dortmund. Im Falle eines mehrfachen oder sonstigen schwerwiegenden Täuschungsversuches kann der Prüfling zudem exmatrikuliert werden (§ 63 Abs. 5 Hochschulgesetz - HG -).

Die Abgabe einer falschen Versicherung an Eides statt wird mit Freiheitsstrafe bis zu 3 Jahren oder mit Geldstrafe bestraft.

Die Technische Universität Dortmund wird ggf. elektronische Vergleichswerkzeuge (wie z.B. die Software "turnitin") zur Überprüfung von Ordnungswidrigkeiten in Prüfungsverfahren nutzen.

Die oben stehende Belehrung habe ich zur Kenntnis genommen.

Ort, Datum

Unterschrift